UNIVERSITY OF CALIFORNIA
RIVERSIDE

Doping Effects in Organic Low-Dimensional Conducting Materials and their Opto-Electronic Applications

A Dissertation submitted in partial satisfaction
of the requirements for the degree of

Doctor of Philosophy

in

Chemistry

by

Dejan Stekovic

December 2018

Dissertation Committee:

- Dr. Mikhail E. Iktis, Co-Chairperson
- Dr. Eric L. Chronister, Co-Chairperson
- Dr. Richard J. Hooley
- Dr. Matthew P. Conley

The Dissertation of Dejan Stekovic is approved:

Committee Co- Chairperson

Committee Co-Chairperson

University of California, Riverside

ACKNOWLEDGMENTS

Throughout my life and my academic career, I have been fortunate enough to have many people support me. Without them I would not have been able to make it this far. First and foremost, I would like to thank my mother, father, and sister for their support throughout the years no matter the scenario. I could not have made it to this point without you.

During my time at UCR I have been influenced by several great scientists. I would like to thank Robert C. Haddon for first allowing me to join the group. You showed me how a scientist thinks and always had time to discuss our projects. The scientific community was lucky to have you. I thank Mikhail E. Itkis for taking up the advisor role after Dr. Haddon's passing. Thank you for all that you have taught me and your patience as I learned about fields new to me, I have learned a lot from you. I would also like to thank Dr. Eric L. Chronister for also acting as an advisor and allowing me to continue Dr. Haddon's research.

I thank the many group members I've had throughout the years. Dr. Pradip Bag for teaching me synthetic organic chemistry and how to grow crystals as well as providing useful advice. Dr. Sushanta K. Pal for also helping to teach me about neutral radical crystals. Dr. Elena Haddon for teaching me about carbon nanotubes and allowing me to have first-hand experience at Carbon Solutions. I thank my fellow graduate students Guanghui Li, Wangxiang Li, Mingguang Chen, Basim Arkook, and Matthew Moser for their contributions to my projects for helping me to understand the science behind it all.

Portions of the dissertation are adapted with permission from the following references:

Chapter 2: Stekovic, D.; Arkook, B.; Li, G.; Li, W.; Bekyarova, E.; Itkis, M.E., High Modulation Speed, Depth, and Coloration Efficiency of Carbon Nanotube Thin Film Electrochromic Device Achieved by Counter Electrode Impedance Matching *Adv. Mat. Inter.* **2018**, 5, 1800861.

Chapter 3: Bag, P.; Itkis, M.E.; Stekovic, D.; Pal, S.K.; Tham,F.S.; Haddon, R.C., Band Structure Engineering by Substitutional Doping in Solid-State Solutions of [5-Me-PLY(O, O)]$_2$B$_{(1-x)}$Be$_x$ Radical Crystals *J. Am. Chem. Soc.* **2015**, 137, 10000-10008.

Chapter 4: Stekovic, D.; Bag, P.; Shankhari, P.; Fokwa, B.P.T.; Itkis, M.E., Effect of Substitution on the Hysteretic Phase Transition in a Bistable Phenalenyl Based Neutral Radical Molecular Conductor *Under Review.*

Chapter 6: Stekovic, D; Itkis, M.E., Phenalenyl Based Neutral Radical as a Novel Electrochromic Material Modulating Visible to Short-Wave Infrared Light *Under Review.*

ABSTRACT OF THE DISSERTATION

Doping Effects in Organic Low-Dimensional Conducting Materials and their Opto-Electronic Applications

by

Dejan Stekovic

Doctor of Philosophy, Graduate Program in Chemistry
University of California, Riverside, December 2018
Dr. Mikhail E. Itkis, Dr. Eric L. Chronister, Co-Chairpersons

The field of materials science has produced a variety of valuable products and technologies defining modern day civilization. While still dominated by inorganic materials, the field of organic electronics opens new technological opportunities and the access to a new class of complementary materials. Being carbon based, organic electronic materials are abundant and environment friendly, often made with low temperature processing compatible with existing inorganic materials, and highly tunable for specific optical and electronic properties. These properties have helped enable the use of organic electronic materials throughout a wide range of products. Some of these include organic light emitting diodes (OLEDs) for electronic displays and lighting, organic field effect transistors (OFETs) for device control and computing, and organic

photovoltaics (OPVs) for energy generation among other uses. With their wide range of uses, the study of organic electronic materials is of high importance.

In this work, we examine both highly studied and relatively new low-dimensional materials. Since their discovery in 1991, single-walled carbon nanotubes (SWNTs) have seen much interest due to their unique electronic and optical properties. Here we design all-SWNT electrochromic devices capable of modulating incoming light with fast response times (few milliseconds). The mechanism behind the device is explored through the view of an electric double layer capacitor (EDLC) and reveals important clues for the design of fast electrochromic devices.

Also explored here is the substitutional doping of phenalenyl based radical molecular conductors. Through the use of substitutional doping most commonly used in silicon-based semiconductors, we demonstrate the enhancement of the electrical conductivity of some molecular conductors and modification of their magnetic properties. We also explored the possibility of using the substitutional doping to control a hysteretic phase transition and related bistable state in another phenalenyl based radical molecular conductor. Finally, the phenalenyl based radicals are incorporated into an electrochromic device which is able to modulate both visible and short-wave infrared light thus opening a novel pathway for development of a new class electrochromic materials for smart window applications.

Table of Contents

List of Figures

reductant (tetrakis(dimethylamino)ethylene (TDAE)) is added to grow solid solutions of $[Bu]_2B_{1-x}Be_x$.

Figure 4.4: Pictures of crystals of (a) $[Bu]_2B$, (b) lightly doped $[Bu]_2B_{1-x}Be_x$, (c) heavily doped $[Bu]_2B_{1-x}Be_x$ and (d) $[Bu]_2Be$. The scale bars are 1 mm.

Figure 4.5: Perpendicular views of $[Bu]_2B$ dimers in its (a, b) low spin and (c, d) high spin states showing interfacial distances and high degree of overlap between spin-bearing carbons shown in green. (e-h) Views of $[Bu]_2Be$ crystal interactions showing larger interfacial distances and little to no overlap of spin-bearing carbons shown in green.

Figure 4.6: Powder X-ray diffraction data of solid solutions of $[Bu]_2B_{1-x}Be_x$ showing the transition of the structure from that of the host ($[Bu]_2B$) to that of the dopant ($[Bu]_2Be$).

Figure 4.7: Temperature dependent fraction of Curie spin per molecule as a function of doping level x. (a) Lightly substituted $[Bu]_2B_{1-x}Be_x$: Compression of the height of the hysteresis loop with increasing doping; (b) Expanded view of the hysteresis loop above room temperature for lightly substituted $[Bu]_2B_{1-x}Be_x$ showing no phase transition; (d) Events of reverse hysteresis loop at x~6%.

Figure 4.8: (a) Height and (b) width of the hysteretic loop as a function of doping. (c) Curie spin per molecule of the high spin (HS) and low spin (LS) states as a function of doping. (d) Curie spin per molecule at 150 K as a function of doping.

Figure 4.9: Conductivity of doped neutral radical conductors. (a) Zoomed in view of the transition showing a lowering of conductivity as doping is increased and an eventual elimination of the hysteretic phase transition. (b) Arrhenius plot of temperature dependencies of electrical conductivity of various solid solutions of $[Bu]_2B_{1-x}Be_x$ in a wide temperature range.

Figure 4.10: Effects of substitution on $[Bu]_2B_{1-x}Be_x$ solid solutions. (left) With no doping (red) dimers of $[Bu]_2B$ form 2 electron bonds canceling out their spin, at light substitution levels (yellow) some of these are now 1 electron bonds but the $[Bu]B_2$ structure is retained. (Right) At heavy substitution levels $[Bu]_2B_{1-x}Be_x$ adopts the structure of $[Bu]_2Be$ and the spins are non-interacting.

Figure 4.11: Powder X-ray diffraction patterns for the compounds $[Bu]_2B$ (top) and $[Bu]_2Be$ (bottom). The green vertical lines represent calculated peak positions for the respective compounds obtained from their single crystal data. The most prominent peaks were located below $2\Theta = 30$ degree and hence the peak matching was performed only upto $2\Theta = 30$ degree. The full diffraction patterns (in the range $2\Theta = 3$-65 degrees are shown in insets).

List of Tables

List of Schemes

Chapter 1: Introduction to Organic Electronic Materials

1.1: Introduction

The field of materials science has produced many products that make up the technology that helps to define modern day civilization. While still dominated by inorganic materials, the field of organic electronic materials provides some advantages as well as complementary materials. Being carbon based, organic electronic materials are abundant, made with low temperature processing, compatible with existing inorganic materials and highly tunable for specific optical and electronic properties. These properties have helped enable the use of organic electronic materials throughout a wide range of products. Some of these include organic light emitting diodes (OLEDs)[1] for electronic displays and lighting, organic field effect transistors (OFETs)[2] for device control and computing, and organic photovoltaics (OPVs)[3] for energy generation among other uses. With their wide range of uses, the study of organic electronic materials is of high importance.

Organic electronic materials generally fall into one of three categories; polymers, small molecules, and other materials. Polymers are large macromolecules made up of repeating subunits and while they have many advantages, will not be covered here. Small molecule based organic electronic materials are highly tunable through synthetic organic chemistry and, as the name implies, made up of small organic molecules. The other category generally includes allotropes of carbon, such as graphene, fullerenes and carbon

nanotubes. Figure 1.1 shows some examples of all three types of organic electronic materials.

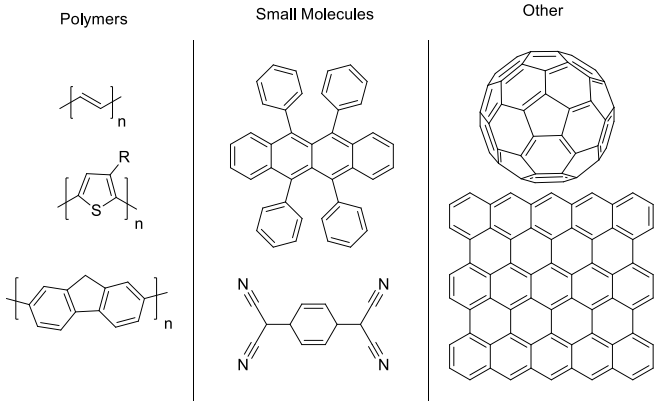

Figure 2.1: Examples of organic electronic materials. (left) Polymers; polyacetylene, poly(3-alkythiophene), and polyfluorene. (Middle) Small molecules; rubrene, and tetracyanoquinodimethane (TCNQ). Other; C_{60} (fullerene) and graphene (small section).

1.2 Introduction to Carbon Nanotubes

Carbon nanotubes (CNTs), as the name implies, are tubes of sp^2 hybridized carbon. They are often thought of as rolled up sheets of graphene (a flat plane of sp^2 hybridized carbon) and are 1-dimensional (1D) conductors. Since their discovery in 1991, CNTs have drawn much attention.[4] While CNTs can be either single-walled (SWNTs) or multi-walled (MWNTs), we will focus on SWNTs. SWNTs possess many exemplary properties such as high mechanical strength[5,6] and high thermal conductivity[7,8] along with unique optical[9,10] and electronic[11] properties. The optical and electronic properties of SWNTs are determined by their chiral indices (m,n) (Figure 1.2). The chiral indices determine both the diameter and the electronic properties of the SWNT. SWNTs are

classified as armchair if n = m, zigzag if either m or n is zero, or chiral (other n and m values). SWNTs are metallic (MT-SWNTs) if the absolute value of n – m is a multiple of 3 or zero. Otherwise, the SWNTs are classified as semiconducting SWNTs (SC-SWNTs). MT-SWNTs, as the name implies, are metallic in nature and thus have no bandgap. On the other hand, SC-SWNTs, have a bandgap that is inversely proportional to their diameter.[12-14]

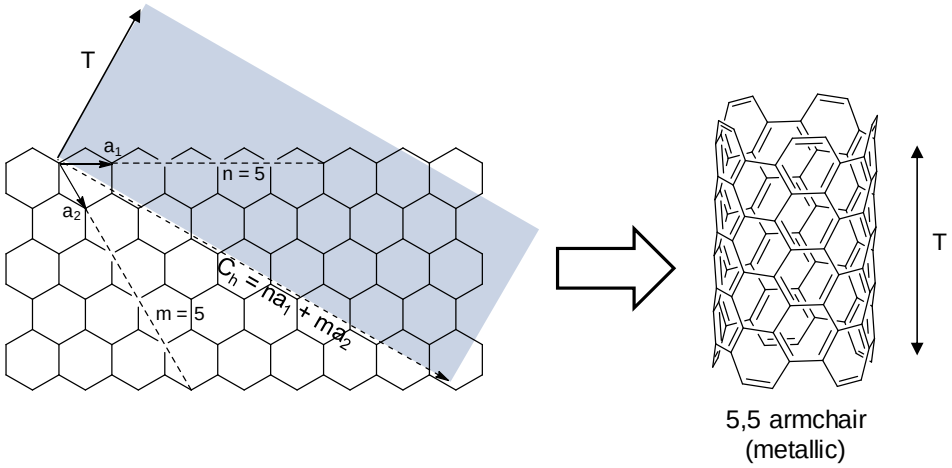

Figure 1.2: A graphene sheet (double bonds excluded for clarity) is wrapped into a SWNT. The chiral indices determine the diameter and electronic properties of the nanotube. Since n- m = 0 the resultant nanotube is metallic for this example of a (5,5) SWNT.

Another advantage of SWNTs is the ability to easily form thin films. These thin films have more macroscopic uses than individual nanotubes and have a better ease of use.[15] There are a number of ways to generate SWNT thin films such as drop casting, spray coating, and filtration. Figure 1.3 demonstrates the vacuum filtration method. A solution of suspended SWNTs is filtered through a membrane. After this the semi-transparent films can be transferred onto various substrates, in this case glass. As can be seen from the figure, SC-SWNTs have a

brownish color while MT-SWNTs have a blue-green color with the color difference originated from their different visible absorption spectra.

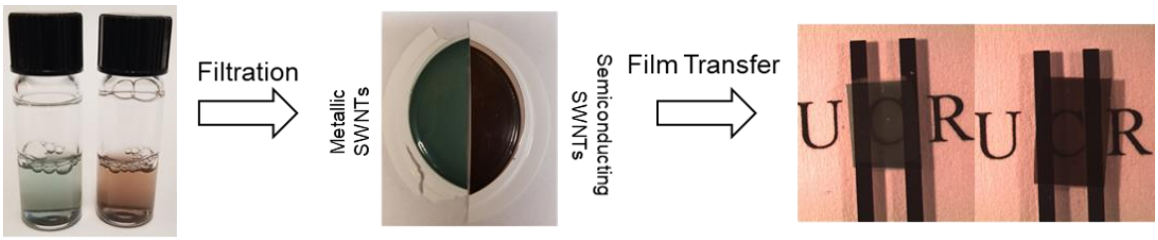

Figure 1.3: Filtration method to form SWNT thin films. (left) Solutions of SC- and MT-SWNTs are (middle) filtered through a membrane to form a film. These films can be transferred onto various substrates, (right) in this case glass.

Due to their unique properties, CNTs have been explored for a number of uses including field effect transistors,[16] semi-transparent electrodes,[15] drug delivery,[17] strong composite materials,[18] sensors,[19] solar cells,[20] hydrogen storage,[21] supercapacitors,[22] batteries,[23] and many others.

1.3 Introduction to Phenalenyl Based Neutral Radical Conductors

As discussed above, another group of organic electronic materials are composed of small molecules. A special subset of these materials, pioneered by R.C. Haddon, are classified as neutral radical conductors.[24] Since the discovery of a long lived radical in triphenylmethyl, much effort has gone into studying their reactivity as well as their properties as materials.[25] These small molecules contain an unpaired electron, i.e. radical, as the charge carrier for conduction. While there are a number of neutral radical conductors,[26-29] we will focus on those derived from phenalenyl. Phenalenyl is composed of ~3 benzene rings fused together in a triangle like shape. Phenalenyl is an odd alternant

hydrocarbon (OAH). Like other alternant hydrocarbons, phenalenyl has symmetrical bonding and antibonding orbitals. However, since phenalenyl has an odd number of carbons, it has an additional nonbonding orbital located in between the two. This nonbonding orbital can be empty (cation), singly occupied (radical), or doubly occupied (anion). Due to the orbital being nonbonding, these three states cause little change in the structure and thus should make good conductors (Figure 1.4).[24,30]

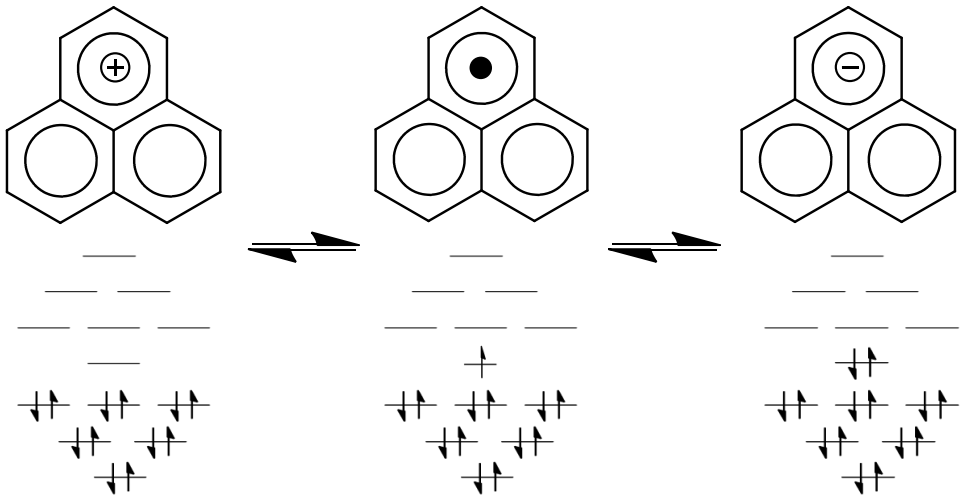

Figure 1.4: Phenalenyl in its cation (left), neutral radical (middle), and anionic (right) state along with accompanying orbitals.

While phenalenyl should in theory make a good conductor, a large problem arises as the phenalenyl neutral radicals can partner up and sigma-dimerize. This leads to the decomposition of phenalenyl and a resulting insulating state.[31,32] To circumvent this issue, two molecules of a derivative of phenalenyl (9-hydroxyl-phenalenone) can be spiro-conjugated through a bridging boron. This leads to a compound that (generally) does not undergo sigma-dimerization and contains a quarter filled band structure.[33,34]

While phenalenyl based conductors we first proposed in 1975, it wasn't until 1999 that the first example was reported.[35] One of the more difficult tasks was the crystallization of the radical. During synthesis, the compounds are created as the cationic salts. Thus, to crystallize the neutral radicals the cationic salts must be reduced then crystallized. The final solution was the use of specially created H-cells in which the cationic salt would be filled in one side, and a chemical reductant in the other. When the cell is inverted the reductant slowly diffuses through the glass frit resulting in reduction and crystal growth at the frit (Figure 1.5).

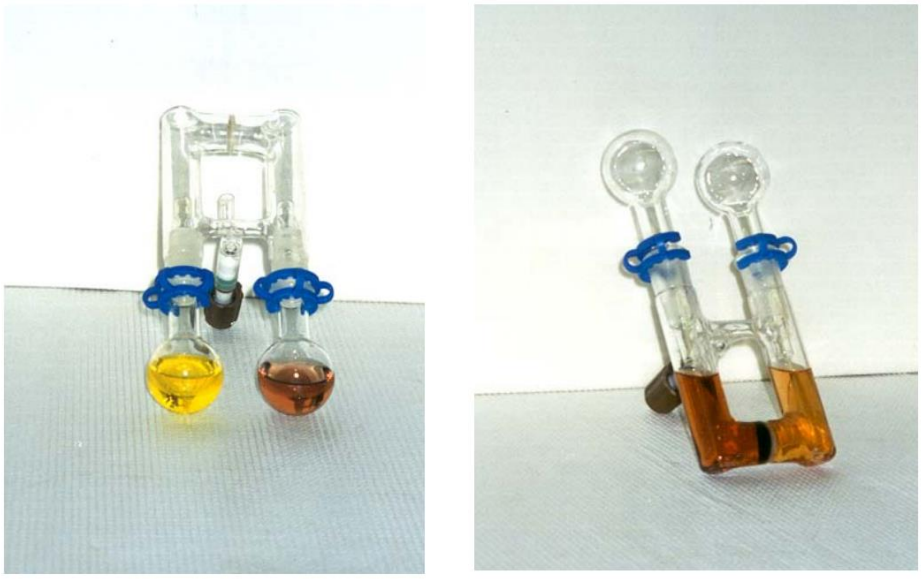

Figure 1.5: An H-cell is used to grow crystals of phenalenyl based neutral radical conductors. (left) The round bottoms are filled with the precursor cation (red-brown colored solution) and a chemical reductant (yellow solution). The cell is inverted and within a few days to a week crystal are grown at the frit (black color).

Since the first crystallization of a phenalenyl-based neutral radical molecular conductor a number of others have also been synthesized, crystallized, and characterized with many possessing unique properties. Some examples are shown in Figure 1.6.[36-42]

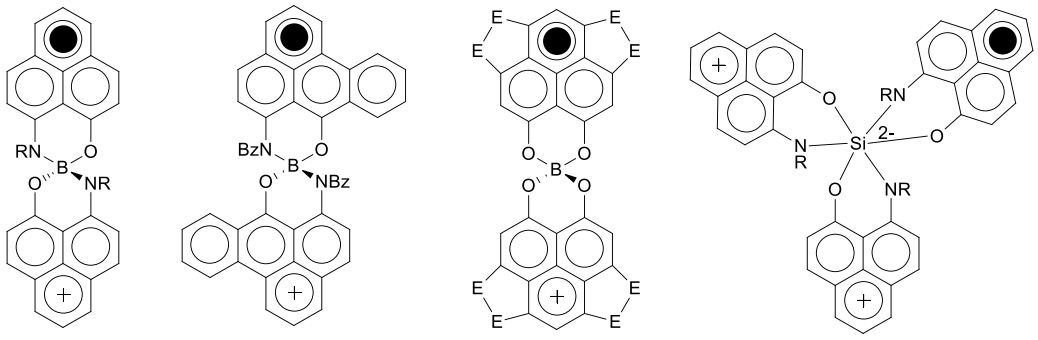

Figure 1.6: Examples of phenalenyl based neutral radical conductors (R = various alkyl chains, E = sulfur or selenium)

One of the most interesting is the butyl-substituted compound presented in Figure 1.6, far left (R = butyl). This compound shows a bistability in the form of a hysteretic phase transition that occurs in the magnetism, electrical conductivity and the optical properties of the material. This material and its phase transition, along with the manipulation of it, is explored further in Chapter 4.[36,43-45]

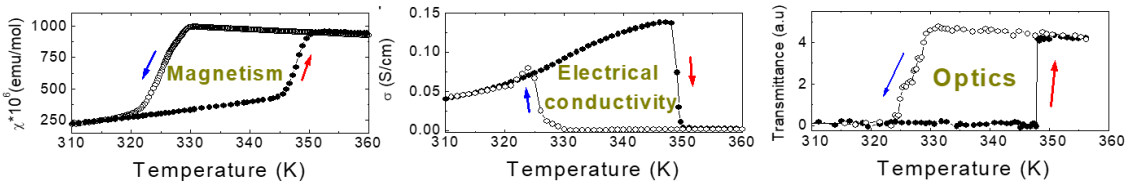

Figure 1.7: Bistability in a butyl substituted phenalenyl based neutral radical conductor being shown in the (left to right) magnetic, electrical conductivity and optical properties

1.4: Electrical Conductivity of Phenalenyl Based Neutral Radical Crystals

One of the major motivations for the construction and study of neutral radical conductors is the discovery of a molecular metal.[24] One characteristic of a metal is high conductivity and a decrease of conductivity as temperature is increased while semiconductors possess intermediate conductivities and an increase of conductivity as temperature is increased. This is explained through the band structure of both metals and semiconductors. Metals possess no band gap at the Fermi level, and thus electrons and holes are free to move throughout the material. In such a case, an increase in temperature results in more molecular vibrations that scatter free carriers through electron-phonon interaction, decreasing the free carriers mean free path and thus reducing the

conductivity of the metals. Semiconductors possess a band gap and thus electrons and holes are not free to move throughout the material at low temperatures. In order to conduct, semiconductors require thermal excitation of valence electrons into the conduction band to form free charge carriers. Thus, as temperature is increased, more electrons are excited, and conductivity is increased.

While neutral radical conductors were predicted to behave as molecular metals, thus far all phenalenyl based neutral radical conductors have behaved as semiconductors. Figure 1.8a shows the band structure calculations of a phenalenyl based neutral radical conductor conducted by Robert Haddon.[35,46] In the quarter filled band structure (bandwidth, W~0.5eV), there is a finite density of states at the Fermi level, and thus the material would be predicted to behave as a metal. However, Figure 1.8b shows the conductivity of a phenalenyl based neutral radical conductor, and it can be seen that the conductivity (0.05 S/cm) is relatively low and increases with increasing temperature. Thus, the material is behaving as a semiconductor. The explanation for this is the limitation of the tight binding approximation used in the band structure calculations; it does not take into account electron-electron interactions. In order to conduct, a phenalenyl molecule must, at some point, contain a filled nonbonding orbital. The electrons in this filled nonbonding orbital repel one another (on site coulombic correlation energy, *U*) creating a band gap resulting in a semiconducting material (Figure 1.8c). The on-site coulombic correlation energy can be estimated through cyclic

voltammetry and is related to the band gap of the material. The band gap of the material can also be estimated from the activation energy and optical measurements, however, their relation to one another in phenalenyl based neutral radical conductors is complicated and poorly understood. It is suggested that the transition of a Mott insulator to a metallic state is controlled by the bandwidth (W) -coulombic correlation energy (U) ratio (W/U).[35,46] However, a strategy of maximizing W and reducing U has yet to result in a metallic state.[35,46,47]

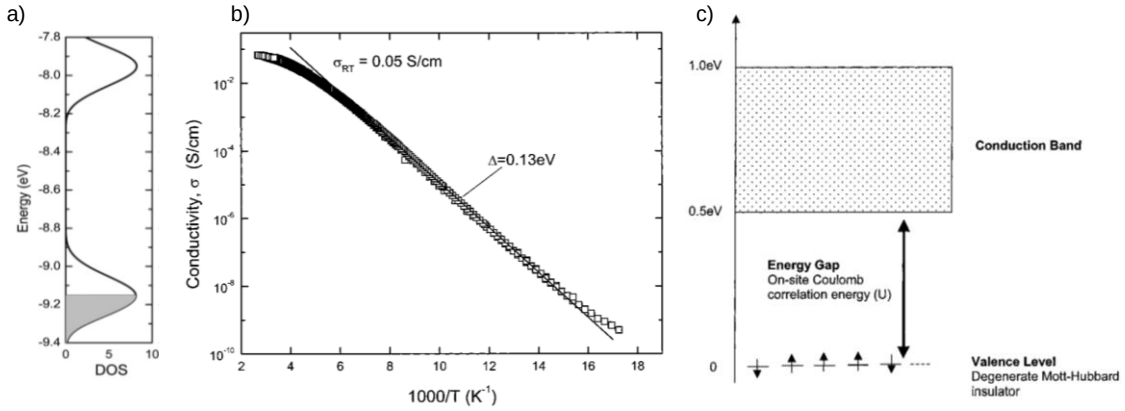

Figure 1.8: (a) Band structure of a phenalenyl based neutral radical conductor predicting a metallic compound; (b) Arrhenius plot of the conductivity as a function of temperature showing semiconductor behavior and (c) the band gap created by the on-site coulomb correlation energy explaining the semiconducting properties.[35,46]

1.5: Structural Motifs in Phenalenyl Based Neutral Radical Conductors

The phenalenyl neutral radicals were discussed above in terms of single molecules, while their solid state properties are heavily influenced by their intermolecular interactions which are mostly controlled through their crystal packing structure. Phenalenyl based neutral radical conductors pack in one of 3

general motifs; dimeric, resonating valence bond and monomeric (Figure 1.9). The first packing motif, dimeric, consists of dimers of neutral radicals. These dimers pancake-bond to one another and, as a result, contain short intradimer interactions which are shorter than the van der Waals distance of carbon-carbon bonds (<3.4 Å). As a result of their pi-dimerization, the spins pair antiferromagnetically into singlet low spin (LS) state which results in magnetism similar to simple diamagnetic molecules (spin per molecule equal to zero over all temperature ranges) (Figure 1.9 left).[36,43,48]

The second, and arguably most interesting case, is that of the resonating valence bond (RVB) motif. Initially proposed by Anderson and Pauling,[49-51] it was first built as a model to explain superconductivity in cuprates. The name draws inspiration from the resonating bonds found in benzene, in which the equal bond distances of the six carbons are explained as the combination of 2 resonance structures with alternating double bonds. Similar to benzene, neutral radical crystals with RVB structures have intermolecular distances which are equal and less than the van der Waals distance of carbon-carbon bonds (<3.4 Å). These compounds contain temperature-independent Pauli paramagnetism, which is characteristic of a metal and is manifested as an increase in spin per molecule as temperature is increased. Neutral radicals with RVB packing motifs often display the highest conductivities.[33,42,46,48]

The final motif, monomeric, is usually made up of molecules with bulky substituents. Here the intermolecular distances are often large (>3.4 Å) and the

spins on each molecule are noninteracting, or independent. As a result, magnetic measurements in this case show one Curie spin per molecule over wide temperature ranges (until low temperatures, where long distance interactions often cause antiferromagnetic pairing).[35,52]

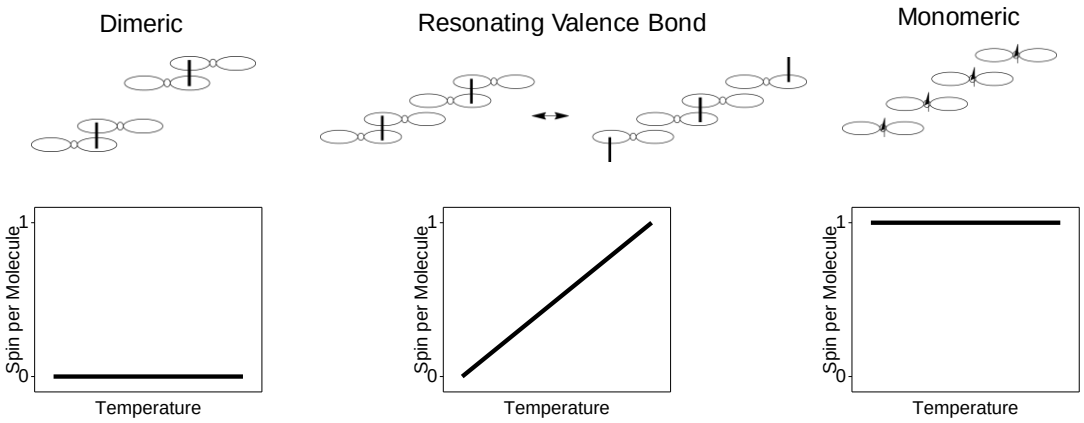

Figure 1.9: Common packing motifs and their magnetic properties in terms of spin per molecules as a function of temperature. (left) Dimeric motif, with short intradimer spacing and large interdimer spacing, displaying antiferromagnetic coupling. (middle) RVB motif, with equal intermolecular contacts less than 3.4 Å and temperature-independent Pauli paramagnetism. (right) Monomeric motif with large intermolecular spacing (>3.4 Å) displaying 1 Curie spin per molecule over all temperature ranges.

1.4: Introduction to Doping:

Despite the first phenalenyl-based neutral radicals being conductors, it was importance to find a way to enhance their electrical conductivity. One advantage of semiconducting materials is that their properties can be controlled, often times through doping.[53] Non-doped semiconductors, i.e. intrinsic semiconductors, often have low conductivities and thus dopants must be introduced to increase the conductivities for most practical purposes. Electrical conduction is the process of charge moving throughout a material. In most

intrinsic semiconductors, few electrons are able to be thermally excited from the valence band to the conduction band due to the band gap in between being relatively large and thus the number of available charges that can move throughout the material (free carrier concentration) is quite low resulting in a low conductivity. Doping refers to the addition of impurities into a material to augment the electrical, optical, and structural properties.

One of the most popular examples of doping is the substitutional doping found in extrinsic silicon which helps form the basis of modern day computers. Substitutional doping refers to the replacement of a host with that of a dopant. Silicon, a group 4 element, can be doped with group 3 or group 5 elements. Since group 3 elements, such as boron, contain one less electron in their valence shell than silicon, they insert holes (positive charge carriers) into the lattice and produce p-type semiconductors. On the other hand, group 5 elements, such as phosphorous, contain one more electron in their valence shell than silicon and thus insert electrons (negative charge carriers) into the lattice and produce n-type semiconductors. An example of substitutional doping found in silicon is shown in Figure 1.10.

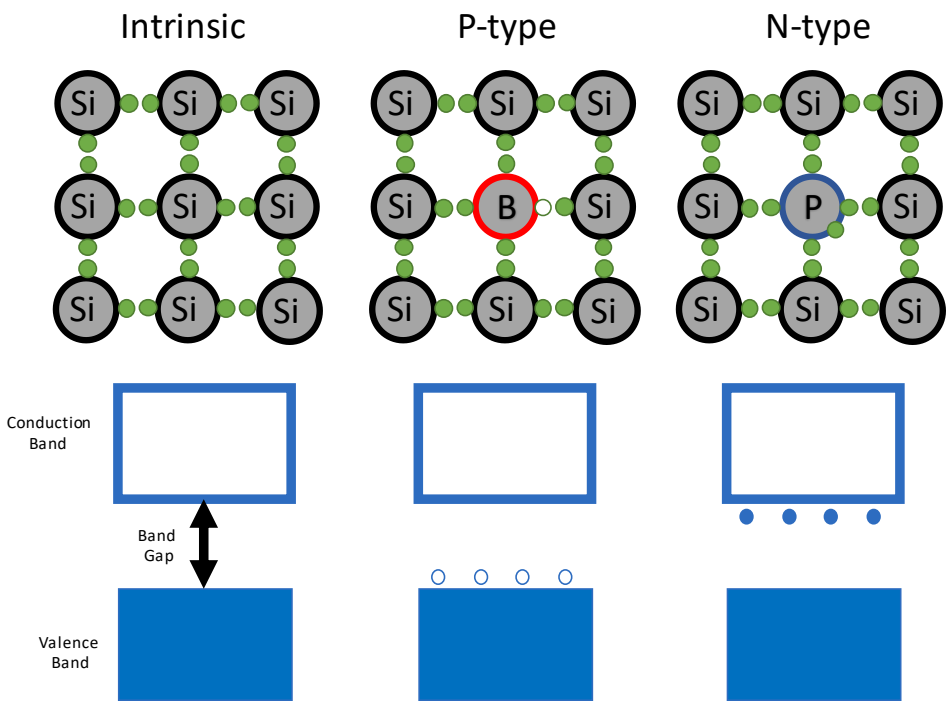

Figure 1.10: (Left) Intrinsic silicon, (middle) p-type silicon, and (right) n-type silicon and their associated band structures.

While substitutional doping is often found in inorganic semiconductors, interstitial doping, in the form of chemical or electrochemical, is more often used in organic semiconductors, particularly polymers. As opposed to substitutional doping, where the dopant takes the place of the host, interstitial doping refers to the addition of impurities into open spaces surrounding the host. Common examples of interstitial chemical doping include the intercalation of alkali metals such as lithium. Due to the low electronegativity of alkali metals, they will donate their electron to the conduction band of the material thus producing n-type semiconducting materials. Popular examples of this include the superconducting alkali doped C_{60} fullerenes[54] and semiconducting alkali doped polyacetylene.[55]

Since the earth's atmosphere is oxidizing, it can produce interstitially chemically doped p-type materials. Interstitial doping can be further controlled through electrochemical doping, often seen in electrochromic devices.[56] Here the semiconducting material is placed on an electrode, with a counter electrode opposite and electrolyte in between for charge balance. When a potential is applied to the polymer, electrons or holes can be injected from the electrode to the material thus n- or p-type doping it with the opposite charge electrolyte occupying interstitial sites for charge balance. This process is further explored in Chapter 2 for a case of carbon nanotubes.

This dissertation is organized in the following way. Chapter 2 discusses the field of electrochromic materials with SWNTs as an example and discusses how electrochemical doping is used to control their optical properties. Chapter 3 and 4 focus on neutral radical conductors and the effects of substitutional doping on them. Chapter 5 lays the foundation towards more effective, energy matched dopants. Chapter 6 shows how phenalenyl based molecules, much like SWNTs, also contain very interesting electrochromic properties.

1.5: References

1) Kulkarni, A. P.; Tonzola, C. J.; Babel, A.; Jenekhe, S. A. *Chem. Mater.* **2004**, *16*, 4556.

2) Yamashita, Y. *Sci. Technol. Adv. Mater.* **2009**, *10*.

3) Lin, Y. Z.; Li, Y. F.; Zhan, X. W. *Chem. Soc. Rev.* **2012**, *41*, 4245.

4) Iijima, S. *Nature* **1991**, *354*, 56.

5) Treacy, M. M. J.; Ebbsen, T. W.; Gibson, J. M. *Nature* **1996**, *381*, 678.

6) Wong, E. W.; Sheehan, P. E.; Lieber, C. M. *Science* **1997**, *277*, 1971.

7) Hone, J.; Whitney, M.; Piskoti, C.; Zettl, A. *Physical Review B* **1999**, *59*, R2514.

8) Itkis, M. E.; Borondics, F.; Yu, A.; Haddon, R. C. *Nano Lett.* **2007**, *7*, 900.

9) Wang, F.; Itkis, M. E.; Bekyarova, E.; Haddon, R. C. *Nat. Photonics* **2013**, *7*, 459.

10) Itkis, M. E.; Niyogi, S.; Meng, M.; Hamon, M.; Hu, H.; Haddon, R. C. *Nano Lett.* **2002**, *2*, 155.

11) Javey, A.; Guo, J.; Wang, Q.; Lundstrom, M.; Dai, H. *Nature* **2003**, *424*, 654.

12) *Carbon Nanotubes: Synthesis, Structure, Properties and Applications*; Dresselhaus, M. S.; Dresselhaus, G.; Avouris, P., Eds.; Springer-Verlag: Berlin, 2001; Vol. 80.

13) Wildoer, J. W. G.; Venema, L. C.; Rinzler, A. G.; Smalley, R. E.; Dekker, C. *Nature (London)* **1998**, *391*, 59.

14) Odom, T. W.; Huang, J.-L.; Kim, P.; Lieber, C. M. *Nature (London)* **1998**, *391*, 62.

15) Wu, Z.; Chen, Z.; Du, X.; Logan, J. M.; Sippel, J.; Nikolou, M.; Kamaras, K.; Reynolds, J. R.; Tanner, D. B.; Hebard, A. F.; Rinzler, A. G. *Science* **2004**, *305*, 1273.

16) Tans, S. J.; Verschueren, A. R. M.; Dekker, C. *Nature* **1998**, *393*, 49.

17) Hampel, S.; Kunze, D.; Haase, D.; Kramer, K.; Rauschenbach, M.; Ritscbel, M.; Leonbardt, A.; Thomas, J.; Oswald, S.; Hoffmann, V.; Buechner, B. *Nanomedicine* **2008**, *3*, 175.

18) Coleman, J. N.; Khan, U.; Gun'ko, Y. K. *Adv. Mater.* **2006**, *18*, 1.

19) Bekyarova, E.; Davis, M.; Burch, T.; Itkis, M. E.; Zhao, B.; Sunshine, S.; Haddon, R. C. *J. Phys. Chem. B* **2004**, *108*, 19717.

20) Rowell, M. W.; Topinka, M. A.; McGehee, M. D.; Prall, H. J.; Dennler, G.; Sariciftci, N. S.; Hu, L. B.; Gruner, G. *Appl. Phys. Lett.* **2006**, *88*, 233506.

21) Dillon, A. C.; Jones, K. M.; Bekkedahl, T. A.; Kiang, C. H.; Bethune, D. S.; Heben, M. J. *Nature* **1997**, *386*, 377.

22) Frackowiak, E.; Beguin, F. *Carbon* **2001**, *39*, 937.

23) Landi, B. J.; Ganter, M. J.; Cress, C. D.; DiLeo, R. A.; Raffaelle, R. P. *Energy Environ. Sci.* **2009**, *2*, 638.

24) Haddon, R. C. *Nature* **1975**, *256*, 394.

25) Gomberg, M. *J. Am. Chem. Soc.* **1900**, *22*, 757.

26) Tian, D.; Winter, S. M.; Mailman, A.; Wong, J. W. L.; Yong, W. J.; Yamaguchi, H.; Jia, Y. T.; Tse, J. S.; Desgreniers, S.; Secco, R. A.; Julian, S. R.; Jin, C. Q.; Mito, M.; Ohishi, Y.; Oakley, R. T. *J. Am. Chem. Soc.* **2015**, *137*, 14136.

27) Yu, X.; Mailman, A.; Lekin, K.; Assoud, A.; Robertson, C. M.; Noll, B. C.; Campana, C. F.; Howard, J. A. K.; Dube, P. A.; Oakley, R. T. *J. Am. Chem. Soc.* **2012**, 2264

28) Kubo, T. *Chem. Lett.* **2015**, *44*, 111.

29) Tian, Y.; Uchida, K.; Kurata, H.; Hirao, Y.; Nishiuchi, T.; Kubo, T. *J. Am. Chem. Soc.* **2014**, *136*, 12784.

30) Uchida, K.; Kubo, T. *J Syn. Org. Chem. JPN* **2016**, *74*, 1069.

31) Uchida, K.; Ito, S.; Nakano, M.; Abe, M.; Kubo, T. *J. Am. Chem. Soc.* **2016**, *138*, 2399.

32) Small, D.; Rosokha, S. V.; Kochi, J. K.; Head-Gordon, M. *J. Phys. Chem. A* **2005**, *109*, 11261.

33) Bag, P.; Itkis, M. E.; Pal, S. K.; Donnadieu, B.; Tham, F. S.; Park, H.; Schleuter, J. A.; Siegrist, T.; Haddon, R. C. *J. Am. Chem. Soc.* **2010**, *132*, 2684.

34) Liao, P.; Itkis, M. E.; Oakley, R. T.; Tham, F. S.; Haddon, R. C. *J. Am. Chem. Soc.* **2004**, *126*, 14297.

35) Chi, X.; Itkis, M. E.; Patrick, B. O.; Barclay, T. M.; Reed, R. W.; Oakley, R. T.; Cordes, A. W.; Haddon, R. C. *J. Am. Chem. Soc.* **1999**, *121*, 10395.

36) Chi, X.; Itkis, M. E.; Kirschbaum, K.; Pinkerton, A. A.; Oakley, R. T.; Cordes, A. W.; Haddon, R. C. *J. Am. Chem. Soc.* **2001**, *123*, 4041.

37) Bag, P.; Pal, S. K.; Itkis, M. E.; Sarkar, A.; Tham, F. S.; Donnadieu, B.; Haddon, R. C. *J. Am. Chem. Soc* **2013**, *135*, 12936.

38) Bag, P.; Itkis, M. E.; Pal, S. K.; Bekyarova, E.; Donnadieu, B.; Haddon, R. C. *Crystals* **2012**, *2*, 446

39) Sarkar, A.; Pal, S. K.; Itkis, M. E.; Tham, F. S.; Haddon, R. C. *J. Mater. Chem.* **2012**, *22*, 8245.

40) Sarkar, A.; Pal, S. K.; Itkis, M. E.; Liao, P.; Tham, F. S.; Donnadieu, B.; Haddon, R. C. *Chem. Mater.* **2009**, *21*, 2226

41) Pal, S. K.; Itkis, M. E.; Tham, F. S.; Reed, R. W.; Oakley, R. T.; Haddon, R. *J. Am. Chem. Soc.* **2008**, *130*, 3942

42) Pal, S. K.; Itkis, M. E.; Tham, F. S.; Reed, R. W.; Oakley, R. T.; Haddon, R. C. *Science* **2005**, *309*, 281.

43) Itkis, M. E.; Chi, X.; Cordes, A. W.; Haddon, R. C. *Science* **2002**, *296*, 1443.

44) Fumanal, M.; Mota, F.; Novoa, J. J.; Ribas-Arino, J. *J. Am. Chem. Soc.* **2015**, *137*, 12843.

45) Fumanal, M.; Novoa, J. J.; Ribas-Arino, J. *Chem. Eur. J.* **2017**, *23*, 7772.

46) Mandal, S. K.; Samanta, S.; Itkis, M. E.; Jensen, D. W.; Reed, R. W.; Oakley, R. T.; Tham, F. S.; Donnadieu, B.; Haddon, R. C. *J. Am. Chem. Soc.* **2006**, *128*, 1982.

47) Pal, S. K.; Itkis, M. E.; Reed, R. W.; Oakley, R. T.; Cordes, A. W.; Tham, F. S.; Siegrist, T.; Haddon, R. C. *J. Am. Chem. Soc.* **2004**, *126*, 1478.

48) Pal, S. K.; Itkis, M. E.; Tham, F. S.; Reed, R. W.; Oakley, R. T.; Donnadieu, B.; Haddon, R. C. *J. Am. Chem. Soc.* **2007**, *129*, 7163.

49) Anderson, P. W. *Mater. Res. Bull.* **1973**, *8*, 153.

50) Anderson, P. W. *Science* **1987**, *235*, 1196.

51) Pauling, L. *Nature* **1948**, *161*, 1019.

52) Mandal, S. K.; Itkis, M. E.; Chi, X.; Samanta, S.; Lidsky, D.; Reed, R. W.; Oakley, R. T.; Tham, F. S.; Haddon, R. C. *J. Am. Chem. Soc.* **2005**, *127*, 8185.

53) Sze, S. M. *Physics of Semiconductor Devices*; Wiley: New York, 1981.

54) Hebard, A. F.; Rosseinsky, M. J.; Haddon, R. C.; Murphy, D. W.; Glarum, S. H.; Palstra, T. T. M.; Ramirez, A. P.; Kortan, A. R. *Nature* **1991**, *350*, 600

55) Jow, T. R.; Shacklette, L. W. *J. Electrochem. Soc.* **1988**, *135*, 541.

56) Beaujuge, P. M.; Reynolds, J. R. *Chem. Rev.* **2010**, *110*, 268.

Chapter 2: Carbon Nanotube Electro-Optical Devices

2.1: Introduction to Opto-Electronic Devices

Opto-electronic materials are those which can change their optical properties upon the application of an external electric field. Electrochromic devices[1] are a subclass of electro-optical devices and many are based on electrochemical capacitor designs which use electrochemical doping to control the optical properties of the material as discussed in Chapter 1. Figure 2.1 shows a diagram of a typical electrochromic device. In between clear substrates are transparent conductive electrodes, an ion storage layer on one side and electrochromic material on the other with an electrolyte in between. Upon application of a potential, the ions diffuse towards their oppositely charged electrodes and dope the electrochromic material. In response, the electrochromic material goes from a bleached to colored state or vice-versa.

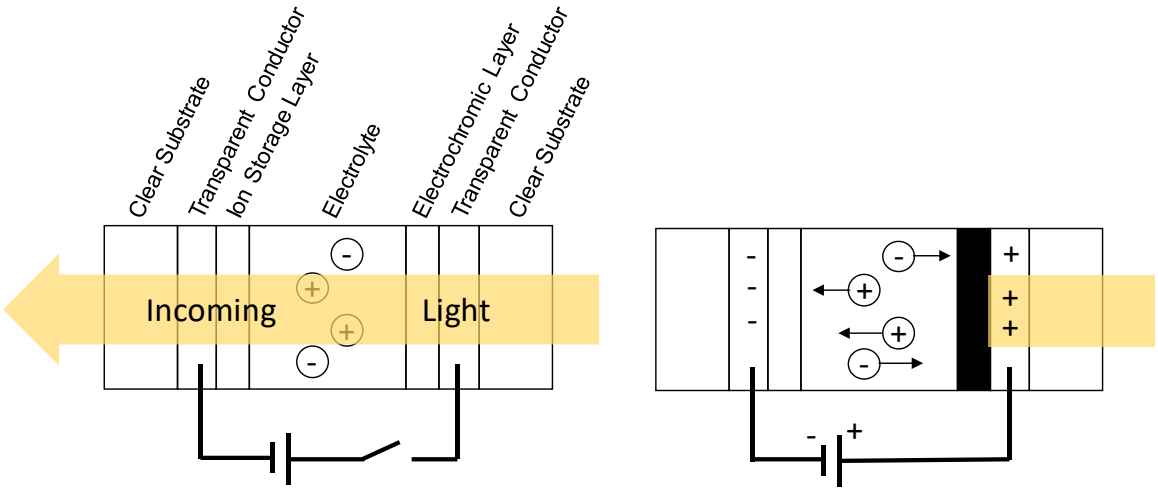

Figure 2.1: Schematic of an electrochromic device in its (left) bleached and (right) colored state.

The uses of such materials range from smart windows,[2,3] wearable electronics, artificial reconfigurable camouflage[4-6] and electro-optical shutters[7] among many others.[8,9] For example, smart windows would reduce energy costs of buildings by providing natural heating in their bleached state and block incoming heat from light in their colored state. Wearable electronics could display information when needed and be transparent when not in use.

The most explored component of electrochromic devices is the electro-optical materials themselves. Different materials can vary in the spectral range in which they can modulate, the degree to which they can modulate, and the response times of the devices. Depending on the particular use, some properties are more important than others. For example, in smart windows the spectral range and degree of modulation are very important while slow response times are acceptable.[2,3] Electrochromic devices are a good match for this as their response times are generally in the tens to hundreds of seconds,[10] but some nanostructured materials are able to achieve response times in the millisecond range.[11-13] For other uses, such as electro-optical shutters, all three (range, modulation, speed) are important and thus the optimization of these parameters is receiving attention.[1]

2.2: Electro-Optical Properties of Carbon Nanotube Thin Films:

Carbon nanotubes, due to their unique electronic properties, have garnered interest for use in electrochromic devices. The requirement for transparent conductive layers has been the main push for CNTs in

electrochromic devices. The transparent electrodes are typically made of indium tin oxide (ITO) due to its high conductivity and transparency. However, the rising cost of ITO had incentivized exploring other materials. One of the explored alternatives are CNT thin films. Due to their high conductivity and easy to form thin films, as discussed in Chapter 1, they have been successfully used as transparent electrodes in both rigid and flexible electrochromic devices as well as other electronics.[14,15] Recently, metallic (MT-) SWNTs have also been used as the active electrochromic layer. It was shown that MT-SWNT thin films could act as both the conductive and electrochromic layer simultaneously, modulating visible light to go from green or pink films to yellow. Like many other electrochromic materials, the MT-SWNT showed slow response times on the order of seconds.[16]

As previously discussed, both semiconducting (SC-) SWNTs and MT-SWNTs have interesting optical properties, some of which have been explored in electrochromic devices as discussed above. Like many other properties of SWNTs, the optical properties are also controlled by the chirality and diameter of the SWNTs. In the visible-near infrared spectral range SC-SWNTs have two main absorption bands related to the electronic transitions (labeled S_{11} and S_{22}) between the pairs of van Hove singularity peaks in the valence and the conduction band, while MT-SWNTs have one (labeled M_{11}) (Figure 2.2).

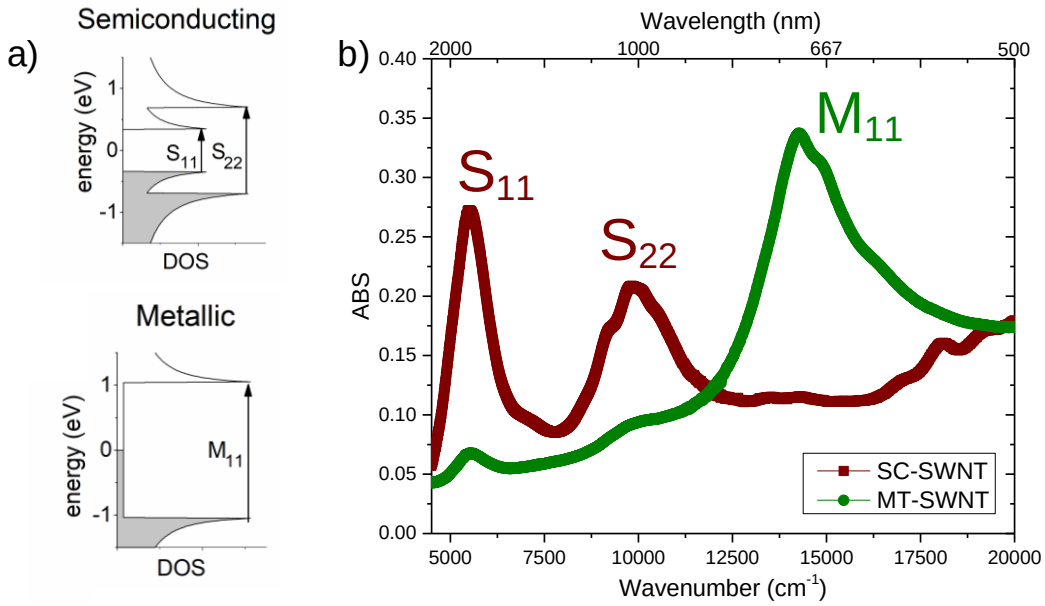

Figure 2.2: (a) Band diagrams for SC- and MT-SWNTs showing interband transitions and (b) corresponding absorptions shown in thin films.

These interband transitions can be modulated by both solid state and electrolyte-controlled gating (electrochemical doping). By applying an electric field to the SWNTs the position of the Fermi level, which controls the concentration of electrons and holes in the valence and conduction bands, can be adjusted. The interband transitions absorb most when the valence band is completely filled and the conduction band is empty. Both p- and n-doping will suppress the transition. Figure 2.3 shows the modulation of the Fermi level and its effect on the absorbance spectra of a thin film of SC-SWNTs.[17-22] It should be noted that the optical properties are directly tied in with the electrical (conductivity) properties which are used for the development of the SWNT-based field-effect transistors (FETs) which have some advantages as compared to the current day silicon-based FETs.[23]

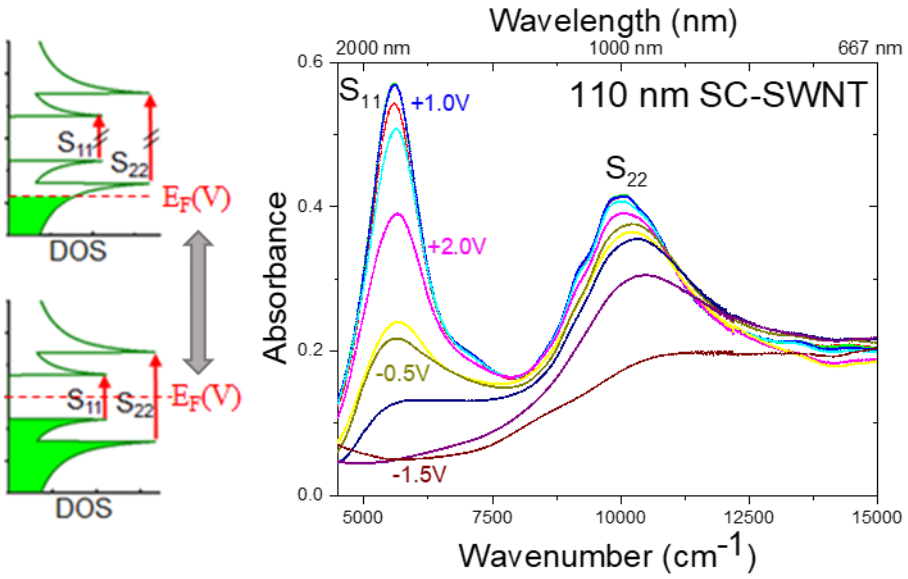

Figure 2.3: (left) Band diagram of SC-SWNTs showing suppression/regeneration of the interband transitions through gating and the (right) resultant absorbance spectra showing the modulation of absorbance from gating.

2.3: SWNT Thin Film Electrochromic Devices

Recent work in our group has produced an all-SWNT thin film electrochromic device where the active electrochromic layer was a thin film of SC-SWNTs with a MT-SWNT thin film counter electrode and ionic liquid electrolyte (Figure 2.4a).[24] Ionic liquids (ILs) were used as the electrolyte as they can lead to an accumulation of high charge carrier density at the IL – solid material interface. The advantage of using SC-SWNTs is that the S_{11} transition occurs around 1800 nm which is in the range of fiber optic communication bands as well as some other uses.[25,26] With the spectral range being determined by the material used, the response time and light modulation was explored. Modulation depth (*MD*) is used to quantify the amount of light modulation and is defined as:[27]

$$MD = 10 \log \frac{T_{BL}}{T_{COL}}$$

Where T_{BL} is the transmittance in the bleached state and T_{col} is the transmittance in the colored state. With very thin films on the order of a few tens of nanometers the devices showed *MD* of ~3-4 dB. The devices also showed very fast switching times on the order of a few milliseconds. To achieve higher *MD* the thicknesses of the electrochromic SC-SWNT thin films were increased. With increasing film thicknesses, *MD* of ~6 dB (~4 times modulation of transmittance) was reached, however, a significant slowdown of the response time was observed with a response time increasing to over 30 ms.(ref) In order to develop a competitive, highly efficient electrochromic device, higher depths of modulation are required without sacrificing the response time. However, past research did not provide a pathway for maintaining the speed of operation for thicker SWNT thin film devices as the increasing response time was originally attributed to the increasing diffusion time of the ions when the thickness of the SC-SWNT film increases.[24]

The research presented in this dissertation started with the further increase of the thickness of the electrochromic SC-SWNT thin film layer in order to achieve *MD* exceeding 10 dB, and to find a way to maintain the fast speed of response. The response time of the device can be observed in terms of its bandwidth (BW), which is defined as the frequency *f*(50%) at which the amplitude of the response is decreased by 50%.[27] As shown in Figure 2.4 b,c the bandwidth decreases from 135 Hz to 5.5 Hz for the 72 nm and 440 nm thick SC-

SWNT films respectively. This slowdown is also shown in the profile of the response as it goes from square-wave to triangular as shown in figure 2.4d.

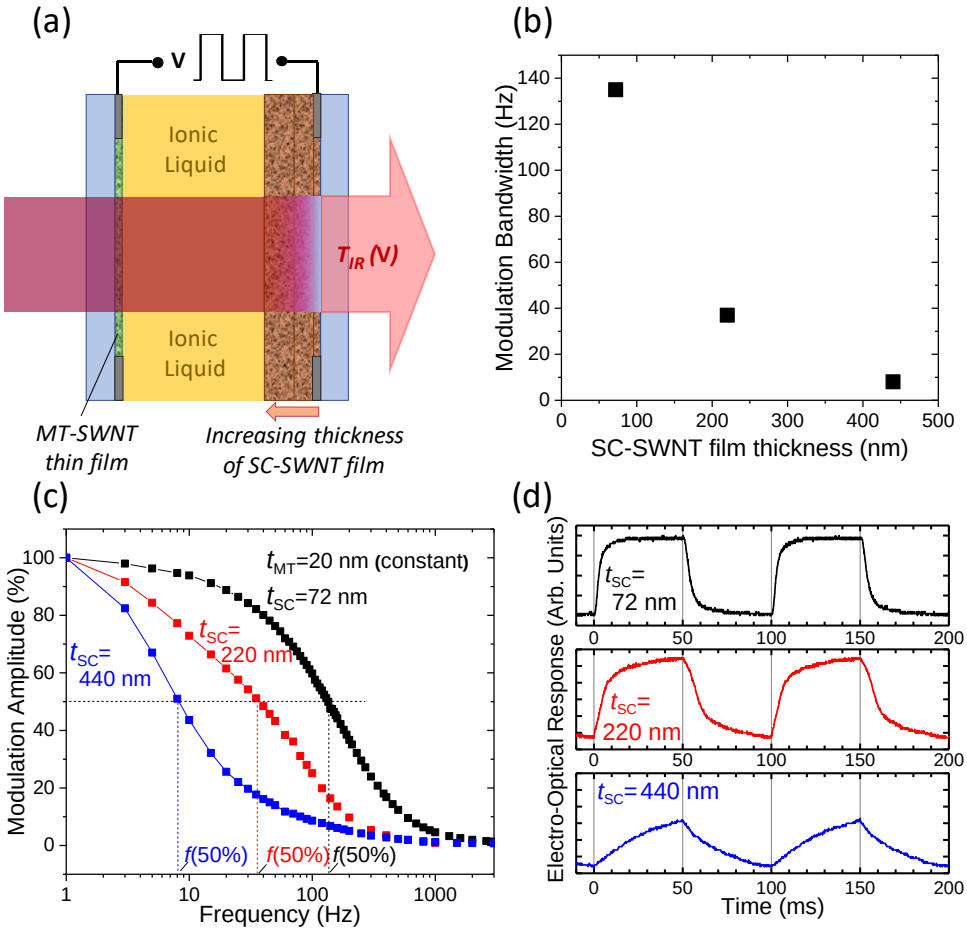

Figure 2.4: (a) Schematic of the all-SWNT device with increasing thickness of the SC-SWNT layer to increase light modulation. (b) Modulation bandwidth as a function of SC-SWNT film thickness. (c) Frequency dependencies of the amplitude of electro-optical modulation as a function of SC-SWNT film thickness. (d) Oscilloscope traces of the SWNT electrochromic cell with various thickness of the SC-SWNT film.

As previously discussed, the optical properties of SC-SWNTs are determined by their chirality and diameter. In our previous reports, SC-SWNTs of a wide diameter range were used (1.2-1.7 nm), resulting in a relatively broad absorption

range. Very recently, it was shown that by using sorted SC-SWNTs of very narrow diameter distribution and, ultimately, of single chirality, electrochromic notch filters are able to be constructed. In that work, a lateral configuration in which both the electrochromic layer and the SWNT counter-electrode were positioned on the same substrate was used and while very high modulation depths were reached (up to 43 dB), the device showed very slow response times from 200 ms for very thin films to over 20 seconds for thicker films.[28] Compared to our response times of a few milliseconds these devices were on the order of 100 to 10,000 times slower. This large difference in device response time, combined with the potential uses of such devices if faster response times could be achieved, demanded further study.

2.4: Fast, High Modulation Depth, Carbon Nanotube Based Electrochromics

While much effort has been given to various types and designs of materials for the electrochromic electrodes, the counter electrode is often ignored, and the use of platinum wire is not uncommon.[16,29,30] Through serendipity (accidental formation of a thicker MT-SWNT than intended), it was found that increasing the thickness of the MT-SWNT counter electrode helps remedy the slowdown of the devices as the active SC-SWNT layer is thickened. It was a counter-intuitive result as the slowdown of the response was originally associated with slower diffusion into the thicker SWNT layer. Based on this initial observation a new strategy on improving response time was developed. Figure 2.5 illustrates this strategy and the results. Figure 2.5a shows a schematic of the device with an

increase of the thickness of MT-SWNT counter electrode for fixed thickness of SC-SWNT electrochromic layer. As can be seen in Figure 2.5b, the bandwidth (speed) of the devices increases as the MT-SWNT is made thicker until a saturation point is reached after which an increase in the thickness of the MT-SWNT has no effect. Figure 2.5c shows the frequency dependencies of devices with 440 nm thick SC-SWNT films and various thicknesses of MT-SWNT films. It can be seen that the bandwidth is increased from ~ 10 Hz with the previous device configuration to ~110 Hz with the thicker MT-SWNT counter electrode. Figure 2.5d shows the corresponding oscilloscope traces at 10 Hz square-wave voltage modulation where the square shape is restored with thicker counter electrode films.

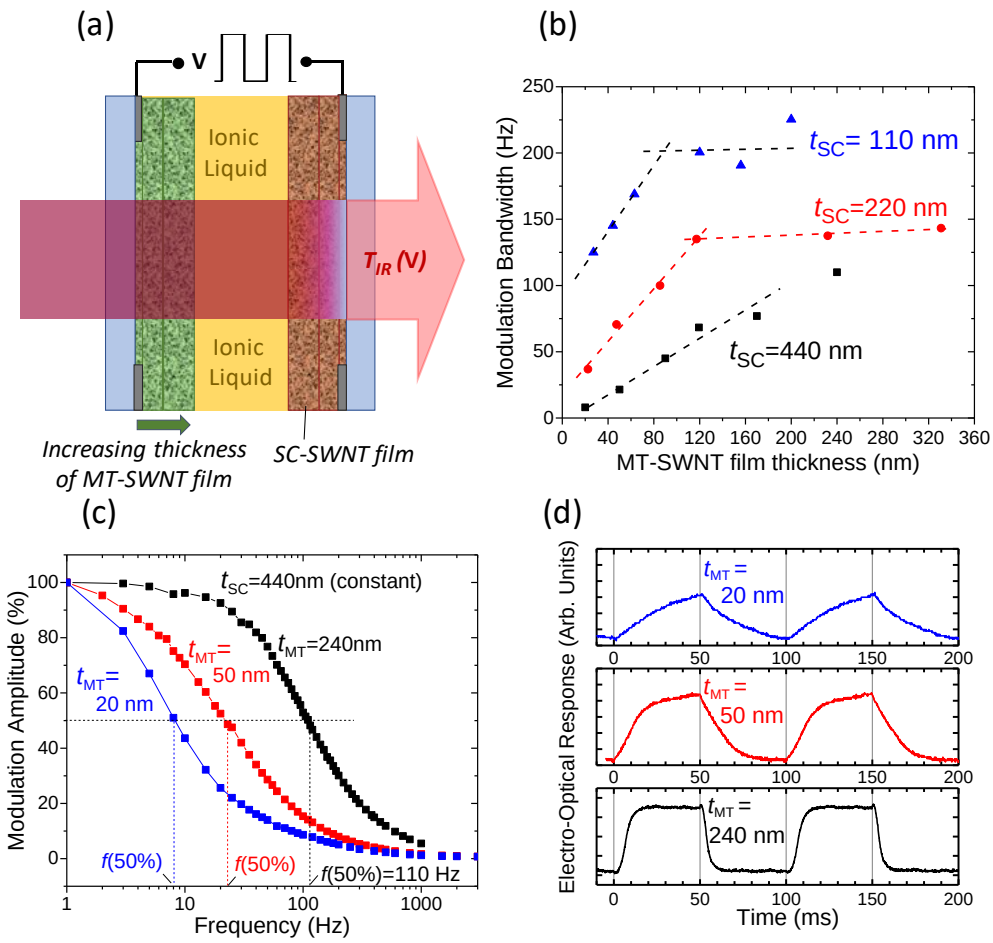

Figure 2.5: (a) Schematic of device with increasing MT-SWNT film thickness. (b) Bandwidth as a function of MT-SWNT film thickness for various SC-SWNT film thicknesses. (c) Frequency dependencies of 440 nm SC-SWNT films with various MT-SWNT counter electrodes. (d) Corresponding oscilloscope trances at 10 Hz showing regeneration of the square wave.

Along with fast devices, high modulation depths are also desired. Figure 2.6a shows the transmittance spectra of the bleached and colored states of various thicknesses of SC-SWNT thin films. As can be seen, thicker films of SC-SWNT darken both the bleached and colored state. Figure 2.6b shows modulation depth as a function of SC-SWNT film thickness and is linear

approaching 20 dB indicating that higher modulation levels could be achieved by further thickening the film which is significantly higher than the previously reported 3-6 dB with accompanying slower response times.[24] The modulation data in Figure 2.6b were taken with a fast InGaAs photodiode with a central wavelength of 1870 nm. However, the center of the S_{11} transition is at 1770 nm. Figure 2.6c shows the transmittance data taken using Cary 5000 monochromator with relatively slow data acquisition system. The observed transmittances at bleached and colored states are 45.9% and 0.44%, respectively, resulting in *MD* value 10*Log(45.9/0.44) exceeding 20 dB. Figure 2.6d shows an oscilloscope trace of the electrochromic switching showing response times of 3.2 ms to reach 63% of the signal and 6.5 ms to reach 90% of the original signal.

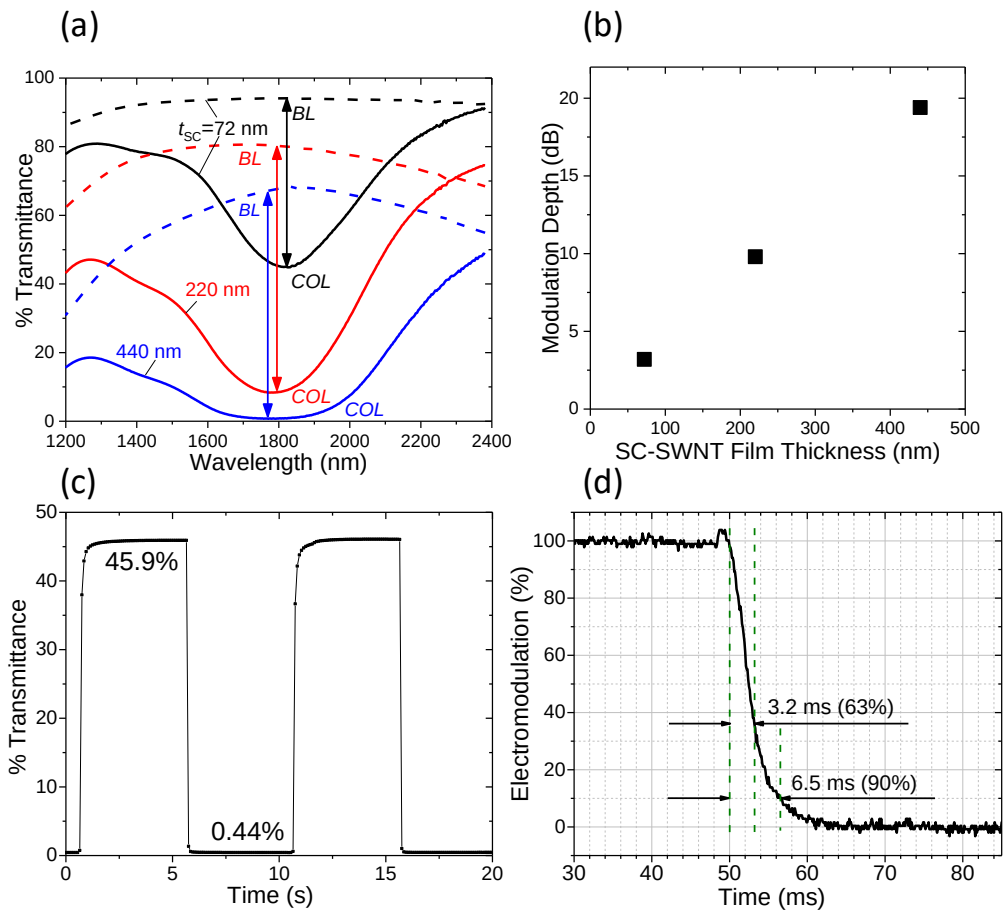

Figure 2.6: (a) Transmittance spectra of the bleached (dashed lines) and colored (solid lines) states of various thicknesses of SC-SWNTs. (b) Corresponding modulation depth at ~1870 nm. (c) Transmittance spectra at the center of the S_{11} transition located at 1770 nm and (d) corresponding response time.

From the above, we have shown that it is possible to achieve modulation depths of 20 dB by increasing the thickness of the SC-SWNT layer while maintaining the millisecond response time through counter electrode thickness. These results point to the importance of the counter electrode matching for improving dynamics of the electrochromic cell.

2.5: Understanding the Mechanism Behind the SWNT Thin Film Electrochromic Cell

To better understand the above findings, the SWNT electrochromic cell can be seen as a supercapacitor with two in series electric double layer capacitors (EDLC)[31-34] as shown in Figure 2.7a,b. Figure 2.7a shows only the unbalanced local net charge within the SWNT thin film electrodes and in the bulk IL inter-electrode space. Two EDLCs are formed at the 3D boundary of the IL-SWNT interface. Under no applied potential, the ionic liquid fills this interface with a net neutral charge. As a potential is applied across the cell, the ionic liquid polarization is initiated through ion diffusion controlled be the local electric field at the SWNT-IL interface. The Helmholtz layer,[35] which is the IL-SWNT interface, is where most of the potential drop occurs as presented in Figure 2.7c. In the case of one SWNT electrode being thinner than the other, the corresponding electric double layer capacitances of the two electrodes will be uneven as shown in Figure 2.7b. In this simplified representation, the electrochromic cell is modeled as two connected in series capacitors and thus the voltage drop at each capacitor is inversely proportional to their capacitance. This leads to a large potential drop at the thinner electrode as it has a lower capacitance and a smaller potential drop at the thicker, higher capacitance electrode as presented in Figure 2.7c.

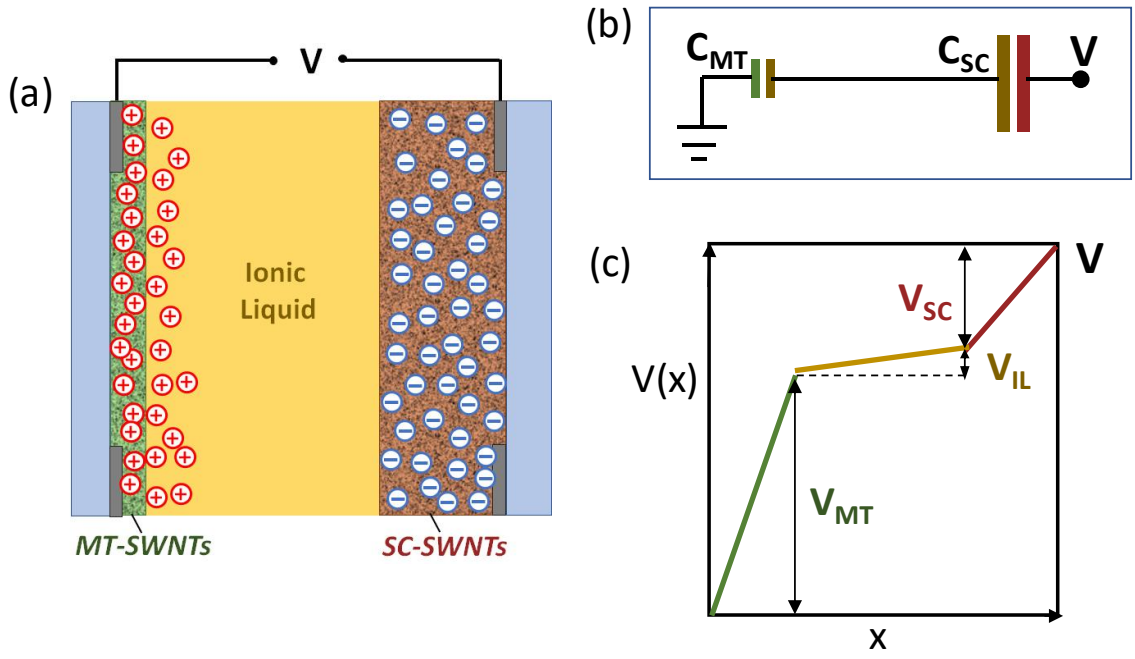

Figure 2.7: (a) Schematic of an unbalanced SWNT cell with only unbalanced local net charges shown. (b) Simplified equivalent circuit of cell and (c) the expected potential drop.

The interfaces between ILs and both nonporous and porous electrodes have been rigorously studied and share some similarities to classical pictures of organic electrolyte-solid electrode interface polarization processes.[36-38] Under no applied potential, the SWNT 3D nanoporous thin film and ionic liquid can be considered as two interpenetrating heterogeneous media,[39] with all pores filled with an equal number of cations and anions. When a potential is applied, the local electric field drives an exchange of ions of opposite sign between individual pores within the SWNT film and the bulk of the ionic liquid. This 3D interface contains a large volume of intra-bundle and inter-bundle space which allows for a large surface area of contact between the SC-SWNTs and IL. In this interface, a

crowding mechanism of the ionic liquid occurs in which the electrode is covered by a layer of ionic liquid of the opposite charge.[40-42] Thus, a thicker SWNT layer with a higher surface area can accommodate a higher concentration of net charge in the IL-SWNT interface than that of a thinner SWNT layer. However, ion polarization requires the same total charge of opposite signs being accumulated at opposite electrodes. In the case of an unbalanced cell, the thinner SWNT electrode will have a portion of its net charge distributed in the diffuse layer in the IL bulk as opposed to the IL-SWNT interface and this would require a larger spread of the electric field and a larger potential drop as discussed above. Thus, the thicker film would contain a smaller portion of the potential drop which results in a smaller electric field polarizing the IL and a resultant slower response.

To experimentally test the above model, electrochemical cells with additional potential probes inserted near each electrode were constructed. These probes allow monitoring of the potential drops in the vicinity of each electrode and in the inter-electrode ionic liquid space in a dynamic mode as the device is switched between the bleached and colored states. Figure 2.8a,c show schematics of such devices with either a thicker SC-SWNT (Figure 2.8a) or MT-SWNT (Figure 2.8c) electrode. Figure 2.8b shows the potential drops across the various electrodes in the case of a thinner MT-SWNT electrode. Here it can be clearly seen that the thinner MT-SWNT electrode experiences a significantly higher potential drop than the thicker SC-SWNT electrode with little potential drop occurring in the IL bulk in the inter-electrode space. In this case the device

was very sluggish as can be seen in the lower panel of Figure 2.8b with switching times of over 50 ms. Meanwhile, Figure 2.8d shows the potential drops in the case of a thicker MT-SWNT and thinner SC-SWNT electrode. Here the larger potential drop occurs on the electrochromic SC-SWNT electrode which results in a faster device with a response time of a few milliseconds as shown in the lower panel of Figure 2.8d.

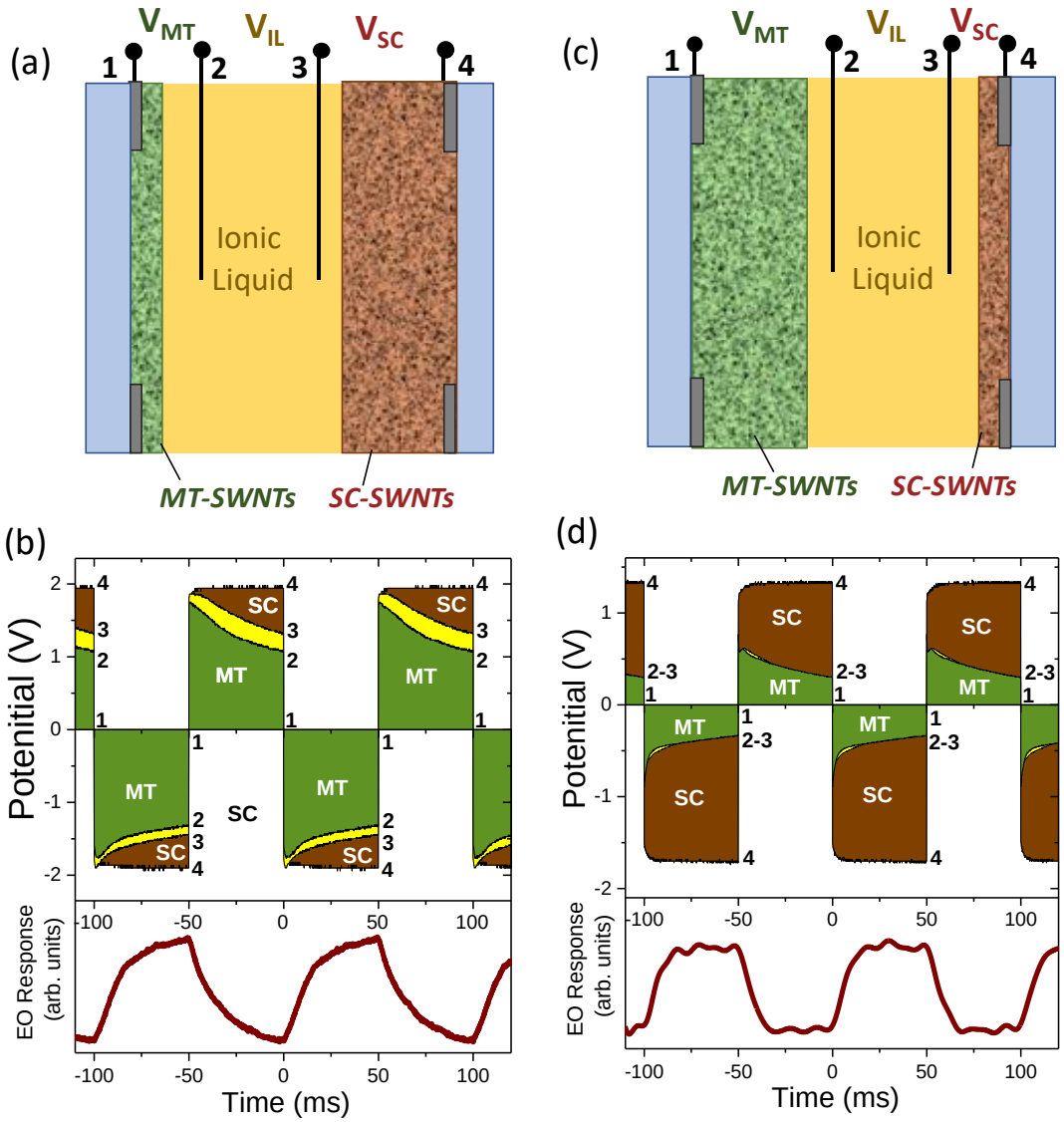

Figure 2.8: Schematics of devices containing additional potential probes with a thicker (a,b) SC-SWNT and (c,d) MT-SWNT electrode and the resultant potential drops and oscilloscope traces.

The above helps to explain the slow electrochromic response in the case of asymmetric devices whose SC-SWNT electrode is thicker than the MT-SWNT counter-electrode. In such a case, the potential drop at the SC-SWNT EDLC is a smaller portion of the overall potential across the cell which results in a smaller

electric field which is the driving force of the ion exchange in the SC-SWNT electrode. This slower ion diffusion then leads to a slower modulation of the charge states within the SC-SWNTs and thus a slower electro-optical response. In the opposite case where the SC-SWNT electrode is significantly thinner, the SC-SWNT will experience a larger portion of the applied potential resulting in a higher electric field thus driving faster ion diffusion resulting in faster electrochromic cell switching times. This is further evidenced by the optimal potential applied for various SC-SWNT:MT-SWNT thickness ratios as shown in Figure 2.9. The SC-SWNTs are being modulated from their intrinsic to the p-doped states (Figure 2.3) and the optimum potential to do so is dependent on the SC-SWNT:MT-SWNT thickness ratio. When the MT-SWNT is significantly thinner a larger potential is required as most of the potential drop occurs on the MT-SWNT and when the SC-SWNT is significantly thinner a smaller potential is required as most of the potential drop occurs on the SC-SWNT as previously discussed (Figure 2.8).

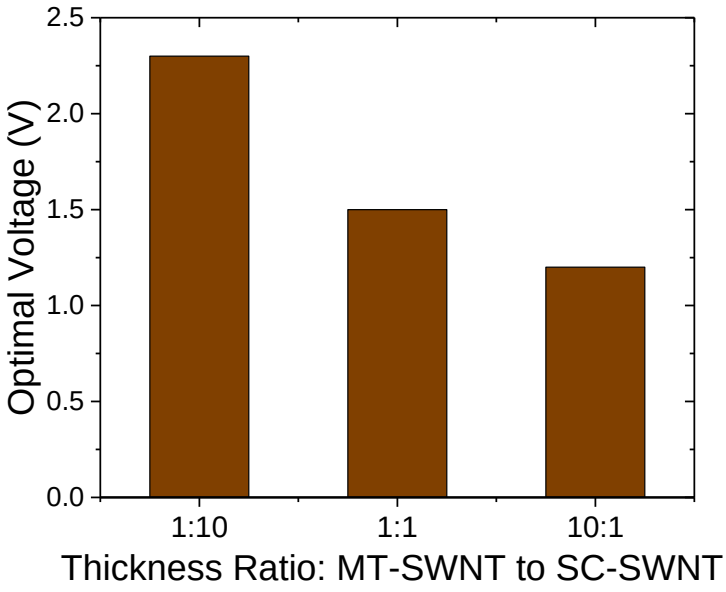

Figure 2.9: Optimal applied potential as a function of MT-SWNT:SC-SWNT electrode thickness.

The above discussion considers a simplified model in which the main factor of the cell is simply the thickness of each electrode. However, the picture is more complex as the types of electrodes used are different (MT- vs SC-SWNTs) and thus each should be studied individually. A complete description of the ac impedances of the electrochromic cells include a number of resistors and capacitors in series and in parallel to the two EDLCs corresponding to the resistances of the electrodes, inter-electrode spaces, and leakage resistances results in a very complex model.[43] Thus, we use a simplified model where the equivalent circuit of the electrochromic cell can be represented by two connected in series EDLCs as previously shown in Figure 2.7b. Here the voltage (*V*) and

time (*t*) dependent equivalent total capacitance (C_T) can be described by the following:

$$C_T(V,t) = \frac{(C_{SC}(U_{SC}(t))) \times (C_{MT}(U_{MT}(t)))}{(C_{SC}(U_{SC}(t))) + (C_{MT}(U_{MT}(t)))}$$

where C_{SC} and C_{MT} correspond to the capacitance of the SC-SWNT and MT-SWNT EDLCs respectively, which are controlled by the time-dependent potential drops $U_{SC}(t)$ and $U_{MT}(t)$ on the SC-SWNT and MT-SWNT EDLCs respectively. However, even for this simplified description, the electrochromic cell impedance becomes very complicated because of the voltage dependences of the quantum capacitances of the SC-SWNT and MT-SWNT layers controlled by time and polarity dependent distributions of the electrical potential across the electrochromic cell.

In the case of a very unbalanced cell, say $C_{SC} >> C_{MT}$, the imaginary portion of the cell impedance will be defined by the smaller of the two capacitances and the total measured capacitance of the cell (C_T) will be roughly equal to C_{SC}. So, to measure of the individual electrode, for example, C_{SC}, an unbalanced cell may be used. These measurements are in some sense equivalent to half-cell studies in batteries when the properties of one specific electrode, cathode or anode, need to be evaluated. In a recent report, the Pt counter-electrode shaped in the form of long multi-loop coils of Pt wire were utilized,[22] but such a coiled electrode is not compatible with the small (20 μL) volume of our compact electrochromic cell. Another alternative is a Pt film as a

flat counter-electrode, but our evaluation shows that the equivalent high capacitance counter-electrode, on the basis of a plain Pt film, would require unpractically large Pt electrode area 50 times larger than the area of our SC-SWNT film when taking into account the high surface area of the SWNT film. Instead, we utilized a high surface area thick MT-SWNT film as the best counter-electrode option to measure the specific capacitance of the SC-SWNT films.

Figure 2.10a presents the ac impedance measurements of the capacitance component in terms of specific capacitance of an unbalanced cell where the SC-SWNT electrode thickness is more than ten times the thickness of the MT-SWNT electrode. In ac impedance measurements the cell is swept from --3V to +2.5 V while applying an overlaid ac excitation (5mV) at various frequencies (1 to 100 Hz). The resulted $C_{SC}(V)$ dependences show a relatively flat region of the width of ~0.7 eV corresponding to the Fermi level position within the bandgap of SC-SWNTs surrounded by the regions of capacitance growth due to the increase of the quantum capacitance component as the Fermi level crosses the van Hove singularities associated with 1D density of states of SC-SWNTs as shown in Figure 2.2. To better visualize these regions, figure 2.10b presents the derivative $(dC_{SC}(V)/dV)$ which shows four characteristic maximums which most likely correspond to the 1st and 2nd pair of van Hove singularities in the valence band (VB), S_{1VB} and S_{2VB}, and conduction band (CB), S_{1CB} and S_{2CB}.[22] The relatively high specific capacitance of SWNT film is provided by its high geometrical capacitance associated with the high surface area of 3D SWNT

network and a unique additional contribution of quantum capacitance associated with quantum states of 1D SWNTs.[44] However it is lower than the value expected for the superionic regime when the ion size and the pore diameters are matching.[36,45] Low frequency values of capacitance and the overall shape of *C*(*V*) dependence is consistent with the data reported recently by the Iwasa group.[22] Because of the small (μL) volume of our cell we were not able to accommodate an optimal type of reference electrode, such as Ag/Ag+, typically utilized in electrochemical studies, so the energy positions in *C*(*V*) features may be shifted by a few tenths of a volt from the exact positions in the density of states of the SC-SWNTs.

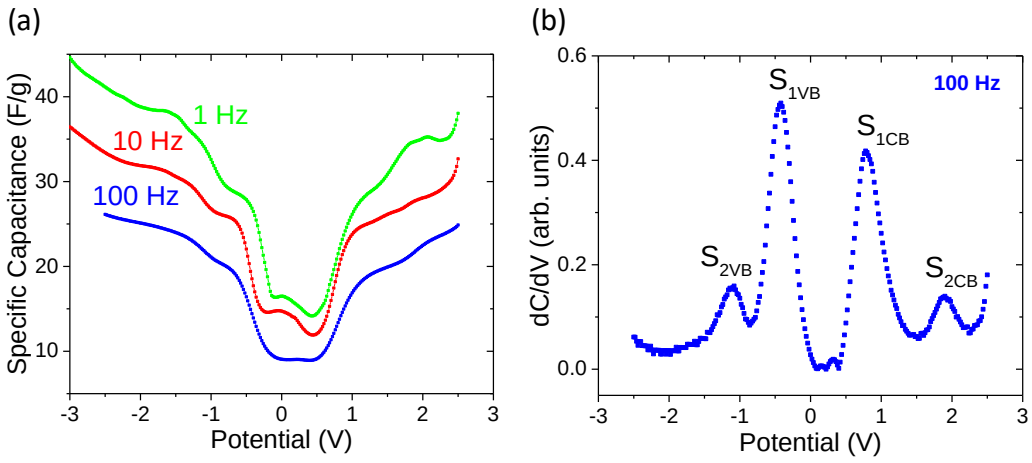

Figure 2.10: Specific capacitance of a SC-SWNT electrode as a function of voltage and (b) its voltage derivative obtained from ac impedance measurements at different excitation frequencies.

Similar measurements were done for the MT-SWNT electrodes in which the cell was made up of a thin MT-SWNT electrode and ten times thicker MT-SWNT counter electrode. A thick MT-SWNT electrode was chosen instead of a

thick SC-SWNT counter electrode in order to exclude S_{11} and S_{22} interfering features originating from the counter-electrode to the overall impedance. Figure 2.11 shows the resulted specific capacitance (Figure 2.11a) data along with the voltage derivative (Figure 2.11b). Both show features consistent with filling of the subbands corresponding to the pair of van Hove singularities in the valence and conduction band of MT-SWNTs.[22] Despite an expected energy independent finite density of states between the pair of 1st van Hove singularities we observed some increase of specific capacitance of MT-SWNTs with the shift of Fermi level from the midgap position.

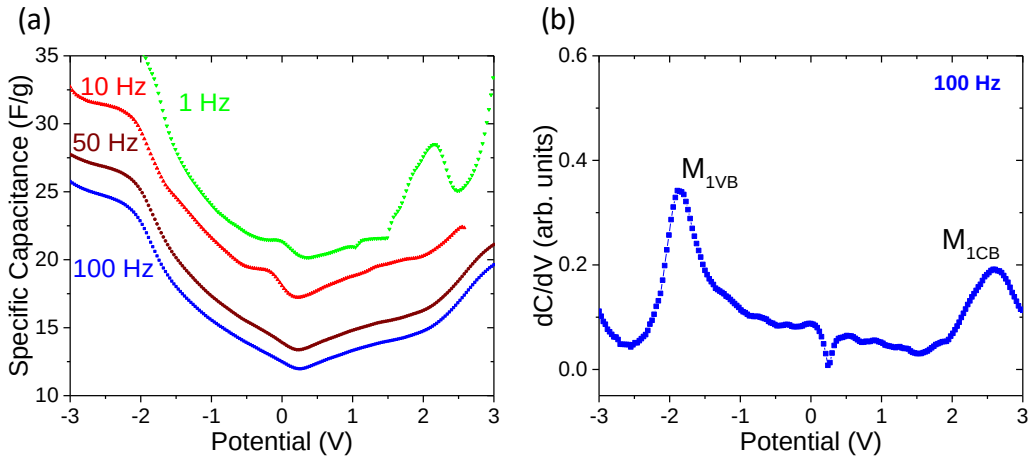

Figure 2.11: Specific capacitance of a MT-SWNT electrode as a function of voltage and (b) its voltage derivative obtained from ac impedance measurements at different excitation frequencies.

Both SC-SWNTs and MT-SWNTs are p-doped due to well-known SWNT environmental sensitivity[46] resulting in a shift of the midgap position towards positive voltage. The frequency dependences (ac modulation at different frequencies) of the midgap point specific capacitances for SC- and MT-SWNT

electrodes are presented in Figure 2.12. With decreasing frequency, the shapes of $C(V)$ dependence for both SC- and MT-SWNT electrodes presented in Figures 2.10a and 2.11a remain mostly unchanged, but the values of specific capacitance in both cases increase as ion exchange corresponding to less accessible sites within the 3D SWNT network became involved in the charge/discharge processes with increasing available time. The specific capacitance value of MT-SWNT film at low voltages, corresponding to the Fermi level position between the subbands associated with the 1st pair of van Hove singularities, is approximately 1.5-2 times higher than in case of SC-SWNTs due to a finite density of states in MT-SWNTs at the Fermi level. It correlates with the observation that approximately half of SC-SWNT electrode thickness is sufficient for the thickness of MT-SWNT counter-electrode in order to achieve the optimal impedance balance resulting in highest modulation bandwidth and shortest response time.

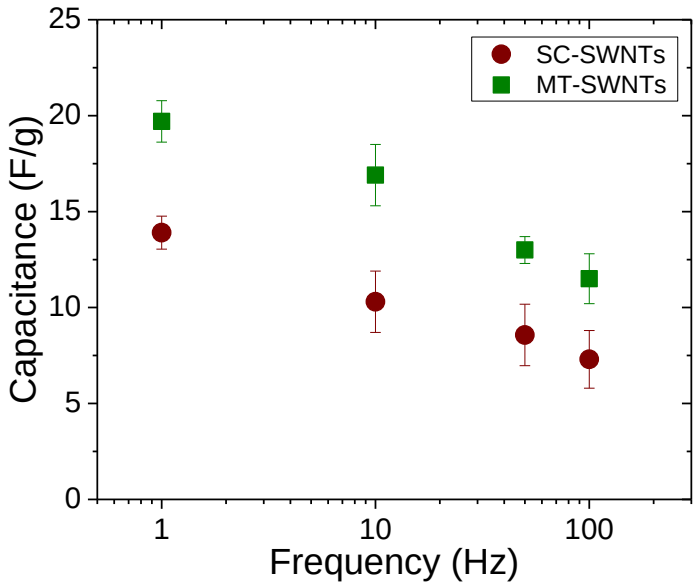

Figure 2.12: Capacitance as a function of frequency for SC- and MT-SWNT electrodes.

The balancing of the electrode and counter-electrode had been previously found to be important in electrochemical device design with an example being asymmetric supercapacitors.[43,47] While much research focuses on the design of the working electrode, the counter electrode has been paid significantly less attention. Recently however, there have been reports that demonstrated that the optimization of the counter-electrode can lower operating voltages, improve device stability, and decrease switching times in electrochromic cells which our results support.[29,30]

2.6: Coloration Efficiency

As discussed above, the SWNT based electrochromic device displays high modulation accompanied by very fast response times. Another parameter by which electrochromic devices are judged is their coloration efficiency (*CE*) which is defined as the change in optical density (*ΔOD*) per change in charge (*⊿Q*) which can be calculated from the following:[48]

$$CE = \frac{\Delta OD}{\Delta Q} = \frac{\log(T_{BL}/T_{COL})}{\Delta Q}$$

Figure 2.13a shows the chronoamperometry while Figure 2.13b shows the corresponding change in transmittance to a 10 Hz square-wave voltage modulation for two balanced cells with SC-SWNT thicknesses of 110 and 220nm. From these datasets, the coloration efficiency is determined from the slope of the linear portion of the optical density vs charge density as presented in Figure 2.13c. The *CE* for both devices exceeds 1800 cm^2/C. Typically used metal oxides range in 50-100 cm^2/C with response times of seconds to tens of seconds[49-51] while some can reach as high 450 cm^2/C in state of the art aluminum doped zinc oxide nanocrystals with response times of 60-70 ms.[13] The typical *CE* values for organic polymer based electrochromic cells are in the range of a few hundred cm^2/C with response times from a few seconds to sub- second,[52-57] while the highest *CE* value of ~5400 cm^2/C was reported with a response time of 150 ms.[58] Faster response times, in the range of 6-30 ms,[11,12] were reported, but without estimation of *CE* or modulation depth. The observed high coloration efficiency of the SWNT-based electrochromic cell is largely due to the SC-SWNT bleaching

mechanism which does not involve reduction-oxidation processes in the electrochromic material, but only refilling of the subbands originated from van Hove singularities of 1D SC-SWNTs. By integrating the current density and normalizing it to the mass of SC-SWNTs per cm^2 (9 and 18 μg) an average charge density of 42.8 Coulombs/g is found which corresponds to 0.0054 e/carbon. These values correspond to the amount of charge required for the switching from the bleached to colored state and are in agreement with the values reported in the literature.[22]

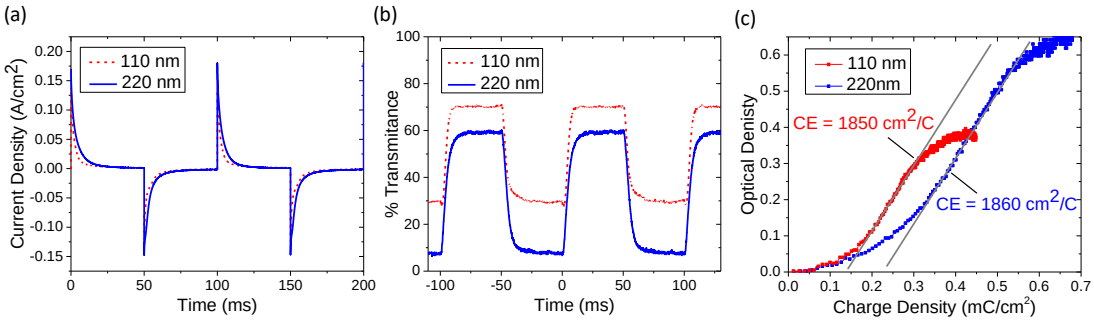

Figure 2.13: (a) Chronoamperometry, (b)transient transmittance spectra and (c) coloration efficiency of SC-SWNT electrochromic devices

2.7: Effects of Counter Electrode Type

Thus far we have ascribed the restoration of the electrochromic cell response time with the increasing capacitance of thick MT-SWNT counter-electrodes. However, it could also be argued that the restoration of the response time arises from the decreased sheet resistance from thickening the MT-SWNT as high sheet resistances have been shown to degrade the performance of devices such as supercapacitors and batteries.[43] To test the effects of sheet resistance versus capacitance two different counter electrodes were tested using

the same thickness of SC-SWNT electrodes. One counter electrode was made up of a single layer of graphene while the other was made up of a 120 nm thick MT-SWNT thin film. Both counter electrodes have similar sheet resistances (~ 700 Ω), but very different capacitances. Figure 2.14 shows the corresponding frequency dependencies of the electrochromic response for both device as well as the oscilloscope traces of the transmittance modulation. It can be seen that the MT-SWNT counter electrode device shows about a tenfold higher increase in bandwidth and more square-like oscilloscope traces. This indicates that the high surface area of the MT-SWNTs counter-electrode layer and resulting high electrochemical capacitance are responsible for the fast response times of the devices as opposed to its sheet resistance. The sheet resistance may be more important for significantly thinner films, especially near the percolation threshold.

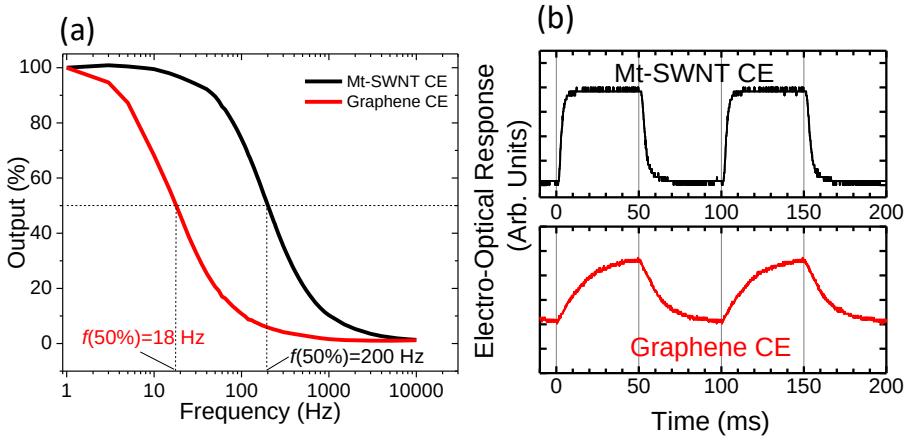

Figure 2.14: (a) Frequency dependencies and (b) oscilloscope traces of devices made with MT-SWNT and graphene counter electrodes with matching sheet resistances.

2.8: Effects of Offset Counter Electrodes:

As thus far demonstrated, matching the capacitance of the two electrodes by increasing the thickness of the MT-SWNT counter electrode is an important factor in the fast response times of the devices. However, while the MT-SWNTs are mostly transparent at the 1800 nm wavelength of discussion, they do cause some losses of transmittance. For example, with a 200 nm thick MT-SWNT there is approximately a 10% loss of transmittance in the bleached state (some of this has to do with a small amount (~1%) of SC-SWNTs in the MT-SWNT solution/film). To combat this loss in transmittance, a device in which the MT-SWNT counter electrode is offset from the electrochromic MT-SWNT electrode was designed as shown in Figure 2.15. Here the MT-SWNT counter-electrode covers only some area of the SC-SWNT film allowing for measurements of overlapped and nonoverlapped sections. As can be seen from the oscilloscope traces in Figure 2.15b, the overlapped sections display a more square-like shape while going further from the electrodes results in a more triangular type shape. Figure 2.15c shows the frequency dependencies which show a sharp drop off in bandwidth even in areas directly next to (but not overlapped) the MT-SWNT counter electrodes. Figure 2.15d shows that using thinner MT-SWNT electrodes does increase the transparency of the bleached state in case of no overlap, but is unfortunately accompanied by a tenfold decrease in bandwidth. This slowdown is likely associated with the weakening of the electric field as the separation of the electrodes is increased. This effect likely explains the slower response times of

the previously discussed notch filters with two electrodes placed on the same substrate.[28] Thus, a vertical design configuration with overlapping matched electrodes is optimal.

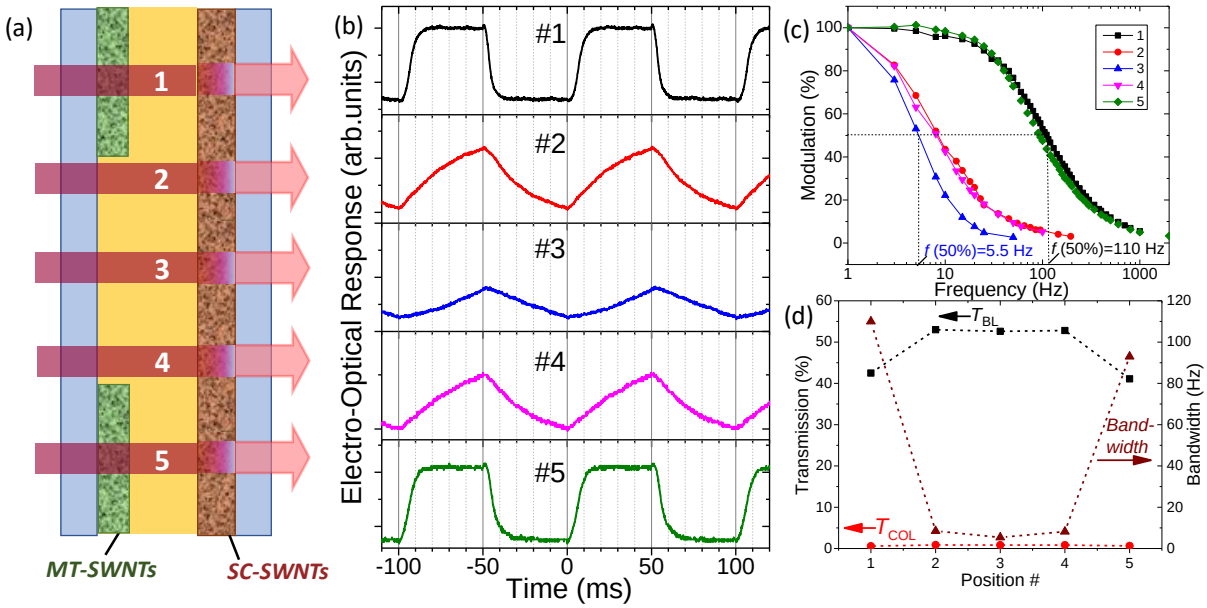

Figure 2.15: (a) Schematic of offset device with (b) resultant oscilloscope traces. (c) Frequency dependencies as a function of position and its (d) transmittance data.

2.9: Expansion to MWIR and LWIR

We have shown the ability of SC-SWNTs to modulate light at the S_{11} peak, however, close observation of low energy edge of the S_{11} (>2000 nm, Figure 2.3) provides a hint that the doping process could affect the transmittance at longer wavelengths.[59] The applications in the spectral range of mid-wave infrared (MWIR,3-8 um) and long-wave infrared (LWIR, 8-14 um) are plentiful. For example, MWIR is used in heat seeking missiles while the LWIR is used for thermal imaging.[60,61] Thus, the ability to modulate MWIR and LWIR radiation

could have numerous applications for military and civilian purposes. Unfortunately, the current device design is unsuitable for the MWIR and LWIR ranges. As previously discussed, an electrochromic device must have all transparent components other than the switchable electrochromic material. To remedy this, the glass substrates are substituted with transparent barium fluoride (BaF_2) substrates. The ionic liquid electrolytes also absorb in these ranges but, are a necessary component of the device. To help alleviate this, a number of ionic liquids were studied in thin layers (~0.01 mm) to minimize absorbance. $[C_6mim][PF_6]$ (1-hexyl-3-methylimidazolium hexafluorophosphate) was found to have the least amount of interfering features (Figure 2.16a). To study the effects on the SC-SWNTs without interference from the MT-SWNTs a horizontal device structure was used (Figure 2.16b) with the ionic liquid and encapsulating substrate not shown. Figure 2.16c shows the transmittance spectra from 1 to 14 μm which encapsulates the short-wave infrared (SWIR, 0.7-3 um) all the way to the LWIR. Here the absorbance of the device and ionic liquid are baselined out and thus the spectra show only the effects of the electrochromic SC-SWNT thin film. The device shows a MWIR modulation from ~85% to ~30% and a LWIR modulation of ~80% to ~15%. While further studies have yet to be carried out due to material and time constraints, the initial results are positive. Future work could look at the elimination of the absorbing electrolyte for a more transmissive, possibly solid-state electrolyte.

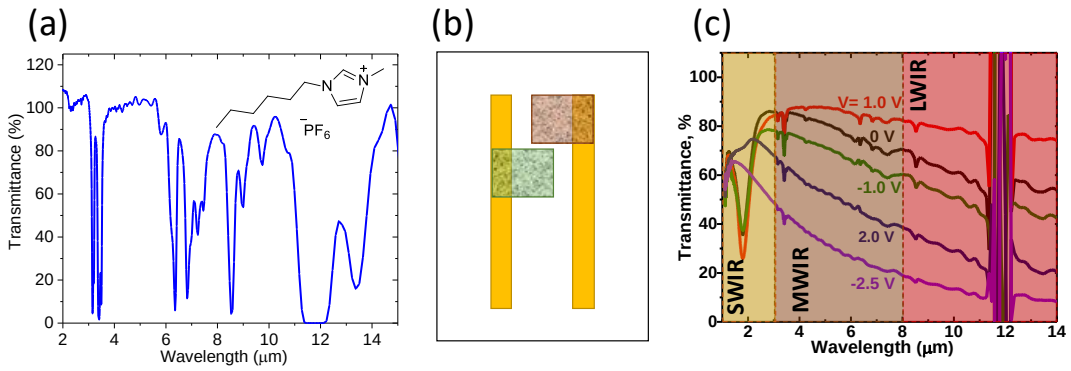

Figure 2.16: (a) Transmittance spectra of $[C_6mim][PF_6]$ in the SWIR to LWIR range. (b) Device schematic with a BaF_2 substrate, gold electrodes and SC-SWNT (brown) and MT-SWNT (green) thin films, the IL and encapsulation layer is not shown. (c) Transmittance spectra of the SC-SWNT thin film as a function of applied voltage in the SWIR to LWIR range.

2.10: Conclusions

In conclusion, we have developed electrochromic devices with SC-SWNT films as active electrochromic layers and MT-SWNT counter electrodes which serve as both transparent conducting electrodes and ion storage layers. Through balancing the of capacitances of the SC- and MT-SWNT electrodes we have achieved a modulation depth of 20 dB with switching times of a few milliseconds and a high coloration efficiency of 1800 cm^2/C. The device mechanisms were explored through consideration as an electric double layer capacitor. The resulting balanced and vertically designed device allows for effective potential distribution across the electrochromic cell maximizing the ion diffusion from the SC-SWNT electrode as it switches from a bleached to colored state. This work highlights the often-ignored importance of device design in electrochromic cells. The MWIR and LWIR applications of SC-SWNTs were also explored.

2.11: Experimental and Supplementary Information

Figure 2.17 shows the configuration of the typical device design while Figure 2.18 shows the configuration of the offset device related to sub-chapter 1.7 (Figure 2.15).

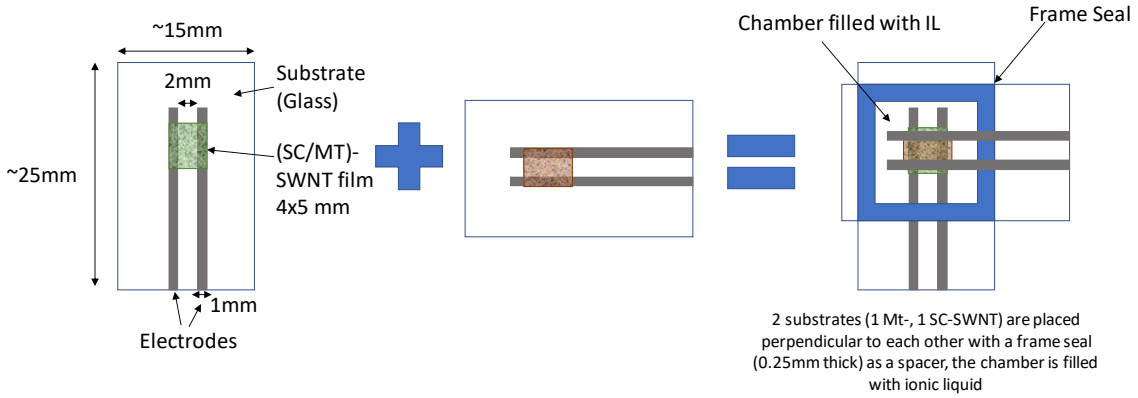

Figure 2.17: Typical device configuration.

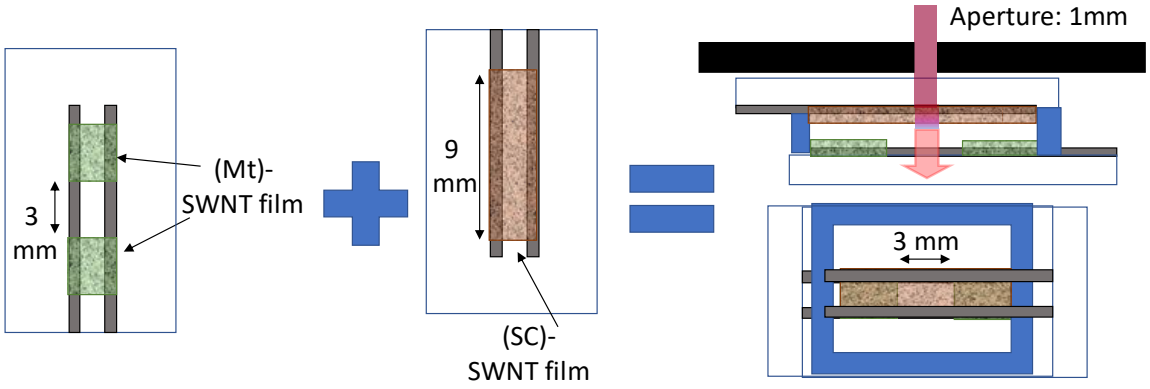

Figure 2.18: Offset device configuration.

Preparation of the electrochromic cell: Electrochromic and counter-electrode layers of the SWNT-based electrochromic cells were made in the form of semitransparent films of large diameter (diameters range 1.2-1.7 nm) 99% separated SC-SWNTs (IsoNanotubes-S) and MT-SWNTs (IsoNanotube-M), respectively, purchased from Nanointegris Inc. According to the manufacturer,

purification and separation of SWNTs was conducted by density gradient ultracentrifugation technique starting with electric arc discharge synthesized SWNT material. The SWNT films were prepared by vacuum filtration of the original dispersions of SC- and MT-SWNTs (spectra in Figure 2.19) and transferred on glass substrates to bridge 2 mm gap between predeposited Ti(15 nm)/Pt(150 nm) electrodes. The thickness of the SC- and MT-SWNT films was measured by Veeco Dektak 8 Profilometer. Taking into account the amount of SWNT material per unit area of the filtration membrane utilized for the film preparation the effective SWNT film density of 0.5±0.1 g/cm^3 was obtained. The effective thickness of the thinner films (outside of the Dektak measurement range) was obtained by comparing their optical absorption at wavelength of 27500 cm^{-1} (364 nm, featureless part of the spectra) to the absorption of the thick films at which Dektak thickness measurements were conducted as the optical absorption is proportional to the amount of SWNT material per unit area of the film. The glass substrates with two SWNT-based electrodes were sealed together by an adhesive frame (Frame-SealTM, Bio-Rad Laboratories) of thickness 250 μm with inner space filled with ionic liquid N,N-diethyl-N-(2-methoxyethyl)-N-methylammonium bis- (trifluoromethylsulfonyl)-imide (DEME-TFSI) purchased from IoLiTec Inc.

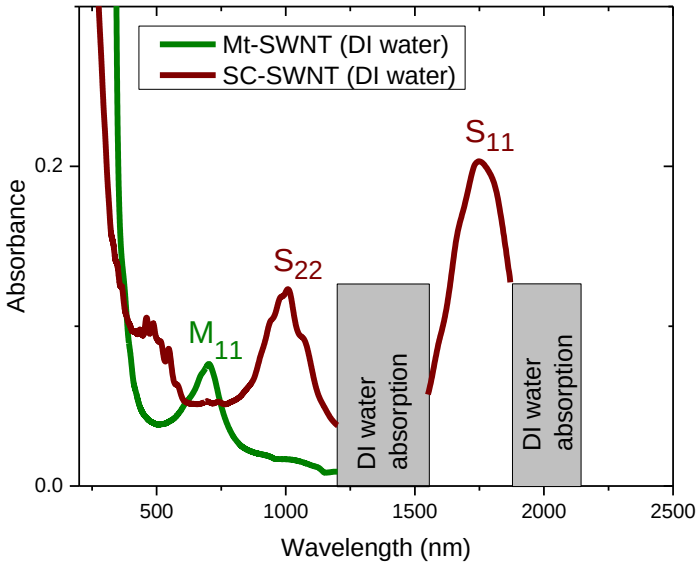

Figure 2.19: Absorption Spectra of SC- and MT-SWNT aqueous solutions used.

Spectroscopy and Electro-Optical Measurements: Transmission/Absorption spectra of the SWNT thin film based electrochromic cells were measured as a function of the voltage across the cell utilizing Cary 5000 UV-Vis-NIR spectrophotometer (Agilent Technologies) with the DC gate voltage supplied by Keithley model 617 source-meter. Dynamic properties of the electrochromic response were studied utilizing infrared LED (Model 1800P, Thorlabs) as a source of infrared radiation in the vicinity of wavelength 1800 nm closely matching the maximum of the S_{11} absorption band of SC-SWNTs. A square-wave voltage modulation was applied to the electrochromic cell utilizing an ultra-low distortion function generator (Model DS360, Stanford Research Systems). InGaAs photodiode (Model FD10D, Thorlabs) was utilized as a detector of the

electromodulated transmitted light with the output connected to the lock-in amplifier (SRS 830, Stanford Research Systems) to measure the amplitude and frequency dependence of the electrochromic response. The temporal traces of the electrochromic response were captured by Tektronix TDS 1001C-EDU oscilloscope connected to the ac output of the lock-in amplifier. The dynamic potential distribution across the SWNT electrochromic cell presented in Figure 2.8e,g was measured by an oscilloscope (Tektronix TDS 1001C-EDU) with different inputs of the oscilloscope measuring potentials at the probes 2, 3, and 4 in reference to the electrically grounded MT-SWNT film (Probe 1). Figure 2.20 shows the transmittance and absorbance spectra of various SC-SWNT films used.

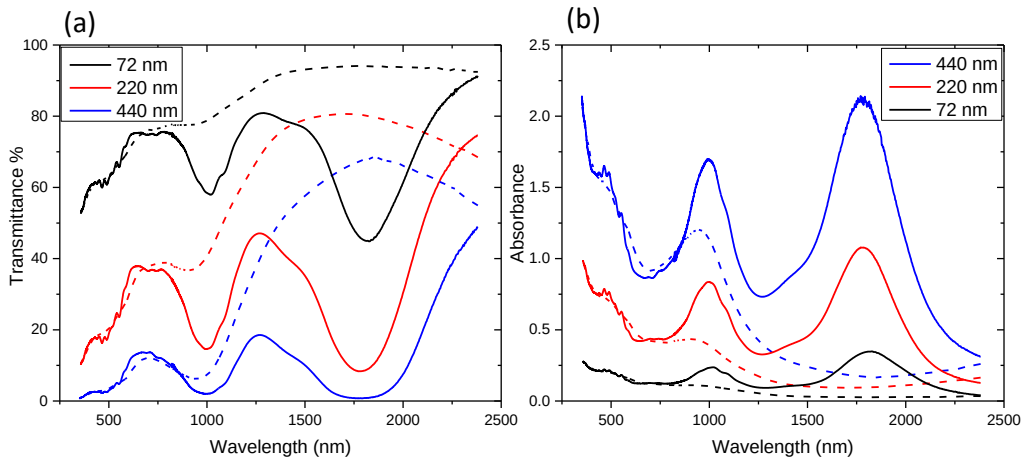

Figure 2.20: (a) Transmittance and (b) absorbance spectra of various SC-SWNT films used.

Electrochemical Measurements: Chronoamperometry, cyclic voltammetry and Electrochemical Impedance Spectroscopy measurements were performed on a CHI 1140 electrochemical analyzer (CH Instruments Inc) in a 2-electrode

configuration. For chronoamperometry applied potentials of +1.9V and -1.3V for the 55nm SC-SWNT device and +1.8V and -1.4V for the 110 nm SC-SWNT device were used. AC impedance measurements were performed on a CHI 6203D electrochemical workstation (CH Instruments Inc) with 0.03 V increments, 0.005 V amplitude and varying AC frequencies. Figure 2.21 shows the EIS spectroscopy of a balanced device.

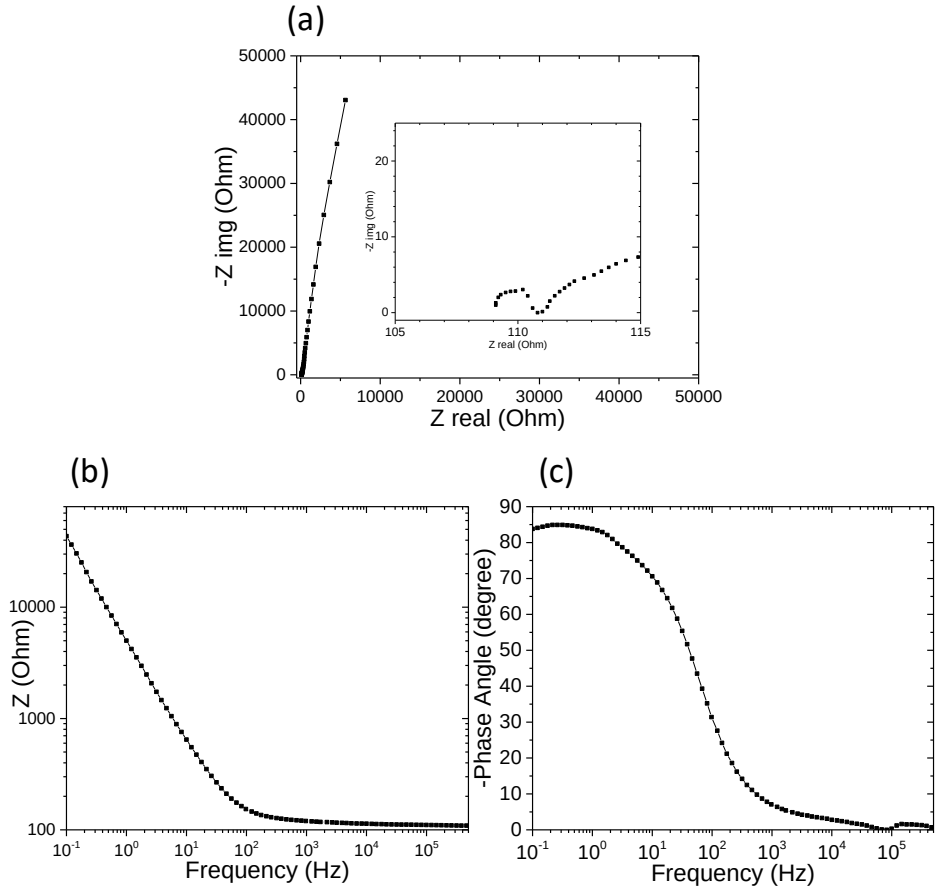

Figure 2.21: Electrochemical impedance spectroscopy of a 120 nm SC-SWNT/120 nm Mt-SWNT electrochromic device. (a) Nyquist plot showing linearity in the low frequency and the characteristic (inset) semi-circle at high frequencies. (b) Bode magnitude plot. (c) Bode angle plot reaching ~85° at low frequencies.

2.12: References

1) Wang, Y.; Runnerstrom, E. L.; Milliron, D. J. *Annu. Rev. Chem. Biomol. Eng.* **2016**, *7*, 283.

2) Granqvist, C. G. *Thin Solid Films* **2014**, *564*, 1.

3) Baetens, R.; Jelle, B. P.; Gustavsen, A. *Sol. Energy Mater Sol. Cells* **2010**, *94*, 87.

4) Phan, L.; Walkup, W. G.; Ordinario, D. D.; Karshalev, E.; Jocson, J. M.; Burke, A. M.; Gorodetsky, A. A. *Adv. Mater.* **2013**, *25*, 5621.

5) Morin, S. A.; Shepherd, R. F.; Kwok, S. W.; Stokes, A. A.; Nemiroski, A.; Whitesides, G. M. *Science* **2012**, *337*, 828.

6) Chou, H. H.; Nguyen, A.; Chortos, A.; To, J. W. F.; Lu, C.; Mei, J. G.; Kurosawa, T.; Bae, W. G.; Tok, J. B. H.; Bao, Z. A. *Nat. Commun.* **2015**, *6*.

7) Kim, G. W.; Kim, Y. C.; Ko, I. J.; Park, J. H.; Bae, H. W.; Lampande, R.; Kwon, J. H. *Adv. Opt. Mater.* **2018**, *0*, 1701382.

8) Bach, U.; Corr, D.; Lupo, D.; Pichot, F.; Ryan, M. *Adv. Mater.* **2002**, *14*, 845.

9) Deb, S. K. *Sol. Energy Mater Sol. Cells* **2008**, *92*, 245.

10) Mortimer, R. J.; Rosseinsky, D. R.; Monk, P. M. S., Eds *Electrochromic Materials and Devices*; Wiley-VCN Verlag GmbH & Co. KGaA: Weinheim, Germany, 2013.

11) Cho, S. I.; Kwon, W. J.; Choi, S.-J.; Kim, P.; Park, S.-A.; Kim, J.; Son, S. J.; Xiao, R.; Kim, S.-H.; Lee, S. B. *Adv. Mater.* **2005**, *17*, 171.

12) Jain, V.; Yochum, H. M.; Montazami, R.; Heflin, J. R. *Appl. Phys. Lett.* **2008**, *92*, 033304.

13) Garcia, G.; Buonsanti, R.; Llordes, A.; Runnerstrom, E. L.; Bergerud, A.; Milliron, D. J. *Adv. Opt. Mater.* **2013**, *1*, 215.

14) Wu, Z.; Chen, Z.; Du, X.; Logan, J. M.; Sippel, J.; Nikolou, M.; Kamaras, K.; Reynolds, J. R.; Tanner, D. B.; Hebard, A. F.; Rinzler, A. G. *Science* **2004**, *305*, 1273.

15) Layani, M.; Kamyshny, A.; Magdassi, S. *Nanoscale* **2014**, *6*, 5581.

16) Yanagi, K.; Moriya, R.; Yomogida, Y.; Takenobu, T.; Naitoh, Y.; Ishida, T.; Kataura, H.; Matsuda, K.; Maniwa, Y. *Adv. Mater.* **2011**, *23*, 2811.

17) Takenobu, T.; Murayama, Y.; Iwasa, Y. *Appl. Phys. Lett.* **2006**, *89*, 263510.

18) Takenobu, T.; Murayama, Y.; Shiraishi, M.; Iwasa, Y. *Jpn. J. Appl. Phys.* **2006**, *45*, L1190.

19) Wang, F.; Itkis, M. E.; Haddon, R. C. *Nano Lett.* **2010**, *10*, 937.

20) Wang, F.; Itkis, M. E.; Bekyarova, E.; Haddon, R. C. *Nat. Photonics* **2013**, *7*, 459.

21) Pekker, Á.; Kamarás, K. *Phys. Rev. B* **2011**, *87*, 075475(8).

22) Shimotani, H.; Tsuda, S.; Yuan, H.; Yomogida, Y.; Moriya, R.; Takenobu, T.; Yanagi, K.; Iwasa, Y. *Adv. Funct. Mater.* **2014**, *24*, 3305.

23) De Volder, M. F. L.; Tawfick, S. H.; Baughman, R. H.; Hart, A. J. *Science* **2013**, *339*, 535.

24) Moser, M. L.; Li, G.; Chen, M.; Bekyarova, E.; Itkis, M. E.; Haddon, R. C. *Nano Lett.* **2016**, *19*, 5386.

25) Agrawal, G. P. *Fiber-Optic Communication System*; 4th ed.; John Wiley & Sons: Rochester, 2010; Vol. 222.

26) Chernysheva, M.; Mou, C. B.; Arif, R.; AlAraimi, M.; Rummeli, M.; Turitsyn, S.; Rozhin, A. *Sci. Rep.* **2016**, *6*.

27) Reed, G. T.; Mashanovich, G.; Gardes, F. Y.; Thomson, D. J. *Nat. Photon.* **2010**, *4*, 518.

28) Berger, F. J.; Higgins, T. M.; Rother, M.; Graf, A.; Zakharko, Y.; Allard, S.; Matthiesen, M.; Gotthardt, J. M.; Schee, U.; Zaumseil, J. *ACS App. Mater. Interfaces* **2018**, *10*, 11135.

29) Shen, D. E.; Osterholm, A. M.; Reynolds, J. R. *J. Mater. Chem. C* **2015**, *3*, 9715.

30) Kim, Y.; Shin, H.; Han, M.; Seo, S.; Lee, W.; Na, J.; Park, C.; Kim, E. *Adv. Funct. Mater.* **2017**, *27*.

31) Bisri, S. Z.; Shimizu, S.; Nakano, M.; Iwasa, Y. *Adv. Mater.* **2017**, *29*, 1607054.

32) Ueno, K.; Shimotani, H.; Yuan, H.; Ye, J.; Kawasaki, M.; Iwasa, Y. *J. Phys. Soc. Jpn.* **2014**, *83*, 032001.

33) Ueno, K.; Nakamura, S.; Shimotani, H.; Ohtomo, A.; Kimura, N.; Nojima, T.; Aoki, H.; Iwasa, Y.; Kawasaki, M. *Nat. Mat.* **2008**, *7*, 855.

34) Ueno, K.; Nakamura, S.; Shimotani, H.; Yuan, H. T.; Kimura, N.; Nojima, T.; Aoki, H.; Iwasa, Y.; Kawasaki, M. *Nature Nanotech.* **2011**, *6*, 408.

35) Bockris, J. O. M.; Reddy, A. K. N.; Gamboa-Aldeco, M. *Modern Electrochemistry 2A. Fundamentals of Electrodics*; 2nd ed.; Plenum Publishing Corporation: New York, 1998; Vol. 1.

36) Kornyshev, A. A. *J. Phys. Chem. B* **2007**, *111*, 5545.

37) Mezger, M.; Schroder, H.; Reichert, H.; Schramm, S.; Okasinski, J. S.; Schoder, S.; Honkimaki, V.; Deutsch, M.; Ocko, B. M.; Ralston, J.; Rohwerder, M.; Stratmann, M.; Dosch, H. *Science* **2008**, *322*, 424.

38) Salanne, M. *Top. Curr. Chem.* **2017**, *375*.

39) Merlet, C.; Rotenberg, B.; Madden, P. A.; Taberna, P. L.; Simon, P.; Gogotsi, Y.; Salanne, M. *Nat. Mater.* **2012**, *11*, 306.

40) Largeot, C.; Portet, C.; Chmiola, J.; Taberna, P. L.; Gogotsi, Y.; Simon, P. *J. Am. Chem. Soc.* **2008**, *130*, 2730.

41) Shim, Y.; Kim, H. J. *ACS Nano* **2010**, *4*, 2345.

42) Bazant, M. Z.; Storey, B. D.; Kornyshev, A. A. *Phys. Rev. Lett.* **2011**, *106*.

43) Miller, J. M. *Ultracapacitor Applications*; 1 ed.; The Institution of Engineering and Technology: London, 2011; Vol. 59.

44) Liang, J.; Akinwande, D.; Wong, H. S. P. *J. Appl. Phys.* **2008**, *104*.

45) Kondrat, S.; Kornyshev, A. *J. Phys. Condens. Matter* **2011**, *23*.

46) Collins, P. G.; Bradley, K.; Ishigami, M.; Zettl, A. *Science* **2000**, *287*, 1801.

47) Cai, X. Y.; Lim, S. H.; Poh, C. K.; Lai, L. F.; Lin, J. Y.; Shen, Z. X. *J. Power Sources* **2015**, *275*, 298.

48) Cai, G. F.; Darmawan, P.; Cui, M. Q.; Wang, J. X.; Chen, J. W.; Magdassi, S.; Lee, P. S. *Adv. Energy Mater.* **2016**, *6*.

49) Gu, H. X.; Guo, C. S.; Zhang, S. H.; Bi, L. H.; Li, T. C.; Sun, T. D.; Liu, S. Q. *ACS Nano* **2018**, *12*, 559.

50) Luo, G.; Shen, L. Y.; Zheng, J. M.; Xu, C. Y. *J. Mater. Chem. C* **2017**, *5*.

51) Gillaspie, D. T.; Tenent, R. C.; Dillon, A. C. *J. Mater. Chem.* **2010**, *20*, 9585.

52) Gaupp, C. L.; Welsh, D. M.; Rauh, R. D.; Reynolds, J. R. *Chem. Mater.* **2002**, *14*, 3964.

53) Chen, X. H.; Qiao, W. Q.; Wang, Z. Y. *RSC Adv.* **2017**, *7*, 15521.

54) Sapp, S. A.; Sotzing, G. A.; Reynolds, J. R. *Chem. Mater.* **1998**, *10*, 2101.

55) Cummins, D.; Boschloo, G.; Ryan, M.; Corr, D.; Rao, S. N.; Fitzmaurice, D. *J. Phys. Chem. B* **2000**, *104*, 11449.

56) Argun, A. A.; Aubert, P. H.; Thompson, B. C.; Schwendeman, I.; Gaupp, C. L.; Hwang, J.; Pinto, N. J.; Tanner, D. B.; MacDiarmid, A. G.; Reynolds, J. R. *Chem. Mater.* **2004**, *16*, 4401.

57) Shin, H.; Seo, S.; Park, C.; Na, J.; Han, M.; Kim, E. *Energy Environ. Sci.* **2016**, *9*, 117.

58) Cirpan, A.; Argun, A. A.; Grenier, C. R. G.; Reeves, B. D.; Reynolds, J. R. *J. Mater. Chem.* **2003**, *13*, 2422.

59) Itkis, M. E.; Borondics, F.; Yu, A.; Haddon, R. C. *Science* **2006**, *312*, 413.

60) Henini, M.; Razeghi, M. *Handbook of Infrared Detection Technologies*; Elsevier Advanced Technology: Kidlington, Oxford, UK, 2002.

61) Rogalski, A. *Infrared Detectors*; 2 ed.; CRS Press: Boca Raton, Fl, USA, 2011.

Chapter 3: Effects of Substitutional Doping on the Conductivity of a Phenalenyl Based Neutral Radical Conductor

3.1: Introduction

As discussed in chapter 1, neutral radical conductors have some of the highest conductivities for intrinsic organic conductors. Amongst phenalenyl based neutral radical conductors, those displaying the RVB motif have the highest conductivities.[1-3] One of these is the spiro-bis(5-methyl-1,9-oxido-phenalenyl)boron radical ([5-Me]$_2$B). Figure 1.1 shows the structure of [5-Me]$_2$B along with its temperature dependent spin per molecule magnetic properties, which are commonly found in neutral radical conductors with resonating valence bond (RVB) motifs. [5-Me]$_2$B displays one of the highest conductivities for phenalenyl based neutral radical conductors at 0.3 S/cm at 300 K.[3]

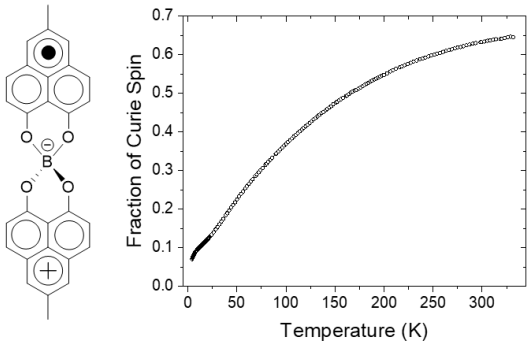

Figure 3.1: The structure and magnetic properties of [5-Me]$_2$B.

As previously discussed, while the band structure of the compound may predict metallic behavior, the on-site coulombic correlation energy (which can be estimated from the CV, Figure 3.8a) creates a band gap which results in the

semiconducting behavior. One solution to this would be a lattice of phenalenyl based molecules in which alternating molecules would either possess a radical or not possess one, thus enabling electrical conductivity without the electron-electron repulsions. Also discussed in chapter 1, the doping was used of to increase the conductivities of semiconductors. While interstitial doping has proven to be a successful way of increasing conductivity, substitutional doping analogous to n- and p-type silicon is significantly less explored.[4-7] The Haddon research group had previously successfully shown the 1st example of the substitutional doping with a phenalenyl based neutral radical conductor, the concentration of dopant was limited.[8] Thus, the effects of substitutional doping in a RVB neutral organic radical conductor warranted further study, especially in the case of a lattice comprised of 50% dopant.

3.2: Introduction to Substitutional Doping in [5-Me]$_2$B

In the case of the substitutional doping of silicon, dopants are chosen from neighboring groups in the periodic table, and would either have one more or one less electron thus serving as n- or p-type dopants. In the case of our bis-boron compounds, boron may be replaced with beryllium which contains one less electron and thus should serve as a p-type dopant. Figure 3.2 shows the structure of the dopant [5-Me]$_2$Be and an overview of the doping co-crystallization. As can be seen, the host and dopant only differ in the bridging element, boron or beryllium, and thus their structures are predicted to be similar allowing for effective substitutional doping. Solutions of [5-Me]$_2$Be and the

precursor cation of $[5\text{-Me}]_2B$ are mixed together, the cation is reduced through the use of a chemical reductant (tetrakis(dimethylamino)ethylene (TDAE)), and solid solutions of various compositions are grown.

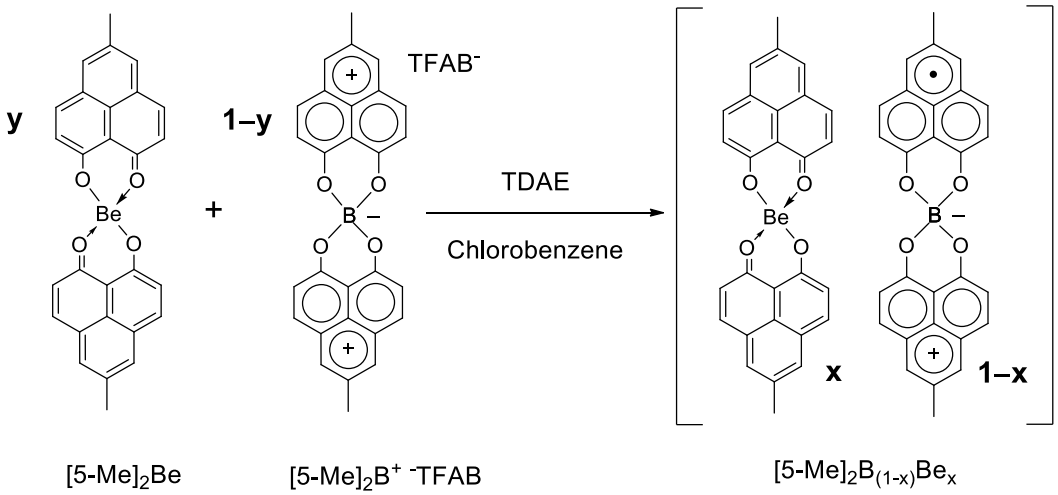

Figure 3.2: Drawings of $[5\text{-Me}]_2Be$ and an overview of the doping co-crystallization. (TFAB = tetrakis[3,5-bis(trifluoromethyl)phenyl]borate)

3.3: Host and Dopant Crystal Structures

In order to have effective substitutional doping, the dopant must incorporate itself into the structure of the host. To evaluate the fit of the dopant into the host structure the crystal structures were evaluated. Figure 3.3 shows the structure of $[5\text{-Me}]_2B$ and $[5\text{-Me}]_2Be$ molecules along with pictures of their crystals. $[5\text{-Me}]_2B$, like all other phenalenyl based neutral radical conductors, is black and opaque while $[5\text{-Me}]_2Be$ is an orange color, similar to the cationic precursor of $[5\text{-Me}]_2B$. The crystal structures of individual molecules of host and dopant look similar. Both compounds show a spiro-conjugated structure with an approximately 30° bend about the tetrahedral bridging atom. This bend is most

likely due to the presence of the methyl group which prevents complete overlap with neighboring molecules due to steric hindrance as discussed further below.

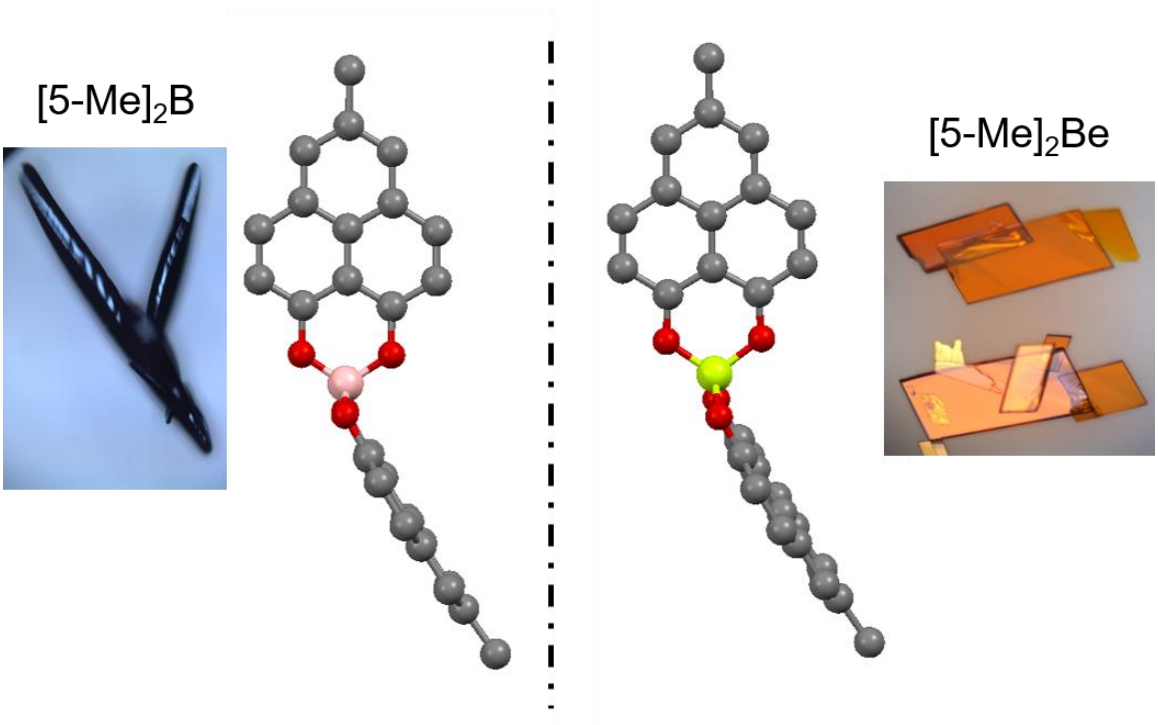

Figure 3.3: Pictures of crystals and molecule crystal structure of host (left) [5-Me]$_2$B and dopant (right) [5-Me]$_2$Be.

As discussed in chapter 1, the intermolecular interactions in crystals of neutral radicals often determine their properties. [5-Me]$_2$B packs in a triclinic unit cell (space group P-1, Z =2). The main feature of its crystal structure are 1-D chains of PLY-PLY overlaps as shown in Figure 3.4 and thus [5-Me]$_2$B is a quasi-1-D material. These 1-D chains are a common theme in phenalenyl based neutral radical conductors which demonstrate RVB packing motifs. The sister compound without the methyl at the 5 position demonstrates complete symmetry (1/2 molecule in asymmetric unit) and thus the 1-D chain is comprised of completely same PLY-PLY interactions. In [5-Me]$_2$B, steric hindrance of the

methyl with the bridging boron prevents this perfect symmetry. Instead the 1-D chains are comprised of 2 separate types PLY-PLY interactions as shown in Figure 3.4 and discussed in greater detail further below.

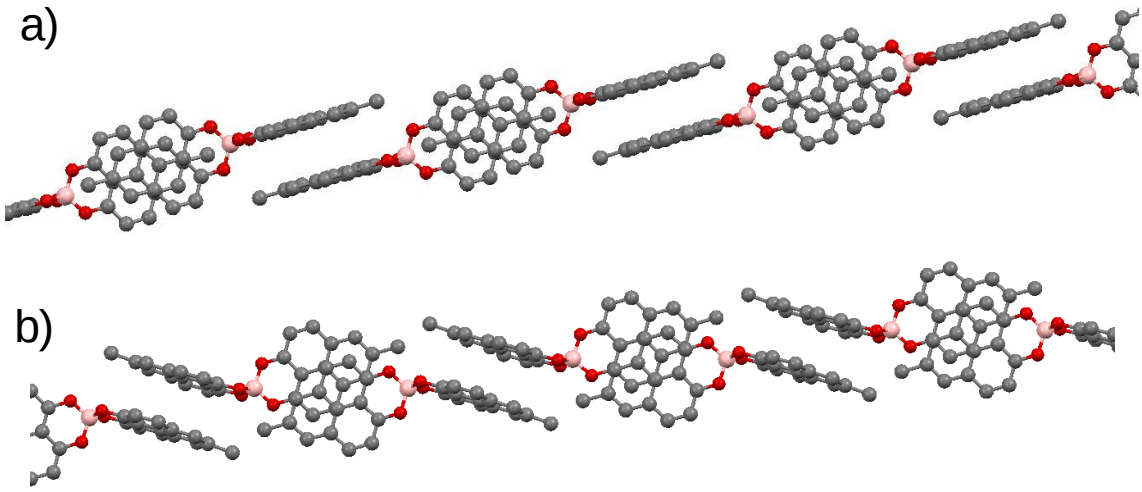

Figure 3.4: 1-D chains of $[5\text{-Me}]_2B$ in perpendicular views (a and b).

In stark contrast, $[5\text{-Me}]_2Be$ adopts a monoclinic unit cell (space group $P2_1/c$, Z = 4), and exhibits a dimeric packing arrangement as shown in Figure 3.5. While there are PLY-PLY intradimer interactions, there are no obvious interdimer interactions. This large difference in packing is ascribed to either the presence or the absence of the radical.

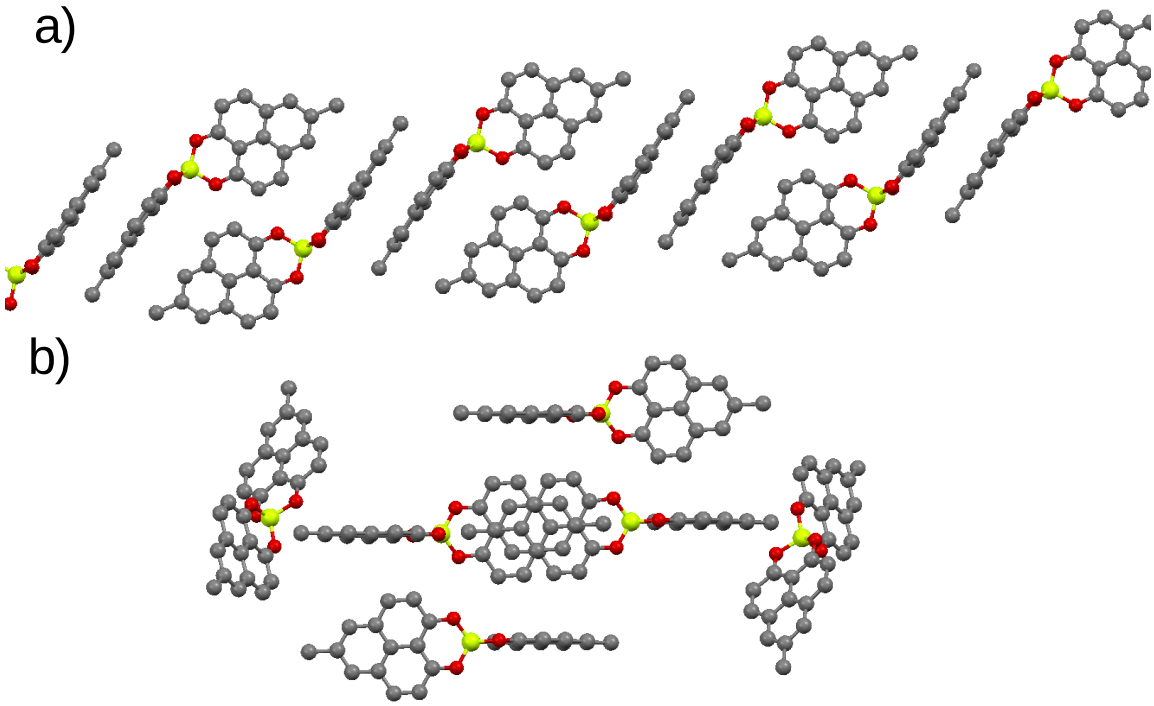

Figure 3.5: Dimeric structure of $[5\text{-Me}]_2$Be showing perpendicular views of dimers with no well overlapped neighbors.

As well as the overall packing structure (dimers vs 1-D chains), the PLY-PLY interactions found in $[5\text{-Me}]_2$B and $[5\text{-Me}]_2$Be are also quite different. As previously state $[5\text{-Me}]_2$B contains 2 separate types of PLY-PLY interactions within the 1-D chain. These interactions are pictured in Figure 3.6. Here the spin bearing carbons (carbons on which the electrons in the non-bonding molecular orbital reside) are colored blue and green for clarity. The first type of PLY-PLY interaction (Figure 3.6a) is similar to the non-methyl containing sister compound and demonstrates almost perfect overlap of spin bearing carbons. Additionally, this PLY-PLY overlap has a short mean plane distance of 3.24 Å, significantly shorter than that of the van der waals distance (3.4 Å). The other PLY-PLY

interaction, due to the presence of the methyl, adopts a slipped structure with only 2 overlapped spin bearing carbons (Figure 3.6b). Even though this interaction contains much less spin bearing carbon overlap, its interplanar distance (3.29 Å) is still significantly shorter than the van der waals distance of carbon.

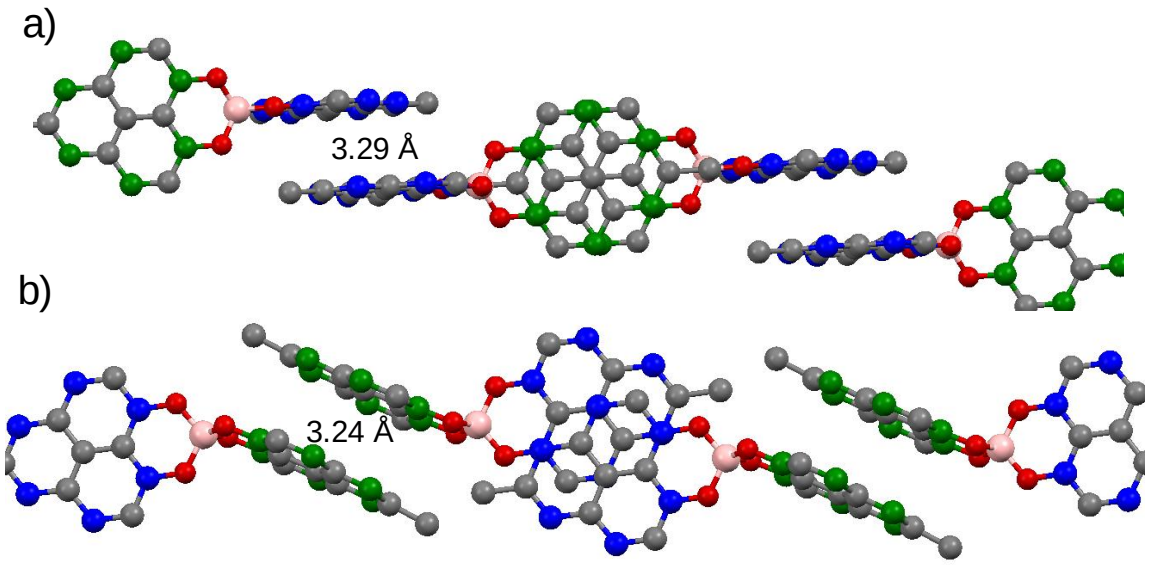

Figure 3.6: Perpendicular views of PLY-PLY interactions involving (a) six and (b) 2 spin bearing carbons.

Meanwhile the dopant, $[5\text{-Me}]_2\text{Be}$, only contains one type of PLY-PLY interaction due to its dimeric structure. This interaction is pictured in Figure 3.7. While there is significant PLY-PLY interaction, none of the 6 spin bearing carbons are overlapped. This lack of overlap is not surprising as the orbital is empty and thus would be predicted to have little to no effect. The interplanar distance (3.37 Å) here is similar to the van der waals distance. These packing

motifs are ascribed to van der Waals dispersion forces which are still sufficient to marinating pi-stacked structures even in the absences of a radical.[9-11]

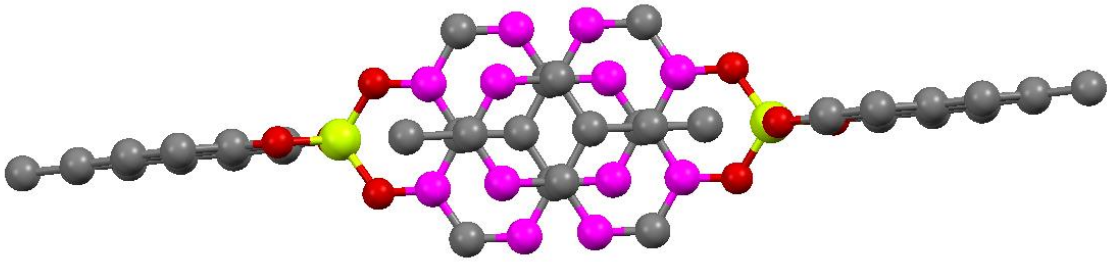

Figure 3.7: PLY-PLY interaction in $[5\text{-Me}]_2$Be.

In conclusion, while the host and dopant only differ in the bridging atom and the presence/absence of a radical, the compounds show significantly different crystal packing structures. $[5\text{-Me}]_2$B demonstrates 1-D chains of 2 different PLY-PLY interactions with short intermolecular distances while $[5\text{-Me}]_2$Be packs as dimers with 1 PLY-PLY interaction that shows poor spin bearing carbon overlap and a larger intermolecular distance.

3.4: Electrochemical Properties of Host and Dopant

Other than structure, another important factor is the electrochemical properties of the host and dopant. Figure 3.8 shows the cyclic voltammograms of $[5\text{-Me}]_2$B and $[5\text{-Me}]_2$Be. It can be seen that $[5\text{-Me}]_2$B can be reduced from cation to neutral radical at -0.36 V and to anion at -0.64 V resulting in a disproportionation constant of 0.28 V (an estimate of the on-site coulombic correlation energy). Meanwhile, the dopant ($[5\text{-Me}]_2$Be) can be reduced from neutral radical-lacking molecule to radical anion at -1.40 V and dianion at -1.69

V. Thus, the energy barrier for an electron to transfer from host to dopant can be estimated as 1.04 V which is significantly higher than the energy required for the disproportionation of 2 molecules of $[5\text{-Me}]_2B$. It should be noted that these are solution-based techniques and thus there are significant limitations to comparisons of the solid-state properties. Overall these results would suggest that $[5\text{-Me}]_2Be$ should be a poor dopant for $[5\text{-Me}]_2Be$.

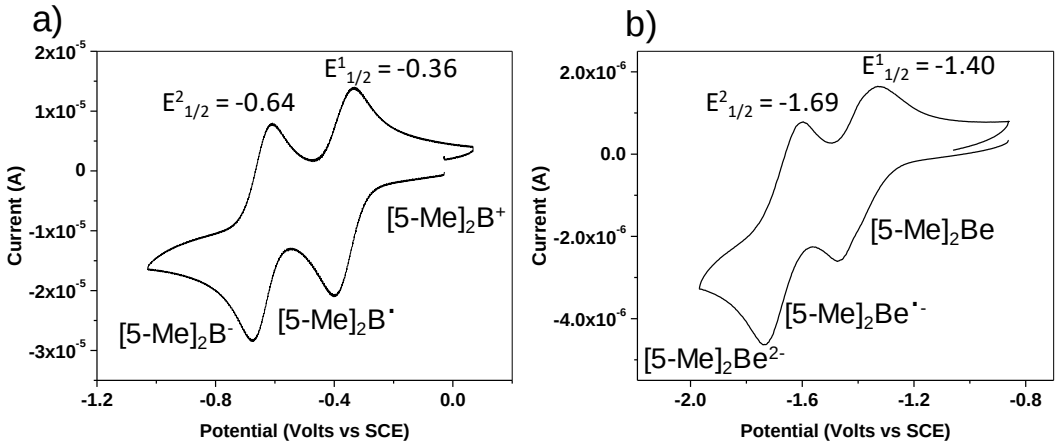

Figure 3.8: Cyclic voltammograms of (a) $[5\text{-Me}]_2B$ and (b) $[5\text{-Me}]_2Be$.

3.5: Effects of Doping on Crystal Structure

Solid solutions of $[5\text{-Me}]_2B_{1-x}Be_x$ were grown despite the differences in their properties. Surprisingly, a full spectrum of dopant concentration was able to be crystalized up to x = 0.59. This is most likely due to the strong pi-association of pairs of PLY units which can possess one or two electrons,[10,12-15] and thus allows for the inclusion of the dopant. The inclusion of dopant exerted many changes on the crystal structure of the solid solutions. Figure 3.9 summarizes

these results in terms of the unit cell parameters and bandwidth of the solid solutions as a function of dopant concentration. The largest change occurs at x = 0.1, where the solid solutions change crystal structure from that of the triclinic host to that of the monoclinic dopant. This demonstrates the importance of the radicals in the packing structure of neutral radical conductors.

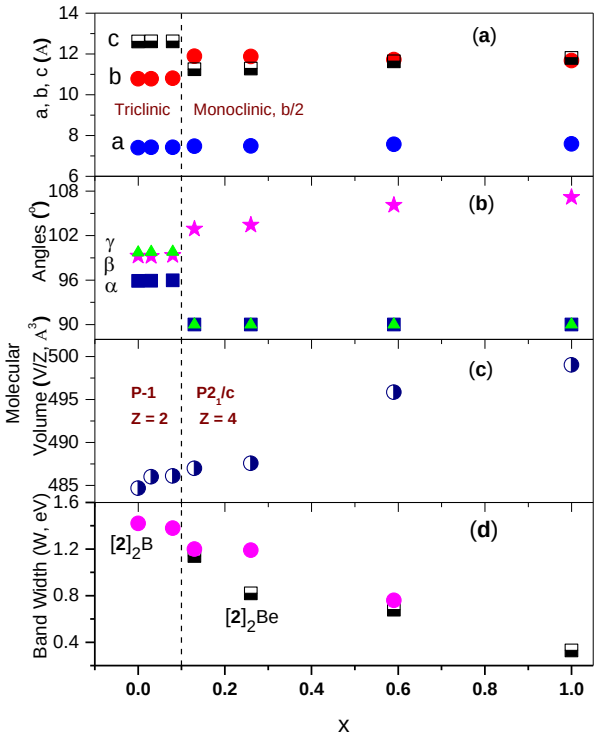

Figure 3.9: Effects of doping on unit cell parameter and bandwidth as a function of dopant concentration (x).

While the overall structure of the solid solutions goes from the 1-D chain structure of the host to the dimeric structure of the dopant, there are still some differences between the solid solutions. Figure 3.10 shows the evolution of a

PLY-PLY interaction as doping is increased. At concentrations of x = 0.0 and 0.08 the overlap of the spin bearing carbons remains. After this the unit cell changes and the PLY units begin to slip away from one another. This slippage is not abrupt but occurs slowly as doping is increased. This can be seen in the differences from x = 0.13 to x = 1 where the spin bearing carbon distance is slowly increased. Overall, it can be seen that doping causes large changes in the crystal structure of the solid solutions.

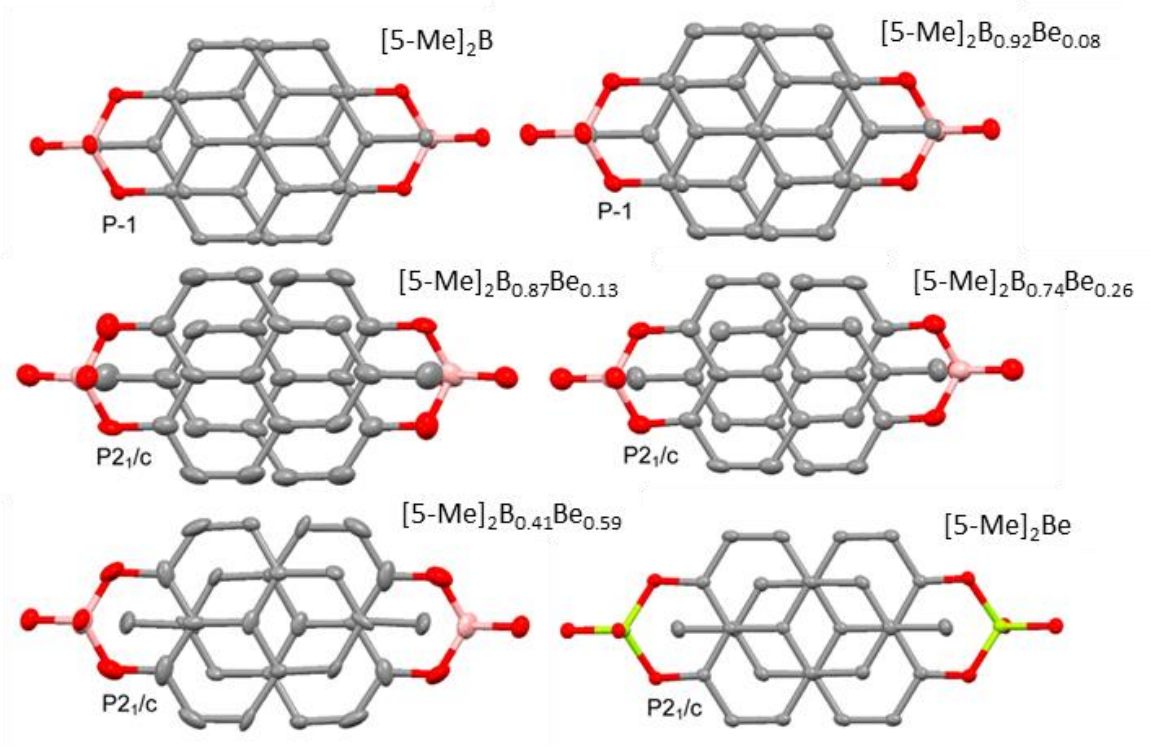

Figure 3.10: Effects of doping on the PLY-PLY interaction.

3.6: Effects of Doping on Electrical Conductivity

As previously stated, the main goal of substitutional doping here is an increase in conductivity leading to a metallic or superconducting state. Figure

3.11 summarizes the effects of doping on the electrical conductivity of the solid solutions. It can be seen in Figure 3.11a that the conductivity remains semiconducting (positive temperature coefficient) throughout all doping concentrations. Figure 3.11b shows the room temperature conductivity as a function of doping. Here it can be seen that doping does in fact increase the conductivity, with a maximum of double the original conductivity at x =0.09 from 0.3 to 0.6 S/cm. After this point, the crystal structure changes and the conductivity starts falling. It is interesting to note that at concentrations of x = 0.13 the conductivity is equal to the conductivity of the original compound despite switching from a 1-D chain structure to a dimeric structure. Figure 3.11c shows the activation energy (slope of lines in Figure 3.11a). The activation energy is related to the bandgap (about ½ the bandgap in intrinsic semiconductors), and it can be seen that the activation energy is lowered and stays low throughout the crystal structure change and does not increase until x = 0.4. This correlates well with the PLY-PLY overlap shown in Figure 3.10 in which the full slippage does not occur until concentrations greater than x = 0.26.

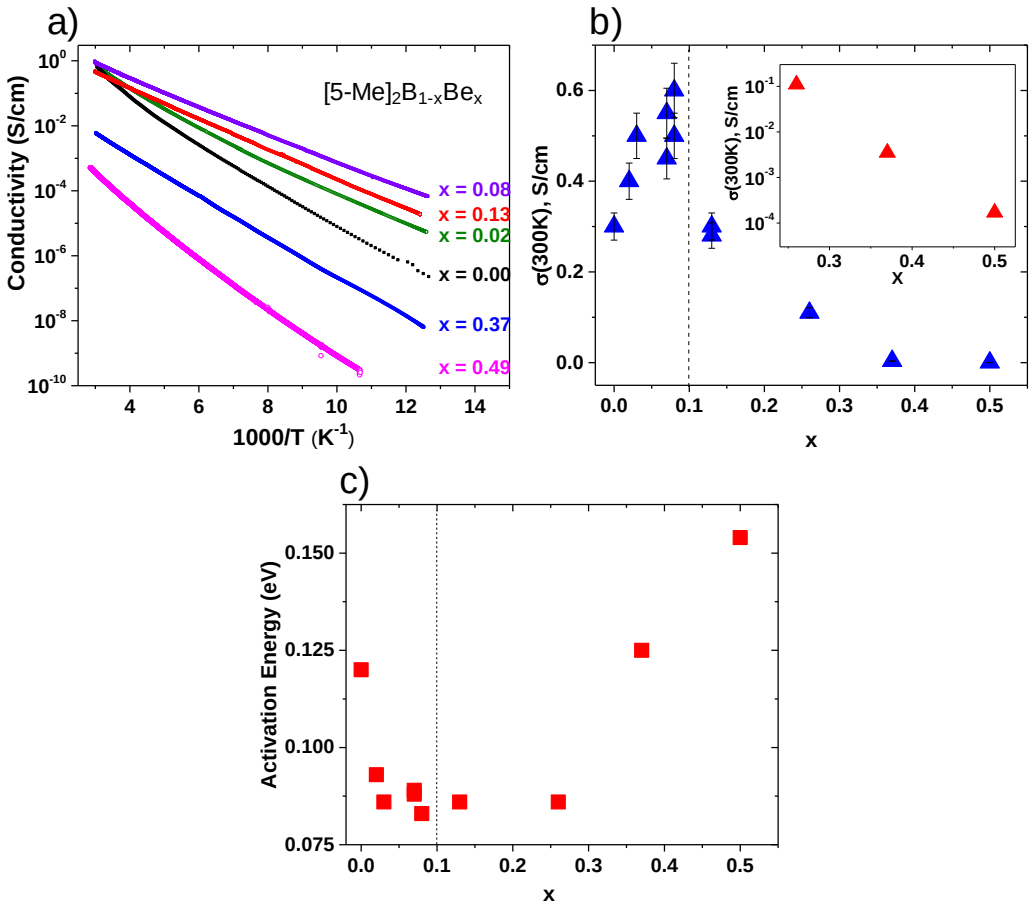

Figure 3.11: Effect of doping on electrical conductivity as a (a) function of temperature. (b) Room temperature conductivity and (c) activation energy as a function of doping concentration. The inset shows a zoomed in picture when x >0.25.

Overall, the increase in conductivity is quite surprising due to the differences in the redox properties of the host and dopant. If viewed from the silicon-based model of substitutional doping, this increase should not occur. However, if viewed from the RVB model discussed in Chapter 1, these increases are not as surprising as doping may disrupt the antiferromagnetic coupling resulting in an increase in conductivity.[16-18]

3.7: Effects of Doping on Magnetic Properties

Along with the electrical conductivity properties, substitutional doping of [5-Me]$_2$B was also found to have large effects on the magnetic properties of the solid solutions. Figure 3.12a summarizes these changes as a function of temperature at various doping concentrations, and Figure 3.12b summaries the fraction of Curie spin at room temperature as a function of doping concentration.

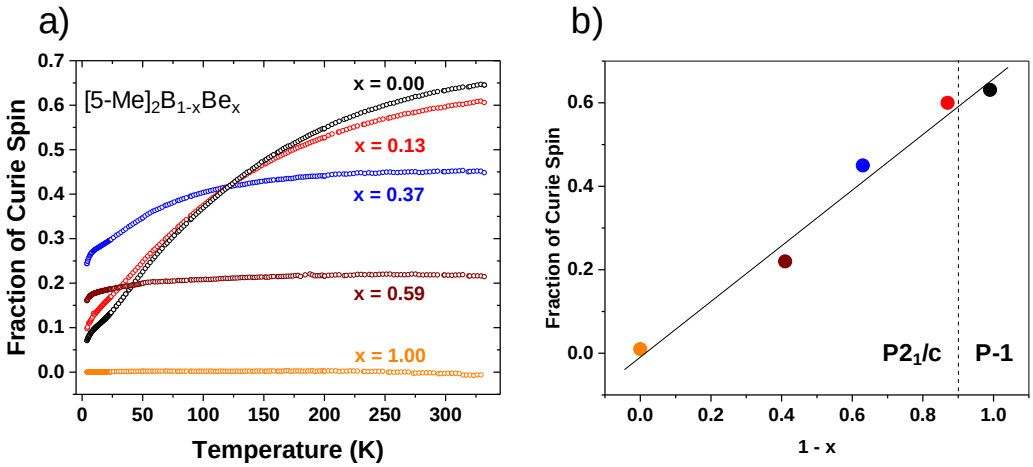

Figure 3.12: (a) Fraction of Curie Spin as a function of temperature at various dopant concentrations and (b) the fraction of Curie Spin at room temperature as a function of doping concentration.

There are two main changes here. The first is the linear reduction in the fraction of Curie Spin as doping is increased, which is an expected result for replacing spin containing [5-Me]$_2$B with spinless [5-Me]$_2$Be. The second effect is the reduction of temperature dependence of the Curie spin as a function of temperature as seen in Figure 3.12a. This indicates that in the dimer state, the dimers are made up of [5-Me]$_2$B-[5-Me]$_2$Be interactions which would contain one

unpaired electron. This single electron dimer is analogous to the monomeric structure as discussed in Chapter 1.

3.8: Conclusion

In conclusion, we have substitutionally doped a phenalenyl based neutral radical conductor, $[5\text{-Me}]_2B$, with its non-radical containing derivative, $[5\text{-Me}]_2Be$, which serves as a p-type dopant. We found that the doping increases the conductivity of the solid solutions by a factor of 2 until the dopant causes severe changes in the crystal structure. While the increase in conductivity is unexpected based on the electrochemistry of the compounds when viewed through the substitutionally doped silicon model, it is expected from the RVB model. The doping also has large effects on the magnetic properties of the solid solutions, causing them to behave more like monomeric compounds. These results demonstrate a novel way to modify the properties of organic semiconducting materials and while substitutional doping has proved effective, is still far from being fully understood and warrants further investigation.

3.9: Experimental

Materials

All reactions and manipulations were carried out under an atmosphere of dry argon using standard Schlenk and vacuum-line techniques or in argon filled gloveboxes.The reagents 1.0M BCl_3 solution in Hexane (Aldrich), $Be(acac)_2$ (Aldrich), Tetrakis(dimethylamino)ethylene (TDAE) (TCI America) and Potassium

tetrakis(pentafluorophenyl)borate (K^+TFAB^-) (Boulder Scientific Company) were used as received. $[2]_2B^+TFAB^-$ was synthesized according to literature procedures[3] and $[2]_2Be$ was synthesized by a modification of the original procedure.[19,20] Dry acetonitrile and chlorobenzene were purchased from Aldrich. Cyclic voltammetric measurement were performed on a CH instrument using a Pt disk electrode in dry acetonitrile under argon atmosphere with *n*-Bu_4NPF_6 as the supporting electrolyte with a standard calomel reference electrode and the ferrocenium/ferrocene couple was used as internal reference. ESI mass spectra were recorded with an Agilent LCTOF (2006) machine with APCI/ESI ionization. MALDI mass spectra were obtained on a Voyager-DE STR BioSpectrometry Workstation mass spectrometer. NMR spectra were recorded on a Bruker 300 spectrometer. Elemental analyses and inductively coupled (ICP) mass spectrometry analyses of the $[5\text{-Me}]_2B_{1-x}Be_x$ samples (10 mg) were performed by the Microanalysis Laboratory, University of Illinois, Urbana Champaign, IL.

Synthesis of $[5\text{-Me}]_2Be$

Beryllium acetylactonate (1 mmol, 0.207 g) was added to a stirred THF (20 mL) solution of 5-methyl-9-hydroxyphenalenone (2 mmol, 0.42 g)[20] in an argon atmosphere, and the mixture was stirred at 60 °C for 2 days. The yellow solid which deposited was filtered and washed with ether. Yield 0.32 g (75%). mp. >350 °C; ^1H NMR (300 MHz, $CDCl_3$): δ 8.13 (2H, d), 7.90 (dH, s), 7.24 (2H, d),

2.64 (3H, s) ppm; ESI-MS: m/z calcd. for $C_{28}H_{19}O_4Be$ [MH^+], 428.1405, found 428.1425; Anal. Calcd. (found) for $C_{28}H_{18}O_4Be$: C, 78.68 (78.55); H, 4.24 (4.30).

General Method of Synthesis and Crystallization of Doped Radicals $[5\text{-Me}]_2B_{1-x}Be_x$

In a typical experiment (preparation of $[5\text{-Me}]_2B_{0.74}Be_{0.26}$) which was conducted in a glove box, a solution of 13 mg (3.04×10^{-5} mol) of $[2]_2Be$ in 10 mL dry chlorobenzene was transferred to a vial containing 33.7 mg (3.04×10^{-5} mol) of $[2]_2B^+$ $TFAB^-$. To this homogeneous solution, a drop of TDAE was added, and the vial was left undisturbed overnight. The black shining needle-shaped crystals (11 mg, yield 42%) which deposited on the walls of the vial were collected by filtration and washed with acetonitrile. The beryllium content (x = 0.26) was established by ICP analysis, and the compound was characterized by bulk magnetic susceptibility, single crystal x-ray diffraction and four probe conductivity measurements. Crystals with other beryllium compositions (x = 0.02, 0.03, 0.08, 0.13, 0.26, 0.37, 0.49 and 0.59) were synthesized and crystallized by similar procedures.

X-ray Crystallography.

Full details of the crystallography are included in the literature. A black thin plate-like fragment was used for the single crystal x-ray diffraction study of $[2]_2B_{0.74}Be_{0.26}$; the crystal was coated with paratone oil and mounted on a cryo-

loop glass fiber. X-ray intensity data were collected at 100(2) K on a Bruker APEX2 platform-CCD x-ray diffractometer system (fine focus Mo-radiation, λ = 0.71073 Å, 50KV/35mA power). Absorption corrections were applied to the raw intensity data using the SADABS program. Atomic coordinates, isotropic and anisotropic displacement parameters of all the non-hydrogen atoms were refined by means of a full matrix least-squares procedure on F2. The H-atoms were included in the refinement in calculated positions riding on the atoms to which they were attached.

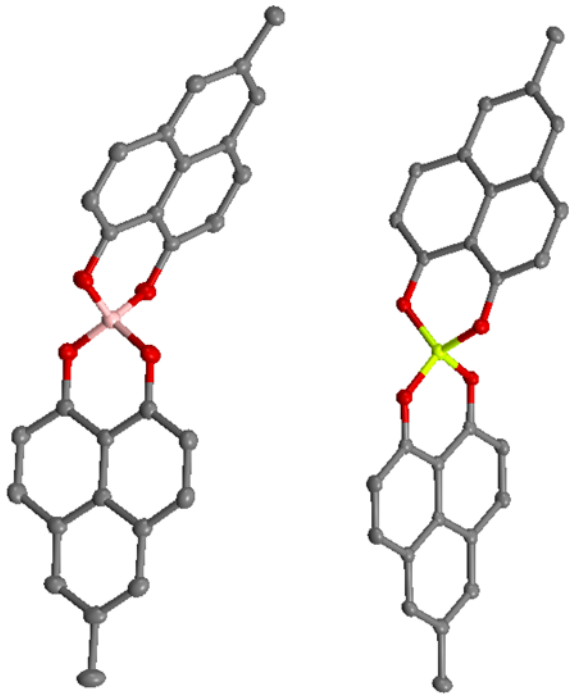

Figure 3.13: Thermal ellipsoids of (left) $[5\text{-Me}]_2B$ and (right) $[5\text{-Me}]_2Be$.

Table 3.1: X-ray crystallographic data of $[5\text{-Me}]_2$Be and $[5\text{-Me}]_2$B.

Compound	$[5\text{-Me}]_2$Be	$[5\text{-Me}]_2$B
Empirical formula	C28 H19 O4 B	C28 H19 O4 Be
Formula weight (g/mol)	430.26	428.46
Temperature (K)	100	100
Crystal system	Triclinic	Monoclinic
Space group	*P*-1	*P* 2_1/c
Unit cell dimensions		
a (Å)	7.3847	7.5857
b (Å)	10.7758	23.3505
c (Å)	12.6337	11.7938
α (deg)	95.650	90
β (deg)	99.3230	107.1530
γ (deg)	99.6940	90
V Å^3	968.958	1996.12
Z	2	4

Conductivity Measurements

The single crystal conductivities were measured in a four probe configuration using in line contacts which were made with silver paint. The sample was placed on a sapphire substrate, and electrical connections between the silver paint contacts and substrate were made by thin flexible 25 μm diameter silver wire to

relieve mechanical stress during thermal cycling of the sample. The conductivities were measured along the long axis of the crystals. The conductivity was measured in a custom made helium variable temperature probe using a Lake Shore 340 temperature controller in the temperature range 330 – 77K. A Keithley 236 unit was used as a voltage source and current meter, and two 6517A Keithley electrometers were used to measure the voltage drop between the potential leads in a four probe configuration in which the instrumentation was driven with LabVIEW software.

Magnetic Susceptibility Measurements

The molar magnetic susceptibility of 10-15 mg samples of the crystalline powders were measured by utilizing a Vibrating Sample Magnetometer in an EverCool-II cryogen-free upgraded version of a Physical Property Measurement System (Quantum Design International, USA) in a magnetic field of 1 Tesla over the temperature range 330 – 4 K.

3.10: References

1) Pal, S. K.; Itkis, M. E.; Tham, F. S.; Reed, R. W.; Oakley, R. T.; Haddon, R. C. *Science* **2005**, *309*, 281.

2) Bag, P.; Itkis, M. E.; Pal, S. K.; Donnadieu, B.; Tham, F. S.; Park, H.; Schleuter, J. A.; Siegrist, T.; Haddon, R. C. *J. Am. Chem. Soc.* **2010**, *132*, 2684.

3) Mandal, S. K.; Samanta, S.; Itkis, M. E.; Jensen, D. W.; Reed, R. W.; Oakley, R. T.; Tham, F. S.; Donnadieu, B.; Haddon, R. C. *J. Am. Chem. Soc.* **2006**, *128*, 1982.

4) Porter III, W. W.; Vaid, T. P.; Rheingold, A. L. *J. Am. Chem. Soc* **2005**, *127*, 16559

5) Porter III, W. W.; Vaid, T. P. *J. Mater. Chem.* **2007**, *17*, 469

6) Bryan, C. D.; Cordes, A. W.; Haddon, R. C.; Hicks, R. G.; Kennepohl, D. K.; MacKinnon, C. D.; Oakley, R. T.; Palstra, T. T. M.; Perel, A. S.; Scott, S. R.; Schneemeyer, L. F.; Waszczak, J. V. *J. Amer. Chem. Soc* **1994**, *116*, 1205.

7) Seber, G.; Freitas, R. S.; Mague, J. T.; Paduan-Filho, A.; Gratens, X.; Bindilatti, V.; Oliveira, N. F.; Yoshioka, N.; Lahti, P. M. *J. Am. Chem. Soc* **2012**, *134*, 3825.

8) Pal, S. K.; Bag, P.; Itkis, M. E.; Tham, F. S.; Haddon, R. C. *J. Am. Chem. Soc;* **2014**, *136*, 14738.

9) Tian, Y.-H.; Sumpter, B. G.; Du, S.; Huang, J. **2015**, 2318

10) Mota, F.; Miller, J. S.; Novoa, J. J. *J. Am. Chem. Soc.* **2009**, *131*, 7699.

11) Cui, Z.; Lischka, H.; Beneberu, H. Z.; Kertesz, M. *J. Am. Chem. Soc* **2014**, *136*, 5539

12) Small, D.; Zaitsev, V.; Jung, Y.; Rosokha, S. V.; Head-Gordon, M.; Kochi, J. K. *J. Am. Chem. Soc.* **2004**, *126*, 13850.

13) Small, D.; Rosokha, S. V.; Kochi, J. K.; Head-Gordon, M. *J. Phys. Chem. A* **2005**, *109*, 11261.

14) Suzuki, S.; Morita, Y.; Fukui, K.; Sato, K.; Shiomi, D.; Takui, T.; Nakasuji, K. *J. Am. Chem. Soc.* **2006**, *128*, 2530

15) Cui, Z. H.; Lischka, H.; Beneberu, H. Z.; Kertesz, M. *J. Am. Chem. Soc.* **2014**, *136*, 12958.

16) Anderson, P. W. *Mater. Res. Bull.* **1973**, *8*, 153.

17) Anderson, P. W. *Science* **1987**, *235*, 1196.

18) Pauling, L. *Nature* **1948**, *161*, 1019.

19) Haddon, R. C.; Chichester, S. V.; Marshall, J. H. *Tetrahedron* **1986**, *42*, 6293.

20) Haddon, R. C.; Rayford, R.; Hirani, A. M. *J. Org. Chem* **1981**, *46*, 4587.

Chapter 4: Effect of Substitution on the Hysteretic Phase Transition in a Bistable Phenalenyl Based Neutral Radical Molecular Conductor

4.1: Introduction

In chapter 3 we showed how substitutional doping in neutral radical conductors could increase the conductivity and alter the magnetic properties of the materials. We also showed that this substitution has large effects on the crystal structure of the solid solutions. While one purpose of substitutional doping in inorganic semiconductors and materials is the enhancement of electrical conductivity, another purpose is to augment other properties of the materials, such as phase transitions. One of the most popular inorganic materials known for its phase transition is vanadium oxide (VO_2). VO_2 experiences a phase transition from its insulating monoclinic phase to a metallic rutile phase around 340 K accompanied by large changes in its optical properties.[1] Due to its potential uses, control of this phase transition has been extensively studied.

One way to affect this transition is through substitutional doping. Scientists have doped VO_2 by switching out vanadium atoms for other metals such as titanium, tungsten, and molybdenum among many others. Through this doping it has been shown that the phase transition can be lowered to room temperature, the width of the hysteretic loop can be decreases or completely eliminated, and the phase transition itself can be completely suppressed.[1-6] The results of these studies and related work on the tuning of the VO_x stoichiometry (x = 1.5-2.5)

have engineered the properties for uses in switching, sensing, smart windows, and night vision applications.[7-10]

Considering the number of developed and potential applications of bistable materials and materials with phase transitions in the vicinity of room temperature, it would be interesting to apply substitutional doping on an organic molecular conductor. The following is a study of the effects of substitutional doping on the phase transition in phenalenyl based neutral radical conductor and its near room temperature bistability.

4.2: Hysteretic Phase Transition in $[Bu]_2B$ with Bistability in the Vicinity of Room Temperature

The structure of bis(9-N-butylamino-1-oxophenalene)boron ($[Bu]_2B$) is shown in Figure 4.1. While similiar to the neutral radical discussed in Chapter 3, $[5\text{-}Me]_2B$, this radical lacks the methyl group at the 5 position and contains a butylamine at the 9 position as opposed to the oxygen.

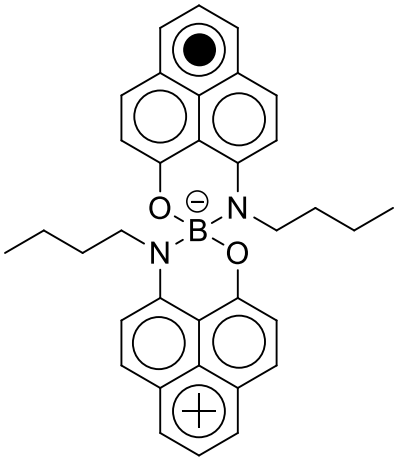

$[Bu]_2B$

Figure 4.1: The structure of $[Bu]_2B$.

Since its first crystallization,[11] $[Bu]_2B$ has garnered much attention due to its near room temperature phase transition illustrated in Figure 4.2. It is one of the very few organic compounds with bistability in the vicinity of room temperature.[12-16] At low temperatures, $[Bu]_2B$ forms dimeric pairs of molecules with a pair of superimposed phenalenyl (SPLY) units and 2 non-superimposed phenalenyl (NSPLY) units. The radicals pair antiferromagnetically into a low spin (LS) state within the SPLY units in what can be described as a 2-electron pancake bond with a short intradimer space (3.11Å). This results in a singlet state and one in which the Curie Spin per molecule is temperature independent and equal to ~0. This antiferromagnetic state is maintained until the temperature is increased from ~200K as the electron wavefunction spreads throughout the molecule and eventually occupy both the SPLY and NSPLY units equally. It leads to the appearance of the temperature dependent fraction of Curie Spin per molecule and an increase of the intradimer space to 3.27 Å. At temperatures above ~325 K a high spin (HS) state in which the electrons are located on the NSPLY is energetically favored, however there is a large energy barrier due to the accompanying increase in unit cell size in part due to the increase in the intradimer spacing but mostly from the increase in interdimer spacing and thus the LS state is preserved. Then, at ~345 K the electrons rapidly migrate to the NSPLY in which they are, for the most part, noninteracting and in a high spin (HS) triplet state. This results in a monomeric type structure which is accompanied by a large change in the unit cell dimensions as the intradimer

space is further increased to 3.38 Å, similar to the van der Waals distance of carbon. At that instance, the interdimer spacing (C-H interaction) is increased from 2.92Å to 3.16Å. Upon cooling, this HS state is maintained below the original phase transition temperature of ~345 K until ~325 K and the material returns to its energetically favorable LS state. As was discussed above, the resulted hysteresis is due to the large energy barrier associated with a dramatic increase in unit cell size in part due to the increase in the intradimer spacing but mostly from the increase in interdimer spacing. In addition to the discussed magnetic bistability, this phase transition manifests itself in the bistable electrical and optical properties. Throughout this phase transition the monoclinic ($P2_1/c$) is maintained.[17,18]

This phase transition has been studied extensively both experimentally and computationally and further discussion can be found in the literature.[11,17-24]

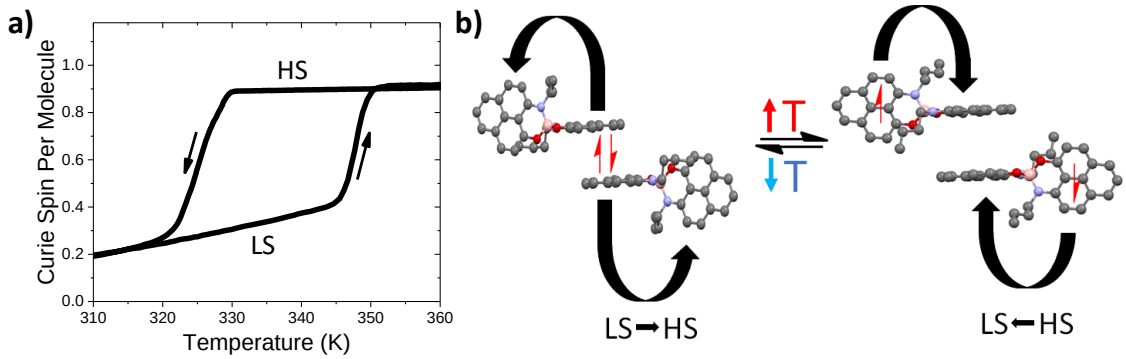

Figure 4.2: (a) Fraction of Curie Spin as a function of temperature around the phase transition of $[Bu]_2B$ and (b) a diagram of the phase transition.

4.3: Synthesis and Crystallization of Substitutional Doped $[Bu]_2B_{1-x}Be_x$

Similar to the substitutional doping experiments in Chapter 3,[25,26] $[Bu]_2B$ is substitutionally doped with its non-radical containing counterpart, $[Bu]_2Be$, to form solid solutions of $[Bu]_2B_{1-x}Be_x$ (Figure 4.3).

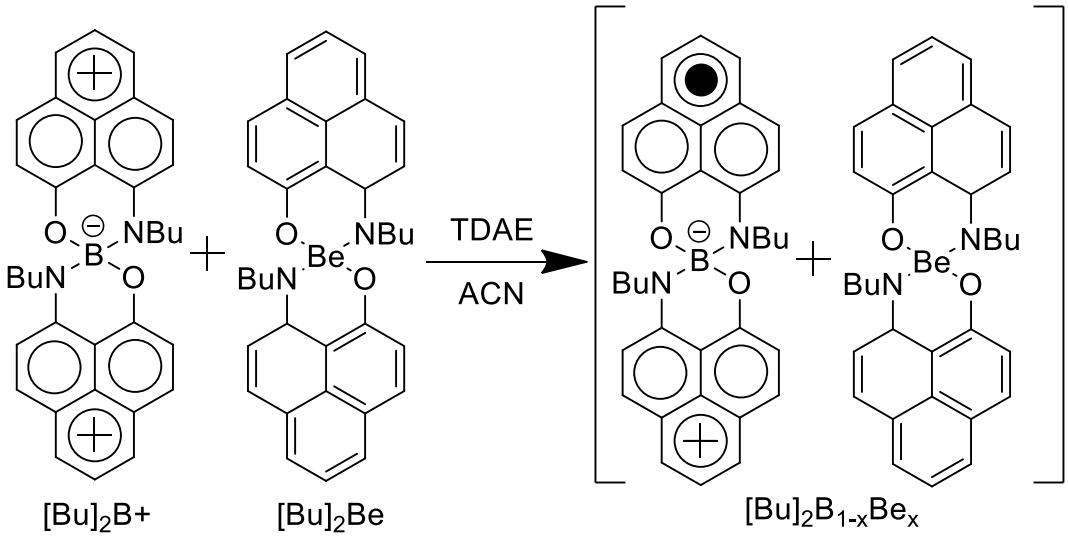

Figure 4.3: The co-crystallization procedure for substitutional doping: The cationic precursor of $[Bu]_2B$ is combined with the dopant, $[Bu]_2Be$, and a reductant (tetrakis(dimethylamino)ethylene (TDAE)) is added to grow solid solutions of $[Bu]_2B_{1-x}Be_x$.

The first observed difference due to substitution is the morphology of the solid solutions. Pure $[Bu]_2B$ appears as black block-like crystals (Figure 4.4a). When substitution with $[Bu]_2Be$ is introduced the crystals elongate and grow needle like (Figure 4.4b). Increasing the amount of $[Bu]_2Be$ results in the growth of more needle like thinner crystals (Figure 4.4c). Thus, the presence or lack of substitution can be determined by simply looking at the morphology of the crystals. $[Bu]_2Be$ is a yellow-orange powder and can be crystalized into various sizes (Figure 4.4d).

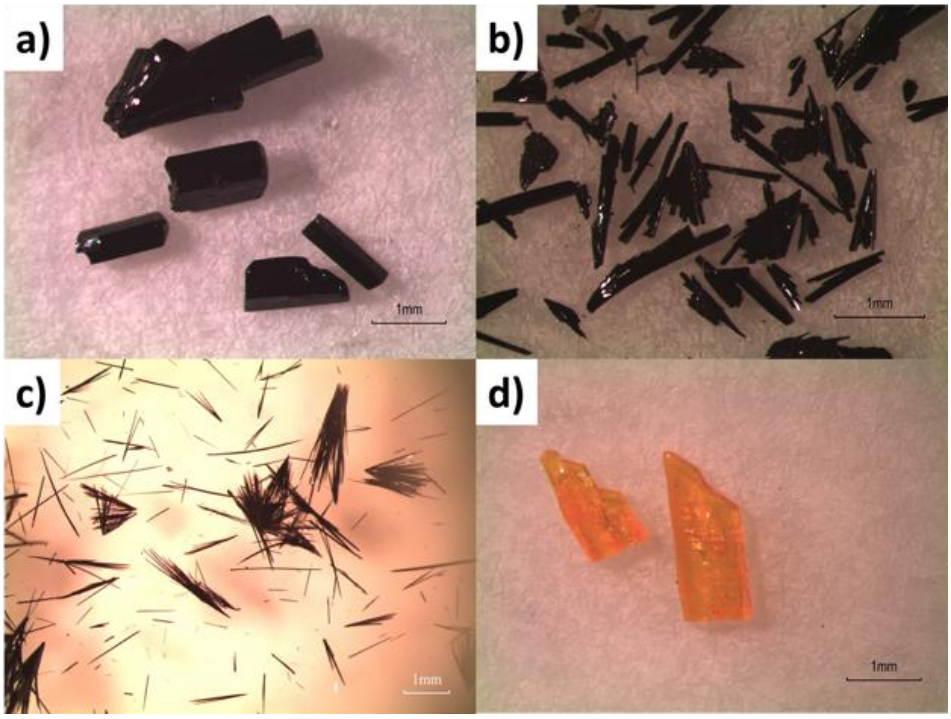

Figure 4.4: Pictures of crystals of (a) $[Bu]_2B$, (b) lightly doped $[Bu]_2B_{1-x}Be_x$, (c) heavily doped $[Bu]_2B_{1-x}Be_x$ and (d) $[Bu]_2Be$. The scale bars are 1 mm.

4.4 Host and Dopant Structure Comparison

As it was shown in Chapter 3, the structure of the host and dopant are important when it comes to substitutional doping experiments.

As established in earlier publications by Haddon research group, the crystal packing of $[Bu]_2B$ corresponds to a $P2_1/c$ space group.[11,17] Figure 4.5 shows an interacting pair (dimer) of $[Bu]_2B$ molecules in 2 views perpendicular to each other in their low spin, low temperature state and their high spin, high temperature state. As can be seen in Figure 4.5a, the interfacial distance is significantly lower (3.11 Å) than the van der Waals distance for a carbon-carbon bond (3.4 Å), due to the presence of interfacial pancake bonding in the low spin state.[27,28] Figure 4.5c shows the same crystal in its high spin state. Here the

interfacial distance is increased (3.39 Å) to approximately the van der Waals distance. This increase of interfacial distance is attributed to the movement of the spin from the superimposed to non-superimposed phenalenyl as the crystal transitions from its low spin to high spin state. Perpendicular views of both the low and high spin states are presented in Figure 4.5b, d. Here the spin bearing carbons are colored in green and it can be clearly seen that the pair of molecules have a high degree of overlap in both the high and low spin states. Both of these observations are attributed to the presence of a radical. This highly overlapped and short distance interfacial interaction is responsible for the low spin state as the radicals with opposite spin pair up.

In contrast, $[Bu]_2Be$, introduced for the 1st time in this study, does not contain a radical, packs in a *P*-1 space group, and contains 4 molecules in the unit cell. The structure of $[Bu]_2Be$ (at 100 K) (Figure 4.5e-h) is dramatically different than that of $[Bu]_2B$, most likely due to its lack of spin. While $[Bu]_2B$ forms dimers with short interfacial distances and has one interfacial interaction, no such dimers in $[Bu]_2Be$ are observed. As can be seen in Figure 4.5e, g the interfacial distances (3.39 Å, 3.33 Å) are significantly greater than that observed in the LS state of $[Bu]_2B$ at the same temperature (100 K). Not only is the distance increased, but the overlap of the spin bearing carbons is very poor as can be seen in figure 4.5f, h, as none of them overlap (green). This is attributed to $[Bu]_2Be$ not possessing a radical, and thus it is unable to form pancake bonds

between neighboring molecules which would shorten interfacial distances and increase spin-bearing carbon overlap.

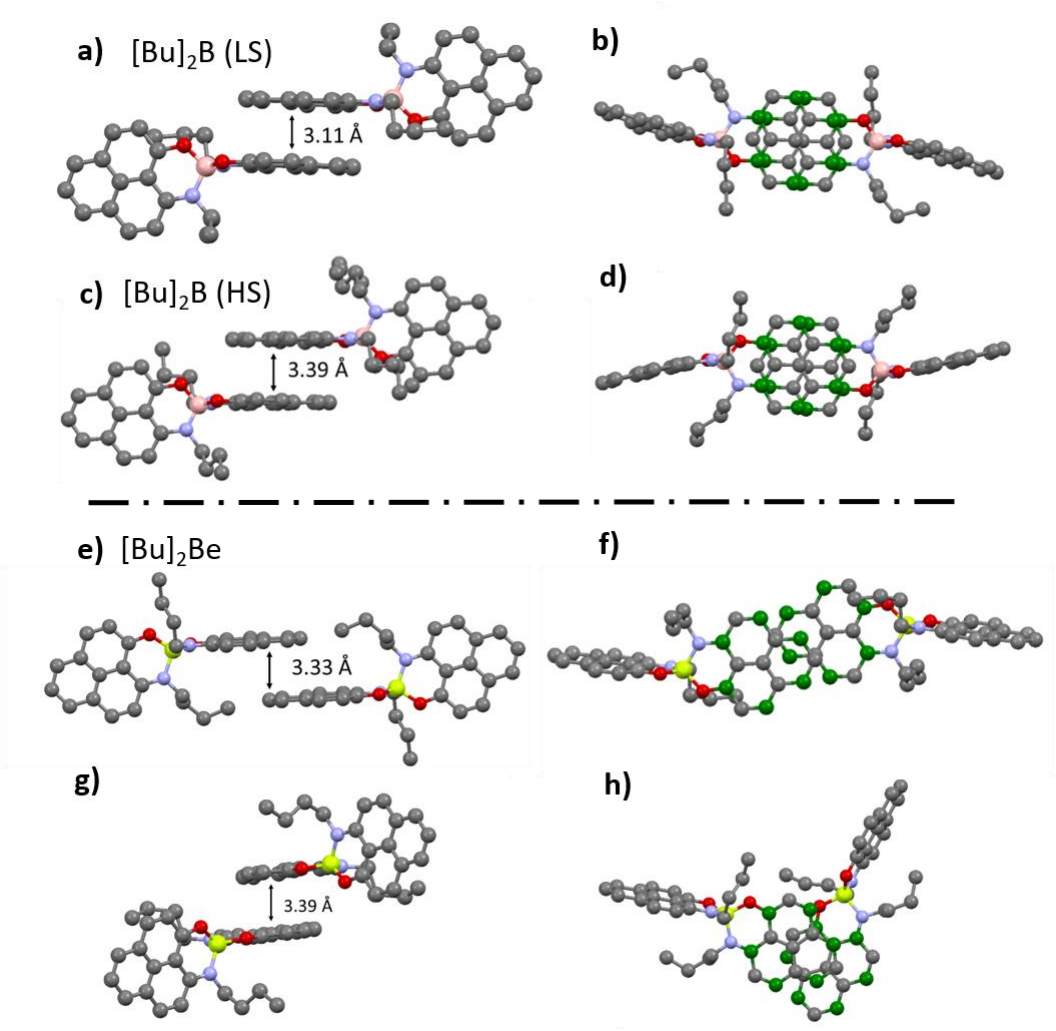

Figure 4.5: Perpendicular views of $[Bu]_2B$ dimers in its (a, b) low spin and (c, d) high spin states showing interfacial distances and high degree of overlap between spin-bearing carbons shown in green. (e-h) Views of $[Bu]_2Be$ crystal interactions showing larger interfacial distances and little to no overlap of spin-bearing carbons shown in green.

4.5: Crystal Structures in Doped $[Bu]_2B_{1-x}Be_x$ Solid Solutions

In Chapter 3 the single crystal structures of solid solutions were solved, however, this is a complicated task. The complete single crystal X-ray study of crystal structures of pure $[Bu]_2B$ and $[Bu]_2Be$ were studied above. For solid solutions of mixed composition, powder X-ray diffraction (pXRD) measurements were taken. This allows for the exploration of the crystal structure in a significantly less time and effort costly manner.

Figure 4.6 presents room temperature powder XRD data for pristine $[Bu]_2B$ (x = 0) and $[Bu]_2Be$ (x = 1). It shows very distinct patterns corresponding to different crystal packing in $[Bu]_2B$ and $[Bu]_2Be$ compounds with a set of major peaks positioned at diffraction angles 2θ of 8.1, 10.4, 13.3 and 16.4 degrees for the $[Bu]_2B$ compound (indicated with an asterisk symbol) and at 7.7, 12.1, 22.4 and 25.7 degrees for $[Bu]_2Be$ (indicated with a delta symbol). In addition, a group of characteristic peaks is observed in the range of 2 θ of 20-25 degrees in the case of $[Bu]_2B$. Single crystal X-ray data for $[Bu]_2B$ and $[Bu]_2Be$ were utilized to simulate powder XRD patterns and the good match can be found between calculated and experimental powder XRD data as shown in Figure 4.11.

The modification of the powder XRD pattern of $[Bu]_2B_{1-x}Be_x$ solid solutions with increasing doping level is also presented in Figure 4.6. It can be clearly seen that low substituted solid solutions ($x<0.06$) bear the same phase as pure $[Bu]_2B$ with major peaks in powder XRD pattern remaining at 2 θ of 8.1, 10.4, 13.3 and 16.4 degrees. No additional peaks corresponding to the phase of $[Bu]_2Be$ are

observed. This indicates that $[Bu]_2Be$ is being incorporated into the crystal structure of $[Bu]_2B$. This observation is not surprising as it is known that the presence of radicals plays a large role in the crystal structure, and other organic radical compounds have shown that one electron is sufficient to form phenalenyl-phenalenyl pancake bonds.[28,29]

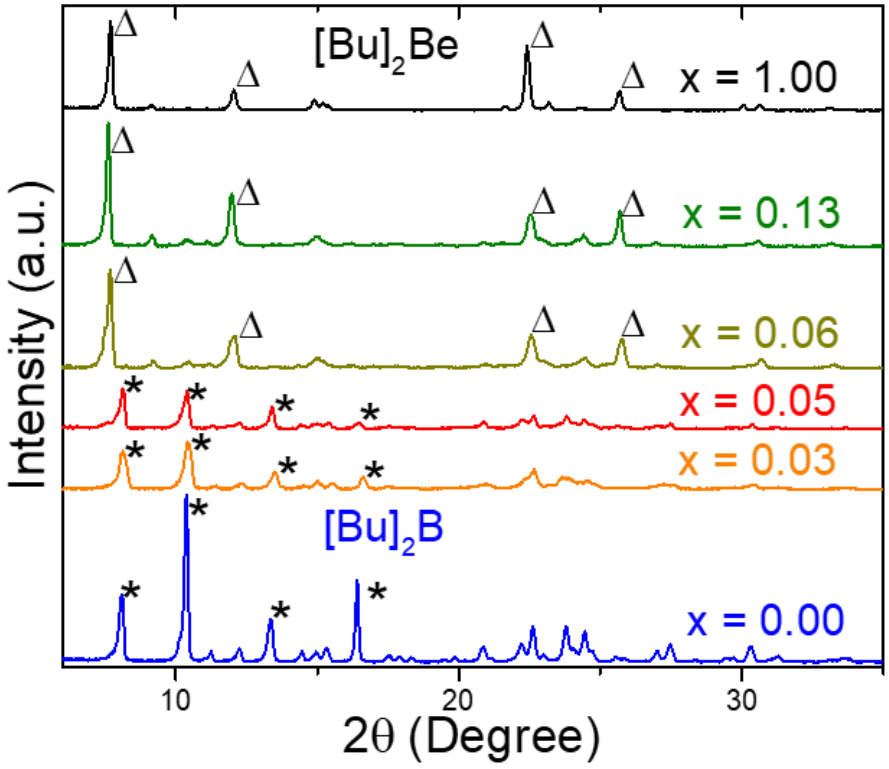

Figure 4.6: Powder X-ray diffraction data of solid solutions of $[Bu]_2B_{1-x}Be_x$ showing the transition of the structure from that of the host ($[Bu]_2B$) to that of the dopant ($[Bu]_2Be$).

Meanwhile, highly substituted solid solutions (x>0.06) match the phase of pure $[Bu]_2Be$ with major peaks shifting to 2 θ of 7.7, 12.1, 22.4 and 25.7 degrees and a disappearance of a group of characteristic peaks in the range of 2 θ of 20-

25 degrees associated with the $[Bu]_2B$ crystal packing. Even though the concentration of substituent is significantly lower than that of the $[Bu]_2B$ host, its presence is enough to completely alter the crystal packing structure. This demonstrates the importance of the radical on the crystal structure. No unique structure for the substituted solid solutions was observed which is consistent with our previous studies.[25] It seems as these substituted organic radical conductors behave as binary systems, that is, they take the form of either the host or the substitute. Thus, it is concluded that at low substitution levels the solid solutions adopt the structure of $[Bu]_2B$ and thus undergo the phase transition while at high substitution levels the solid solutions adopt the structure of $[Bu]_2Be$.

4.6: Magnetic Properties of Solid Solutions $[Bu]_2B_{1-x}Be_x$

Figure 4.7 shows magnetic susceptibility data as a function of temperature for different levels (x) of $[Bu]_2Be$ doping. As shown in Figure 4.7a the low temperature value of Curie spin per molecule in undoped $[Bu]_2Be$ material (x = 0) is approaching zero due to the antiferromagnetic coupling of two spins associated with the low temperature dimer structure (Figure 4.2b). With increasing temperature above 350 K a sharp phase transition to a high temperature (HT) high spin (HS) state is observed with the effective spin (per molecule) increasing to the value of 0.9, close to the one Curie spin per molecule expected from the ensemble of non-interacting spins in neutral radical organic molecular conductors when the dimer coupling is released (Figure 4.7a, b). With decreasing temperature below 325 K a sharp transition to low temperature (LT),

low spin (LS) state is observed thus restoring the dimerized state and completing the counterclockwise hysteresis loop. With an increasing level of doping the amplitude of spin changes decreases with a complete disappearance of hysteresis loop at concentration x > 6.3 % as shown in Figure 4.7c. However, in the vicinity of this critical concentration, we observed a rare event of reversing the hysteresis loop to the clockwise direction with an inverted relationship between low temperature and high temperature spin values (Figure 4.7d). For high substitution levels (x > 0.06) a weak temperature dependence of the effective spin is observed (Figure 4.7c) resembling the behavior of monomeric neutral radical conductors that contain bulky substituents with non-interacting spins.[30] At helium temperatures, the effective spin value decreases to ~0.1 level as long-range antiferromagnetic interaction takes over with reducing thermal fluctuations. Ultimately, no measurable paramagnetic contribution is observed in the pure (x = 1) spinless $[Bu]_2Be$ compound as would be expected due to the lack of a radical.

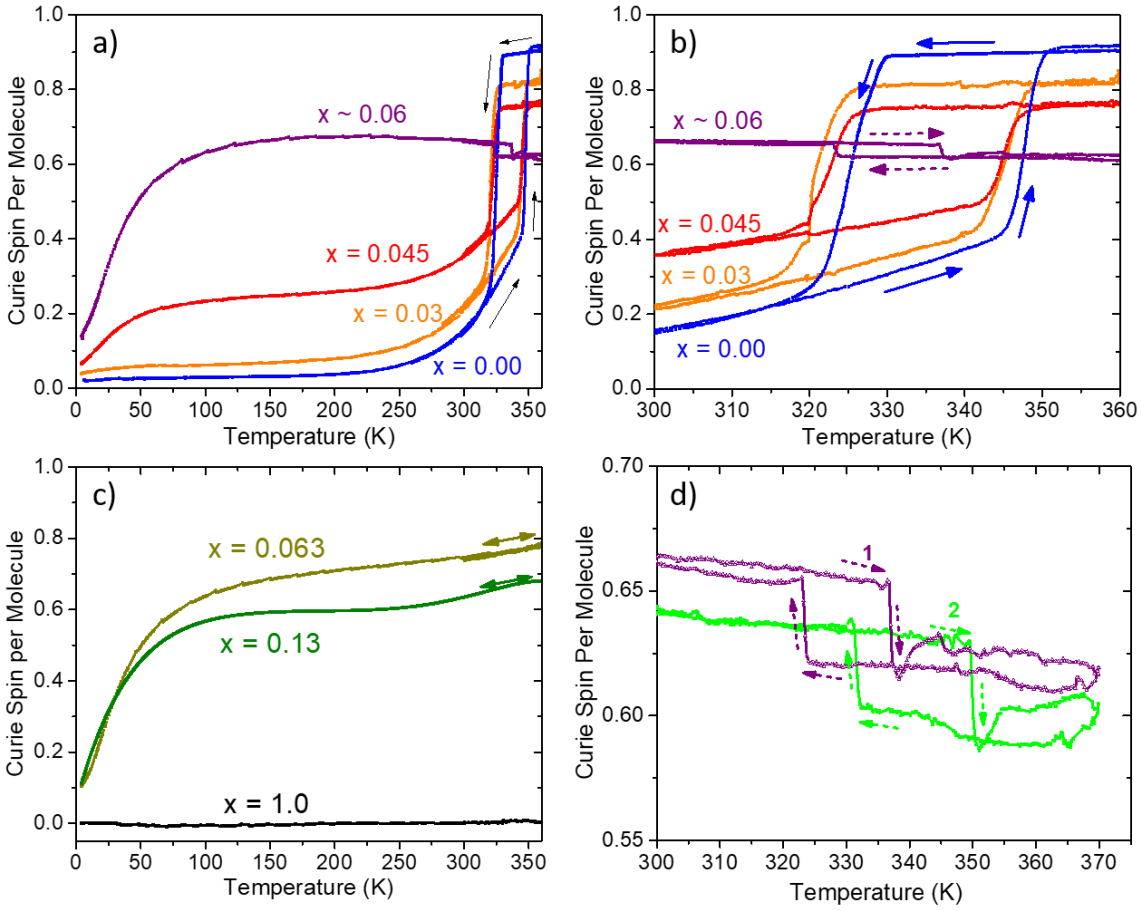

Figure 4.7: Temperature dependent fraction of Curie spin per molecule as a function of doping level x. (a) Lightly substituted $[Bu]_2B_{1-x}Be_x$: Compression of the height of the hysteresis loop with increasing doping; (b) Expanded view of the hysteresis loop above room temperature for lightly substituted $[Bu]_2B_{1-x}Be_x$ showing no phase transition; (d) Events of reverse hysteresis loop at x~6%.

Figure 4.8 presents an additional analysis of the evolution of the hysteretic phase transition with increasing doping. It shows that while the height of the hysteresis loop is reduced with increasing doping level (Figure 4.8a), the width of the loop remains approximately constant at the level of 23.5±1 K (Figure 4.8b). This is different from the case of vanadium oxide in which the width of the

hysteresis loop and temperature of phase transition modify significantly with increasing doping concentration.[1-6] The hysteresis loop height (Figure 4.8a) collapses to zero at the critical level of doping in the vicinity of x ≈ 6%. As shown in Figure 4.8c, both the decrease of the HS value and the increase of the LS value contribute to diminishing the loop height, however, the spin value *S* after the collapse, *S*=0.76 Curie spins/per molecule, is closer to the HS value indicating suppression of dimerization with increasing doping. As shown in Figure 4.8d, well below phase transition temperature, at 150 K, the dimerized state is very prominent for undoped [Bu]2B compound (x=0) showing an effective spin value close to zero. However, with increasing doping the effective spin per molecule at 150 K increases to 0.7 indicating a decoupling of the unpaired spins in neighboring molecules.

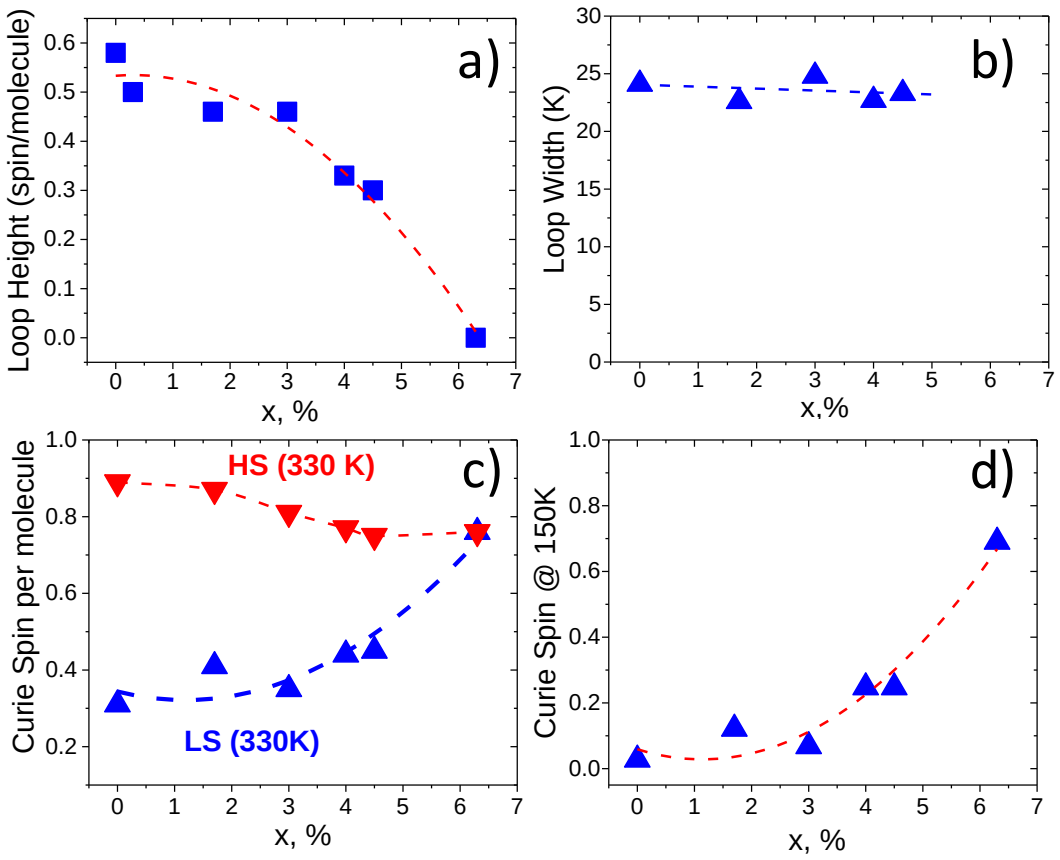

Figure 4.8: (a) Height and (b) width of the hysteretic loop as a function of doping. (c) Curie spin per molecule of the high spin (HS) and low spin (LS) states as a function of doping. (d) Curie spin per molecule at 150 K as a function of doping.

These observations can be partially explained by the change of number of the available spins with the introduction of a non-spin bearing molecule. When substitution is increased, the hysteretic loop is compressed vertically: in HS state maximum possible Curie spin per molecule decreases from 1 to (1-x) with the introduction of x fraction of spin non-bearing $[Bu]_2Be$ molecules; in the LS state x fraction of spin-bearing $[Bu]_2B$ molecules would not be able to find a pair to form a dimer thus contributing to an increase of LS value. However, the observed

decrease of HS value and increase of LS value are stronger than what would be expected from (1-x) and x contributions, respectively, taking into account low concentrations x not exceeding 6% sufficient for the collapse of the phase transition loop. More likely, some changes of the crystal structure with the introduction of non-spin bearing substitutes at low concentrations are responsible for the dramatic effect of substitutional doping on the hysteretic phase transition in $[Bu]_2B$ molecular crystals.

The presence of hysteresis and bistable physical properties of undoped $[Bu]_2B$ molecular crystals were originally ascribed to the existence of the energy barrier for the transition between LT and HT polymorphs.[17] Recently, the nature of this energy barrier was investigated in a computational study by the Ribas-Arino[20,22] group and related to the gauche to anti conformational rearrangement of the butyl groups attached to nitrogen atoms on both sides of the boron atom accompanied by a significant expansion of the crystal in HT phase, followed by a change of magnetic state from LS to HS. The study found that out of four possible polymorphs LS(gauche), LS(anti), HS(gauche) and HS(anti) only LS(gauche) and HS(anti) are thermodynamically stable at low and high temperatures, respectively. Observation of a reverse hysteresis loop (Figure 4.7b, d) with the low temperature spin value exceeding high temperature spin may manifest a situation when with increasing substitutional doping two other polymorphs, LS(anti) and HS(gauche), are becoming thermodynamically

accessible. However, the rarity of the reverse hysteresis event complicates its more detailed and conclusive study.

4.7: Electrical Conductivity of Solid Solutions $[Bu]_2B_{1-x}Be_x$

The phase transition in $[Bu]_2B$ is also observed in its electrical conductivity measurements (Figure 4.9). During the phase transition, $[Bu]_2B$ goes from a higher conductance LT, LS state to a more resistive HT, HS state. The more than an order of magnitude increase of conductivity in LT, LS state was explained in a computational study by Kertesz group by an analysis of the band splitting originating from intramolecular spiroconjugation at the central boron atom, π-π intermolecular interaction in the solid state due to dimer formation, and additional band splitting due to the presence of two sets of dimers in the unit cell $[Bu]_2B$ crystal resulting in different bandgaps in the LS and HS states.[19,24] In some of the warming-cooling cycles the whole conductivity change occurs instantaneously in one step manifesting intrinsic 1st order character of the phase transition. It has been suggested that conformational changes involve cooperative effects when the rearrangement of one butyl group can reduce the potential barriers for rearrangement of the neighboring butyl groups leading to the avalanche type spreading of the conformational changes across the whole crystal.[20] In some other cycles the transition between ultimate high and low electrical conductivity states happens in multiple steps which may be related to the expansion of the volume of conformational changes from. domain to domain across the crystal. It should be noted, that the 4-probe electrical measurements were conducted on

single crystals as compared to magnetic measurements conducted on the ensemble of thousands of crystals. As a result, the magnetic measurements always show relatively smooth transitions between LS and HS states with a width of change ΔT of ~5 K due to averaging over slightly different positions of hysteresis loop over thousands of individual crystals

While we have previously shown that substitution in radical conductors can increase the conductance of the material, here we see the opposite result. As can be seen in Figure 4.9, light substitution levels lower the conductance of both the low and high spin state. Once the solid solutions are heavily substituted they remain in their lower conductance, high spin state with no significant change of activation energy. This result confirms the importance of the paired electrons found in pancake bonding $[Bu]_2B$-$[Bu]_2B$ dimers for increasing of electrical conductivity.

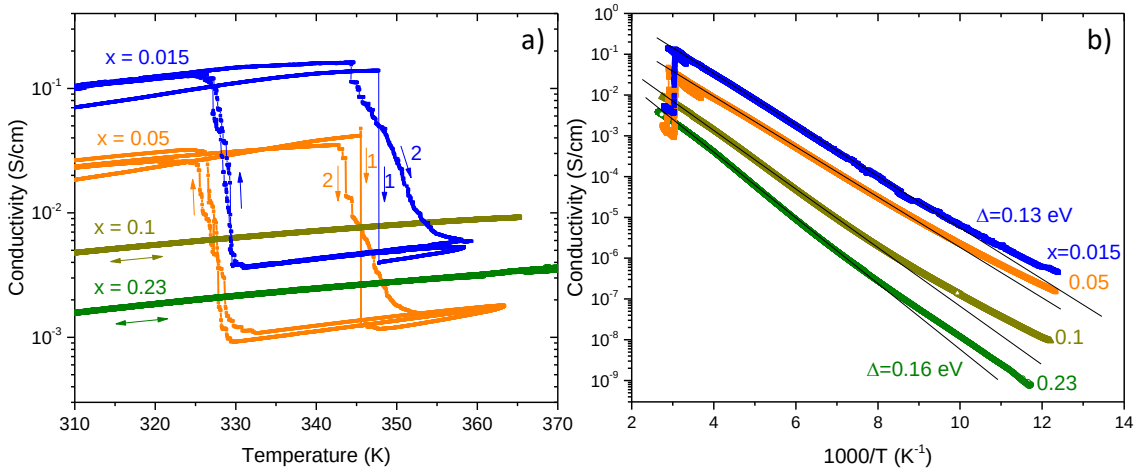

Figure 4.9: Conductivity of doped neutral radical conductors. (a) Zoomed in view of the transition showing a lowering of conductivity as doping is increased and an

eventual elimination of the hysteretic phase transition. (b) Arrhenius plot of temperature dependencies of electrical conductivity of various solid solutions of $[Bu]_2B_{1-x}Be_x$ in a wide temperature range.

4.8: Model of Substitutional Doping in $[Bu]_2B_{1-x}Be_x$

When taking the above data into account, a model of the effects of substituting $[Bu]_2B$ with $[Bu]_2Be$ can be envisioned. As summarized in Figure 4.10, a crystal of $[Bu]_2B$ is made up of pancake bonded $[Bu]_2B$-$[Bu]_2B$ pairs (Figure 4.10 (left, red)). When light substitution is done, the overlapped structure of $[Bu]_2B$ is retained with some pairs containing a single electron $[Bu]_2B$-$[Bu]_2Be$ pancake bond resulting in a larger spin per molecule value in the low spin state (Figure 4.10(left, yellow)). However, due to the presence of $[Bu]_2Be$ substitutes the coherence of the crystal structure may also be suppressed resulting in the decreasing size of the hysteresis loop to a higher degree than the percentage of introduced spinless $[Bu]_2Be$. At this stage there is still a sufficient amount of radicals to maintain the structure of pure $[Bu]_2B$. After the amount of substitution is increased, the solid solution assumes the crystal structure of $[Bu]_2Be$. At this point, even though the amount of radical has been reduced by just 6%, the dimers are no longer able to remain paired and the spins can be considered to be non-interacting (Figure 4.10 (right)). It is interesting to again note that a considerably small reduction in the available spin is able to alter the crystal structure to such a high degree.

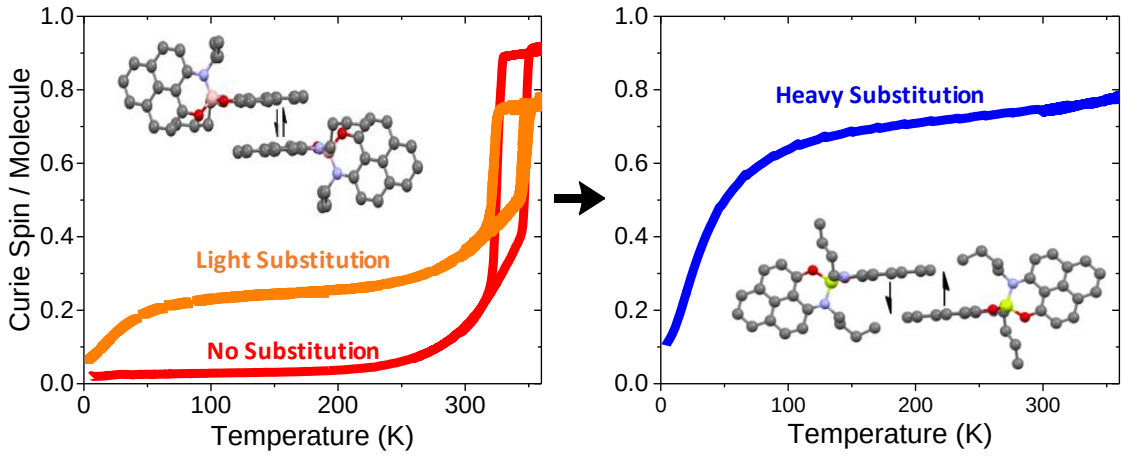

Figure 4.10: Effects of substitution on $[Bu]_2B_{1-x}Be_x$ solid solutions. (left) With no doping (red) dimers of $[Bu]_2B$ form 2 electron bonds canceling out their spin, at light substitution levels (yellow) some of these are now 1 electron bonds but the $[Bu]B_2$ structure is retained. (Right) At heavy substitution levels $[Bu]_2B_{1-x}Be_x$ adopts the structure of $[Bu]_2Be$ and the spins are non-interacting.

4.9: Conclusion

In conclusion, substitutional doping was applied to a bistable neutral organic radical conductor $[Bu]_2B$ by utilizing a non-radical containing molecular substitute $[Bu]_2Be$, and solid solutions of $[Bu]_2B_{1-x}Be_x$ were synthesized and characterized in terms of crystal structure and physical properties. It was observed that at the low doping level ($x < 0.06$) substituent $[Bu]_2Be$ molecules are incorporated in the crystal structure of the host $[Bu]_2B$ compound stabilized by phenalenyl-phenalenyl pancake bond formation. With increasing doping the hysteretic phase transition is gradually suppressed in terms of reducing the height, but conservation of the width of the hysteresis loop was observed through magnetic susceptibility and electrical conductivity measurements. At relatively low substitution level just above 6 percent the abrupt transformation of the crystal

structure to the one of pure $[Bu]_2Be$ crystal packing was observed in powder XRD measurements accompanied by a complete collapse of the hysteresis loop. Thus, in terms of crystal packing, these substituted organic radical conductors behave as binary systems, that is, they take the form of either the host or the substitute. It raises the possibility that one could modify an organic radical conductor with various substituents, with each substituent resulting in a different crystal structure and different properties, thus engineering one organic radical conductor into a multitude of structurally different compounds. A variety of such dopants can be bi-phenalenyl based molecules for better matching of the crystal lattice of the $[Bu]_2B$ host with an interesting case of $[Et]_2B$ dopant which shows a similar phase transition at lower temperature.[11] By studying that one organic radical conductor in its various crystal structures the structure-property relationships could be revealed, perhaps, providing valuable hints of how to design new bistable materials. Overall, this work demonstrates that the substitution technique often used to control the properties of inorganic materials can also be applied to bistable neutral radical organic conductors.

4.10: Experimental and Supplementary Information

Materials:

All reactions were done under a dry argon atmosphere using standard Schlenk and vacuum-line techniques. The reagents 1.0 M BCl_3 in hexane (Aldrich), $BeCl_2$ (Aldrich), tetrakis(dimethylamino)ethylene (TDAE, TCI America), potassium tetraphenylborate (Aldrich), cinnamoyl chloride (TCI America), 2-

methoxynaphthalene (Alfa Aesar), triethylamine (Aldrich), toluene (Aldrich) and dry acetonitrile (Aldrich) were used as received. $[Bu]_2B+ BPh_4-$ was synthesized according to literature procedures.[11] ESI mass spectra were recorded with an Agilent LCTOF (2006) instrument with APCI/ESI ionization. NMR Spectra were collected on a Bruker 300 spectrometer. Elemental analysis and inductively coupled plasma mass spectra (ICP-MS) of the $[Bu]B_{1-x}Be_x$ samples were performed at the Microanalysis Laboratory at the University of Illionis, Urbana-Champaign, IL.

Synthesis of $[Bu]_2Be$:

Synthesis of $[Bu]_2Be$ followed a modified literature procedure.[31] 9-N-butylamino-1-oxophenalene (1 mmol, 0.251 g) (synthesized by literature procedure)[11] and triethylamine (1.1 mmol, 0.101 g) were stirred in anhydrous Toluene (40 mL) in an argon atmosphere at 90 °C before adding $BeCl_2$ (0.5 mmol, 0.040 g). The reaction was allowed to stir overnight at 90 °C. The reaction was allowed to cool, and a yellow solid was filtered, washed with methanol and recrystallized from hot polyethylene carbonate. Yield 0.330 g (65%); mp > 350 °C; 1 H NMR (300 MHz, CD_3CN, 25 °C) δ 8.07 (2H, d) 8.00 (2H, d) 7.89 (2H, d) 7.87 (2H, d) 7.47 (2H, t) 7.29 (2H, d) 7.21 (2H, d) 3.48 (2H, m) 3.22 (2H, m) 1.61 (2H, m) 1.50 (2H, m) 1.13 (4H, m) 0.65 (6H, m) ppm; ESI-MS m/z calcd for $C_{34}H_{34}N_2O_2Be$ [M+] 511.2742, found 511.2741. Anal. Calcd (found) for $C_{34}H_{34}O_2N_2Be$: C, 79.80 (79.67); H, 6.70 (6.56); N 5.48 (5.41).

Crystallization of $[Bu]B_{1-x}Be_x$:

In an invertible H-cell with a medium porosity frit is loaded in a glove box. $[Bu]B_2$+ BPh_4- (1.15 x 10^{-4} mol, 100 mg) and $[Bu]_2Be$ (2.3 x 10^{-5} mol, 11.8 mg)are dissolved in 15 mL dry acetonitrile in a round bottom. In a separate round bottom ~0.2 mL TDAE is dissolved in 16 mL dry acetonitrile. The round bottom flasks are attached to the H-cell and the cell is inverted allowing the solutions to mix at the frit. After ~1 week black crystals have grown onto the frit. The sample is characterized by ICP analysis to find the solid solution composition ($[Bu]B_{0.87}Be_{0.13}$). Crystals of other compositions were grown using the same method, varying the amount of $[Bu]_2Be$ used.

X-Ray Crystallography:

CCDC 1874726 contains the supplementary crystallographic data for $[Bu]_2Be$. These data are provided free of charge by the Cambridge Crystallographic Data Centre. Structures of $[Bu]_2B$ are taken from the literature.[17]

Powder X-Ray Data:

Powder X-ray data of synthesized compounds were collected at room temperature in the 2Θ range 3-65 degrees using a Rigaku MiniFlex 600 diffractometer with Cu-Kα1 radiation (λ = 1.54059 Å), image plate detector and Ge monochromator. Silicon was used as standard. The diffractograms for host and substitute compounds are shown in Figure 4.11. The patterns match well with the calculated pattern obtained from the single crystal data. The unit cell parameters obtained from the single crystal data and powder X-ray diffraction are very close to each other. The obtained lattice parameters from the powder X-ray

diffraction peak matching are given below in Table 4.1. The lattice parameters obtained from powder X-ray diffraction peak matching are shown in Table 4.2.

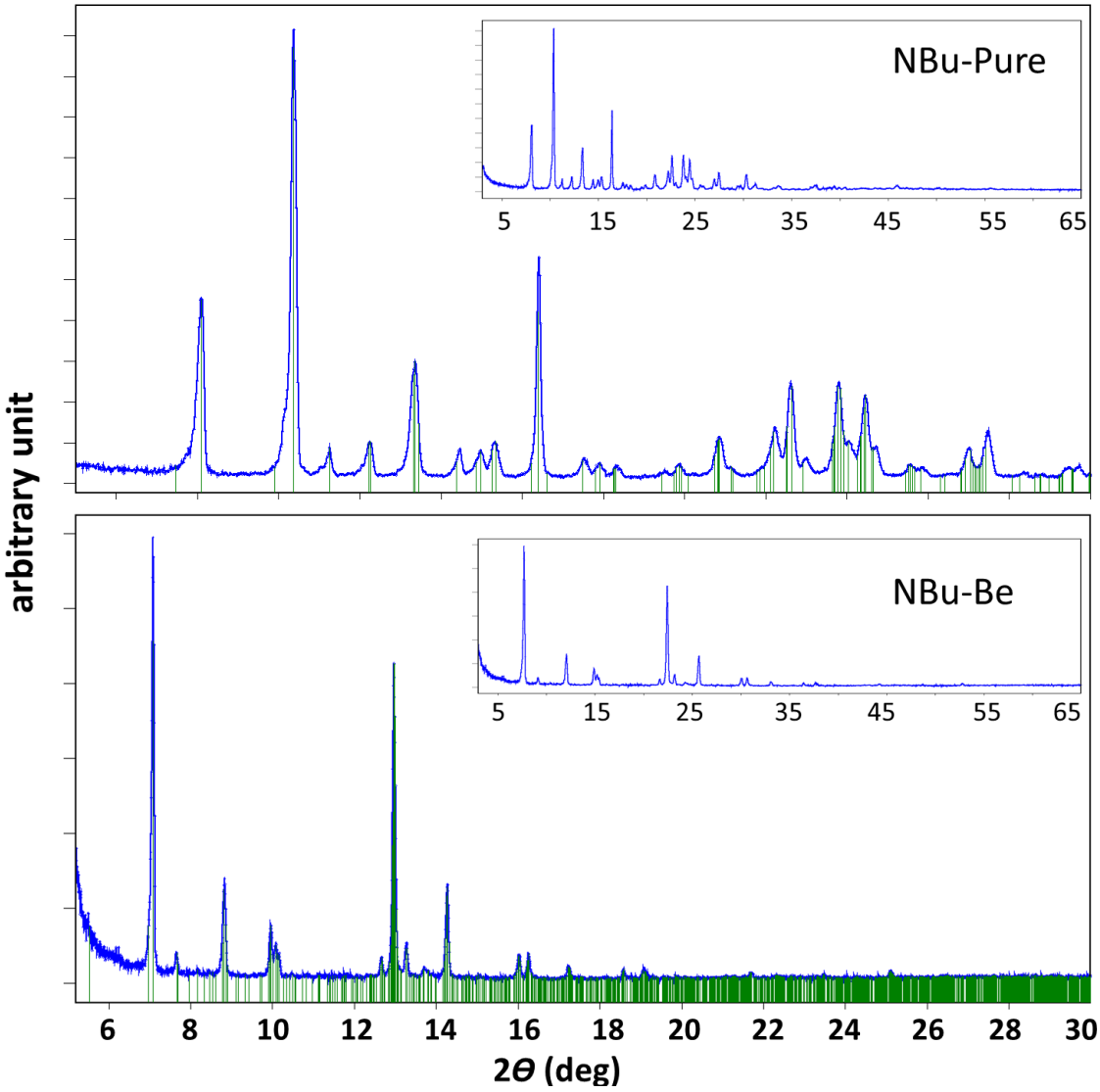

Figure 4.11: Powder X-ray diffraction patterns for the compounds $[Bu]_2B$ (top) and $[Bu]_2Be$ (bottom). The green vertical lines represent calculated peak positions for the respective compounds obtained from their single crystal data. The most prominent peaks were located below 2Θ = 30 degree and hence the peak matching was performed only upto 2Θ = 30 degree. The full diffraction patterns (in the range 2Θ = 3-65 degrees are shown in insets).

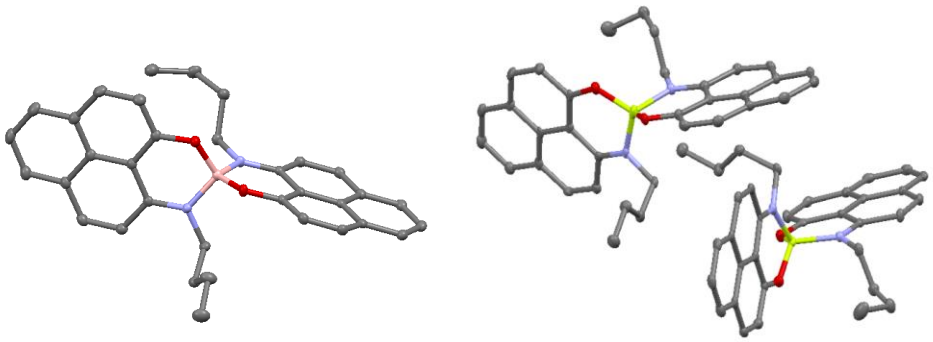

Figure 4.12: Thermal ellipsoids of (left) $[Bu]_2B$ and (right) $[Bu]_2Be$.

Table 4.1: X-ray crystallographic data of $[Bu]_2Be$ and $[Bu]_2B$ (100K and 360K). $[Bu]_2B$ data taken from literature.

Compound	$[Bu]_2Be$	$[Bu]_2B$ (100 K)	$[Bu]_2B$ (360 K)
Empirical formula	C34 H32 Be N2 O2	C34 H32 B N2 O2	C34 H32 B N2 O2
Formula weight (g/mol)	509.62	511.44	511.44
Temperature (K)	100	100	360
Crystal system	Triclinic	Monoclinic	Monoclinic
Space group	*P*-1	*P* 21/c	*P* 21/*c*
a (Å)	9.0726	8.9362	9.076
b (Å)	12.4697	12.1541	12.584
c (Å)	23.703	23.537	24.054
α (deg)	75.239	90.00	90.00
β (deg)	83.744	100.913	96.268
γ (deg)	78.024	90.00	90.00
V Å^3	2532.2	2510.16	2730.84
Z	4	4	4

Table 4.2. Lattice parameters obtained from powder X-ray diffraction peak matching.

Compound	**$[Bu]_2B$**	**$[Bu]_2Be$**
Space group	P 2_1/c (no. 14)	P -1 (no. 2)
a (Å)	9.084	9.096
b (Å)	12.315	12.557
c (Å)	24.062	23.930
α (degrees)	-	74.678
β (degrees)	100.497	83.856
γ (degrees)	-	79.172

Conductivity Measurements:

Single crystal temperature dependent four-probe electrical conductivity measurements were conducted utilizing EverCool-II cryogen-free upgraded version of the Physical Property Measurement System (PPMS, Quantum Design) with-in house made insert for high resistance measurements. The neutral radical crystals were positioned free on a sapphire substrate, and in-line contacts were made with silver paint and four flexible 25 μm diameter platinum wires. This flexible design allowed to reduce the mechanical stress on the crystals associated with a mismatch of thermal expansions of the crystal and the substrate. A Keithley 236 unit and two 6517 Keithley electrometers were used as a current source and two potential probes, respectively, and the resistance vs temperature data were acquired utilizing LabVIEW software.

Magnetic Susceptibility Measurements

Magnetic measurements of ~15 mg powdered samples were measured with a vibrating sample magnetometer in an EverCool-II PPMS system in a 1 Tesla magnetic field from 4K to 360K.

4.11: References:

1) Shao, Z. W.; Cao, X.; Luo, H. J.; Jin, P. *NPG Asia Mater.* **2018**, *10*.

2) Peng, Z. F.; Jiang, W.; Liu, H. *J. Phys. Chem. C* **2007**, *111*, 1119.

3) Wu, Z. P.; Miyashita, A.; Yamamoto, S.; Abe, H.; Nashiyama, I.; Narumi, K.; Naramoto, H. *J. Appl. Phys.* **1999**, *86*, 5311.

4) Burkhardt, W.; Christmann, T.; Franke, S.; Kriegseis, W.; Meister, D.; Meyer, B. K.; Niessner, W.; Schalch, D.; Scharmann, A. *Thin Solid Films* **2002**, *402*, 226.

5) Soltani, M.; Chaker, M.; Haddad, E.; Kruzelecky, R. V.; Margot, J. *Appl. Phys. Lett.* **2004**, *85*, 1958.

6) Peng, Z. F.; Wang, Y.; Du, Y. Y.; Lu, D.; Sun, D. Z. *J. Alloys Compd.* **2009**, *480*, 537.

7) Manning, T. D.; Parkin, I. P.; Pemble, M. E.; Sheel, D.; Vernardou, D. *Chem. Mater.* **2004**, *16*, 744.

8) Han, Y. H.; Choi, I. H.; Kang, H. K.; Park, J. Y.; Kim, K. T.; Shin, H. J.; Moon, S. *Thin Solid Films* **2003**, *425*, 260.

9) Rogalski, A. *Infrared Detectors*; 2 ed.; CRS Press: Boca Raton, Fl, USA, 2011.

10) Wang, B.; Lai, J. J.; Li, H.; Hu, H. M.; Chen, S. H. *Infrared Phys. Technol.* **2013**, *57*, 8.

11) Chi, X.; Itkis, M. E.; Kirschbaum, K.; Pinkerton, A. A.; Oakley, R. T.; Cordes, A. W.; Haddon, R. C. *J. Am. Chem. Soc.* **2001**, *123*, 4041.

12) Fujita, W.; Awaga, K. *Science* **1999**, *286*, 261.

13) Lekin, K.; Winter, S. M.; Downie, L. E.; Bao, X.; Tse, J. S.; Desgreniers, S.; Secco, R. A.; Dube, P. A.; Oakley, R. T. *J. Am. Chem. Soc.* **2010**, *132*, 16212

14) Brusso, J. L.; Clements, O. P.; Haddon, R. C.; Itkis, M. E.; Leitch, A. A.; Oakley, R. T.; Reed, R. W.; Richardson, J. F. *J. Am. Chem. Soc.* **2004**, *126*, 8256.

15) Hoshino, N.; Iijima, F.; Newton, G. N.; Yoshida, N.; Shiga, T.; Nojiri, H.; Nakao, A.; Kumai, R.; Murakami, Y.; Oshio, H. *Nat. Chem.* **2012**, *4*, 921.

16) Mitsumi, M.; Nishitani, T.; Yamasaki, S.; Shimada, N.; Komatsu, Y.; Toriumi, K.; Kitagawa, Y.; Okumura, M.; Miyazaki, Y.; Gorska, N.; Inaba, A.; Kanda, A.; Hanasaki, N. *J. Am. Chem. Soc.* **2014**, *136*, 7026.

17) Pal, S. K.; Bag, P.; Sarkar, A.; Chi, X. L.; Itkis, M. E.; Tham, F. S.; Donnadieu, B.; Haddon, R. C. *J. Am. Chem. Soc.* **2010**, *132*, 17258.

18) Itkis, M. E.; Chi, X.; Cordes, A. W.; Haddon, R. C. *Science* **2002**, *296*, 1443.

19) Huang, J.; Kertesz, M. *J. Am. Chem. Soc.* **2003**, *125*, 13334.

20) Fumanal, M.; Novoa, J. J.; Ribas-Arino, J. *Chem. Eur. J.* **2017**, *23*, 7772.

21) Jorge, G. A.; Kim, K. H.; Jaime, M.; Chi, X.; Hellman, F.; Itkis, M. E.; Mandal, S. K.; Haddon, R. C. *AIP Conf. Proceedings* **2006**, *850*, 1315.

22) Fumanal, M.; Mota, F.; Novoa, J. J.; Ribas-Arino, J. *J. Am. Chem. Soc.* **2015**, *137*, 12843.

23) Taniguchi, T.; Kawakami, T.; Yamaguchi, K. *Polyhedron* **2005**, *24*, 2274.

24) Huang, J. S.; Kertesz, M. *J. Phys. Chem. A* **2007**, *111*, 6304.

25) Bag, P.; Itkis, M. E.; Stekovic, D.; Pal, S. K.; Tham, F. S.; Haddon, R. C. *J. Am. Chem. Soc.* **2015**, *137*, 10000

26) Pal, S. K.; Bag, P.; Itkis, M. E.; Tham, F. S.; Haddon, R. C. *J. Am. Chem. Soc.* **2014**, *136*, 14738.

27) Cui, Z. H.; Lischka, H.; Beneberu, H. Z.; Kertesz, M. *J. Am. Chem. Soc.* **2014**, *136*, 12958.

28) Cui, Z.; Lischka, H.; Beneberu, H. Z.; Kertesz, M. *J. Am. Chem. Soc.* **2014**, *136*, 5539

29) Suzuki, S.; Morita, Y.; Fukui, K.; Sato, K.; Shiomi, D.; Takui, T.; Nakasuji, K. *J. Am. Chem. Soc.* **2006**, *128*, 2530

30) Chi, X.; Itkis, M. E.; Patrick, B. O.; Barclay, T. M.; Reed, R. W.; Oakley, R. T.; Cordes, A. W.; Haddon, R. C. *J. Am. Chem. Soc.* **1999**, *121*, 10395.

31) Haddon, R. C.; Chichester, S. V.; Marshall, J. H. *Tetrahedron* **1986**, *42*, 6293.

Chapter 5: Towards Energy Matched Substitutional Doping

5.1: Introduction

While Chapters 3 and 4 showed that substitutional doping in phenalenyl based neutral radical conductors can be an effective way of modulating their properties, there were still some limitations.[1,2] Compared to silicon, which can be doped to a metallic state, the increases of conductivity seen in Chapter 3 are relatively small. As discussed in Chapter 1, an effective substitutional dopant must both be able to be incorporated into the crystal structure of the host and be electronically comparable to the host. While the crystal structures of our previous dopant were quite different than that of the host, we have shown that the host is able to incorporate at least a limited range of dopant without large changes in the crystal structure. The second requirement, that of comparable electronic properties in order to facilitate charge transfer, has yet to be solved.

As shown in Chapter 3, the energy levels of the SOMO of host, $[5\text{-Me}]_2$B, and the LUMO of the dopant, $[5\text{-Me}]_2$Be, were greater than 1 V apart according to the cyclic voltammogram data.[1] To remedy this, a dopant with a lower lying LUMO was envisioned. While adding substituents to the perimeter of an aromatic system has been known to affect the energy levels, previous phenalenyl based neutral radicals have shown this as a poor direction. The reason is that the substituents interfere with the interfacial PLY-PLY interactions which have been shown to play an important role in the conducting pathways.[3] Thus, to lower the LUMO of the dopant without interfering with the interfacial interactions, a dopant

in which two of the carbons are replaced with two more electronegative nitrogen atoms was suggested. The proposed compound, 4,6-N,N-9-hydroxy-phenalenone (DZPLY) and its beryllium complex ([DZPLY]$_2$Be) is pictured in Figure 5.1. This Chapter discusses the realization of the proposed concept.

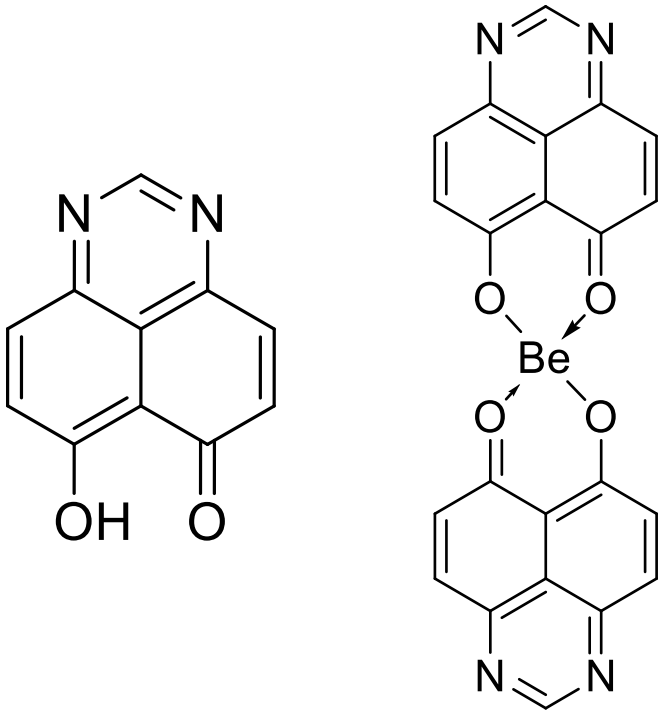

Figure 5.1: Structure of (left) DZPLY and its beryllium complex, (right) [DZPLY]$_2$Be.

5.2: Synthesis of [DZPLY]$_2$Be

With its 1,3-diazine motif, DZPLY is reminiscent of pyrimidines. Pyrimidines can be synthesized from 1,3 diketones and amidines as pictured in Scheme 5.1 (top).[4] With reported synthesis of naphthazarin (5,8-dihydroxy-1,4-naphthoquinone), a simple retrosynthesis was envisioned (Scheme 5.1, bottom). However, reaction of naphthazarin with various amidines resulted in complex

mixtures and no sign of the desired product. This was ascribed to the reactivity of beta carbons in naphthazarin towards nucleophiles.

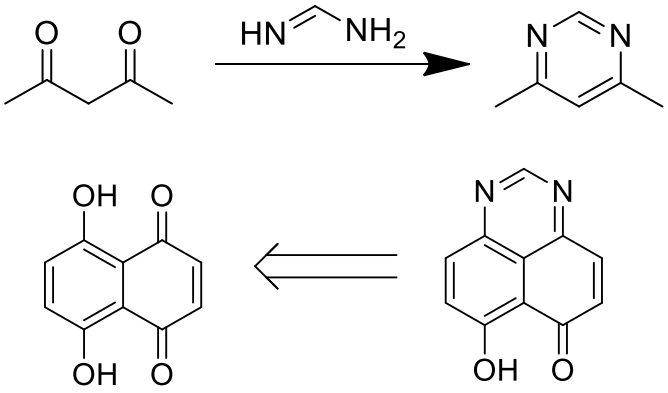

Scheme 5.1: (top) Synthesis of pyrimidines from 1,3-diketones and amidines. (bottom) Proposed retrosynthesis of DZPLY from naphthazarin.

To circumvent this issue, an amine substituted naphthazarin derivative, 5-amino-8-hydroxy-,4-naphthoquinone (amino-naphthazarin), was envisioned to act as the nucleophilic component thus avoiding the issue of reactivity at the beta carbons. Amino-naphthazarin was synthesized from a modified literature procedure.[5,6] From here, amino-naphthazarin is reacted with formamide in acetic acid to give DZPLY.[7] This is then reacted with beryllium acetylacetonate to give the target on interest, $[DZPLY]_2Be$ as shown in Scheme 5.2.

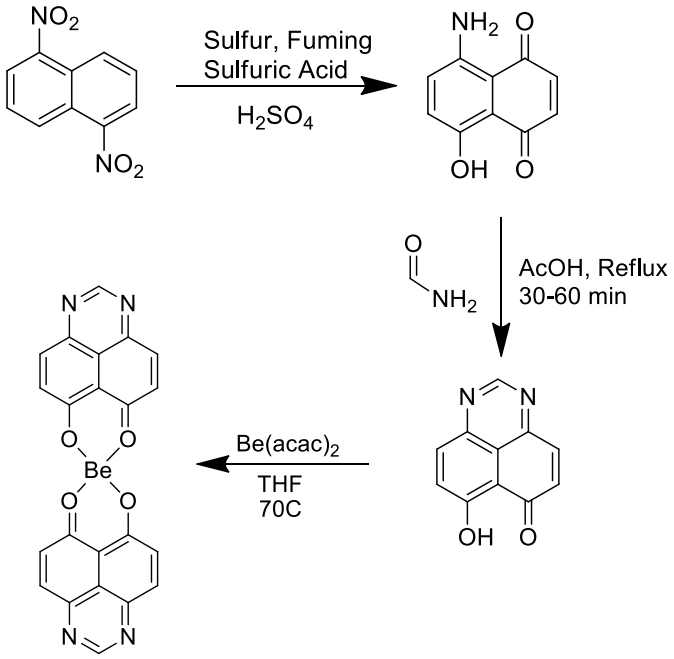

Scheme 5.2: Synthesis of $[DZPLY]_2Be$ from 1,5-dinitronaphthalene. 1,5-dinitronaphthalene is reacted with fuming sulfuric acid and elemental sulfur to produce amino-naphthazarin. Amino-naphthazarin is then reacted with formamide in acetic acid to form DZPLY which is then reacted with beryllium acetylacetonate to give the final product, $[DZPLY]_2Be$.

5.3: Reactivity of DZPLY

The chemical reactivity of DZPLY was also explored and found to be significantly different than that of PLY. Complexation of DZPLY with boron in order to create radicals of $[DZPLY]_2B$ was unsuccessful, possibly due to the aromatic nitrogen atoms. Chelation to beryllium using beryllium chloride (as done with 9-amino-phenalenone derivatives) was also unsuccessful. The desired beryllium complex was only formed through the use of beryllium acetylacetonate (Scheme 5.2).

9-amino substituted derivatives of DZPLY were also explored. To synthesize 9-amino derivatives of PLY, 9-hydroxy-phenalenone is stirred in a

solvent of the substituted amine at reflux overnight, and only the product is observed. DZPLY was found to be much more reactive and stirring in solvent with 2-3 equivalents of substituted amine at room temperature over the course of a few hours resulted in the formation of 3 new products. Those products are indicated by 3 new peaks around 9 ppm in the NMR spectra corresponding to the aromatic hydrogen on the carbon in-between the two nitrogen atoms. Analysis found 3 distinct products; two with masses of 324 g/mol, and one with a mass of 253 g/mol. Figure 5.2a shows the NMR spectra of the three Products. Fraction 2 was ascribed to the targeted product (Figure 5.2b) due to the upfield singlet and 4 pairs of aromatic doublets (one obscured by $CHCl_3$ peak) and correct mass of 253 g/mol. Due to matching masses, the appearance of two butyl chains in the NMR from 0-4 ppm, and consistent splitting as expected from the ring (1 singlet around 9 ppm, 2 doublets, 1 lower shifted singlet) the structures of fraction 1 and 3 were ascribed to that shown in Figure 5.2c. Here, one R group is a butylamine and the others are hydrogens (note: peaks around 3.5 ppm belong to the butyl chain and are doublets of triplets, consistent with the literature).[8] Further exploration to determine the exact structures was not performed. Chelation of the derivatives to boron and beryllium were unsuccessfully attempted, but not heavily studied.

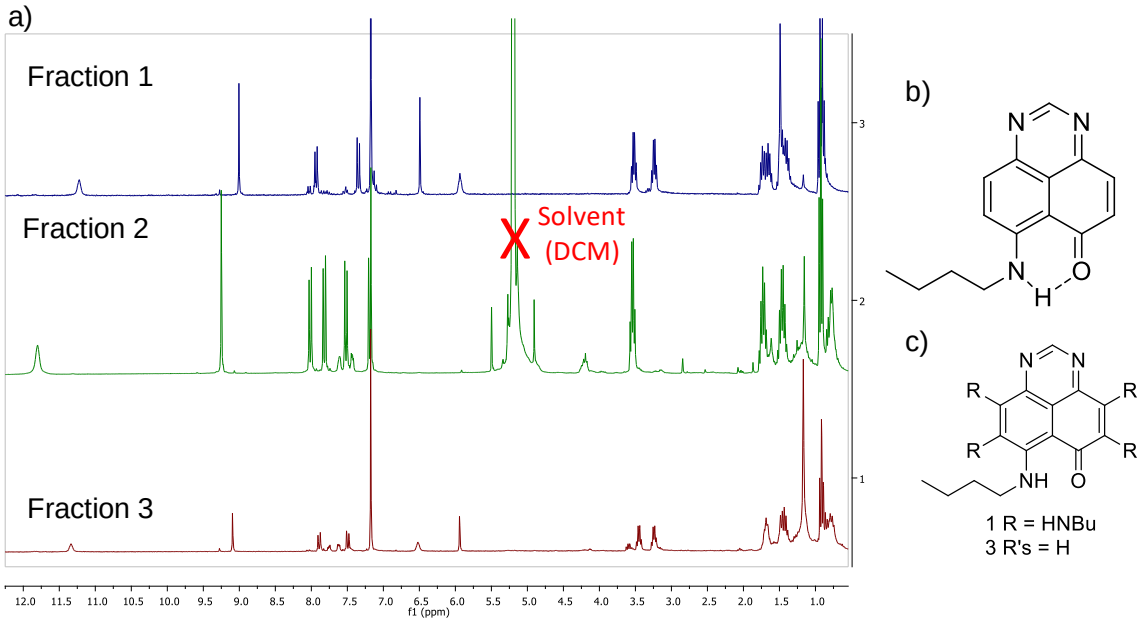

Figure 5.2: (a) NMR spectra of the three products from the reaction of DZPLY and butylamine. (b) Proposed structure of the targeted compound. (c) Proposed structure of the other two products.

Overall DZPLY was found to be more difficult to chelate, and more reactive than PLY, most likely due to the addition of the aromatic nitrogen atoms.

5.4: Electrochemical Properties of $[DZPLY]_2Be$

With the newly synthesized dopant in hand, its electrochemical properties were investigated to determine its suitability. Figure 5.3 shows the differential cyclic voltammetry of the original non-nitrogen containing host radical and dopant[2] along with the pulse voltammetry (DPV) of $[DZPLY]_2Be$ (DPV was chosen over CV as the compound is not very soluble in acetonitrile).

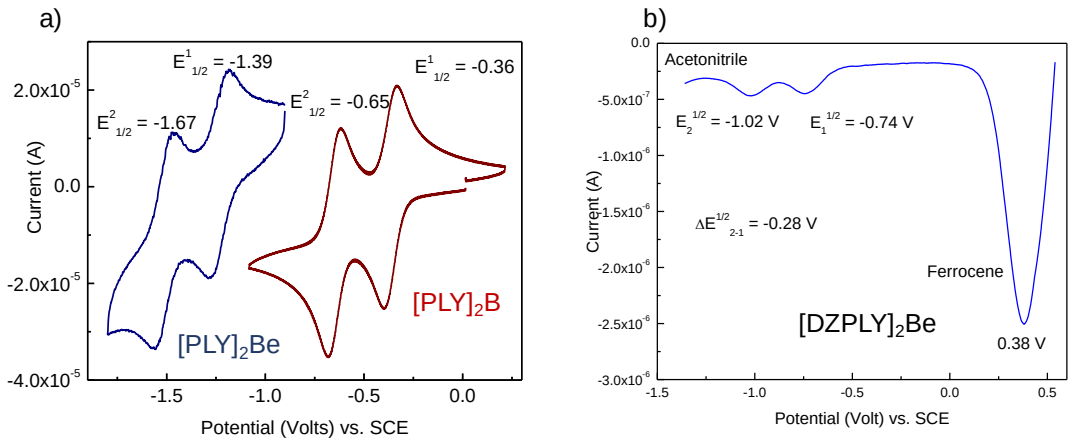

Figure 5.3: (a) CV of $[PLY]_2B$ and $[PLY]_2Be$.[2] (b) Differential pulse voltammetry of $[DZPLY]_2Be$.

From the voltammograms, it can be seen that $[DZPLY]_2Be$ reduces to its radical anion at -0.74 V and to its dianion at -1.02 V (vs SCE). Compared to the respective reduction potentials of -1.39 V and -1.67 V this represents about a 1 V shift towards zero. The potential of the reaction of interest, radical moving from host to dopant, is also reduced from 1.03 V to 0.38 V (summarized in Figure 5.4). While this energy gap is still large compared to the energy gaps found in doped silicon, it is still a significant improvement.

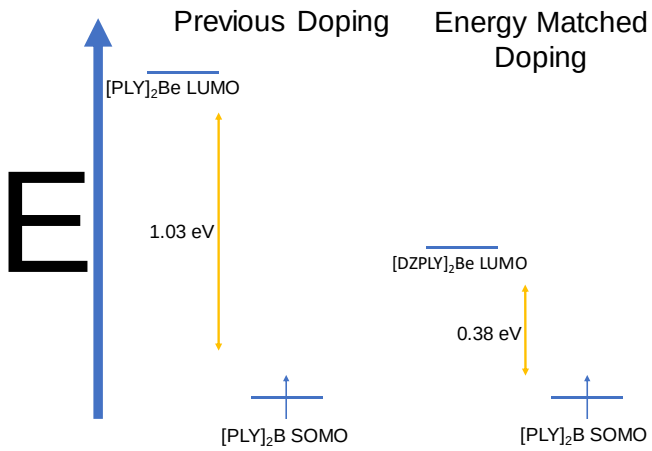

Figure 5.4: Energy differences in the SOMO to LUMO transition of the previous dopant and the new, energy matched dopant.

5.5: Structure of $[DZPLY]_2Be$

With the electrochemistry of the new dopant showing an improvement, the physical packing structure of the $[DZPLY]_2Be$ was also examined. Figure 5.5 shows the structure of a single molecule of radical $[PLY]_2B$ and dopants $[PLY]_2Be$[2] and $[DZPLY]_2Be$. Both $[PLY]_2B$ and $[PLY]_2Be$ pack in a C2/c space group and contain half a molecule in the asymmetric unit while $[DZPLY]_2Be$ packs ins in a $P2_1/c$ space group with an entire molecule in the asymmetric unit. $[DZPLY]_2Be$ also shows a bend in the interplanar angle between the two DZPLY units as can be seen in Figure 5.5. Finally, as would be expected, the C-N bonds in $[DZPLY]_2Be$ are shorter (~1.35 Å) than the C-C bonds (~1.40 Å) in the non-nitrogen containing molecules.

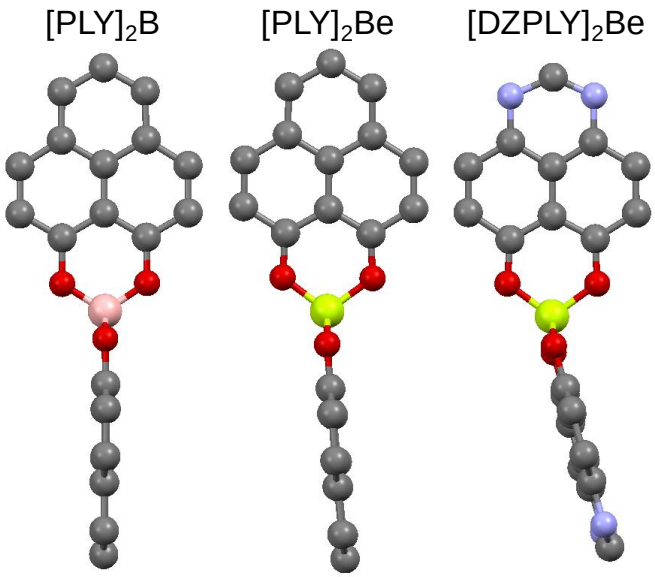

Figure 5.5: Structure of molecules of the radical $[PLY]_2B$ and dopants $[PLY]_2Be$ and $[DZPLY]_2Be$.

The intermolecular interactions found in the crystal structure of $[DZPLY]_2Be$ are also quite different. As can be seen in Figure 5.6 both radical $[PLY]_2B$ and dopant $[PLY]_2Be$ form 1-D chains. The main difference between the host and dopant are the interfacial distance (3.18 Å for radical and 3.40 Å for dopant) and the interchain distances (3.38 Å for radical and 5.15 Å for dopant).[2] In contrast, $[DZPLY]_2Be$ packs as dimers with one PLY-PLY interfacial interaction (3.35 Å) and the other PLYs containing no interfacial interactions.

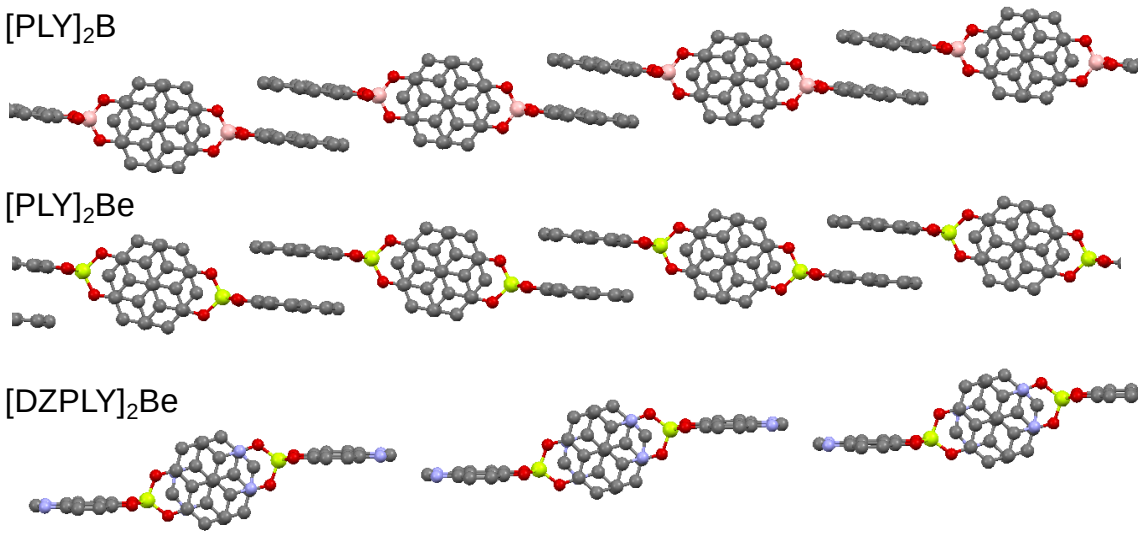

Figure 5.6: 1-D chains found in the crystal structure of $[PLY]_2B$ and $[PLY]_2Be$ and the dimers found in $[DZPLY]_2Be$.

The interfacial interactions are shown in Figure 5.7 in which the spin bearing carbons are colored green (note: nitrogen atoms are not colored green but would still be spin-bearing). All three molecules show good overlap with $[DZPLY]_2Be$ showing the worst overlap. As a reminder, $[PLY]_2B$ and $[PLY]_2Be$ have the same interactions on both PLYs of the molecules while $[DZPLY]_2Be$ only shows interfacial overlap on one DZPLY unit.

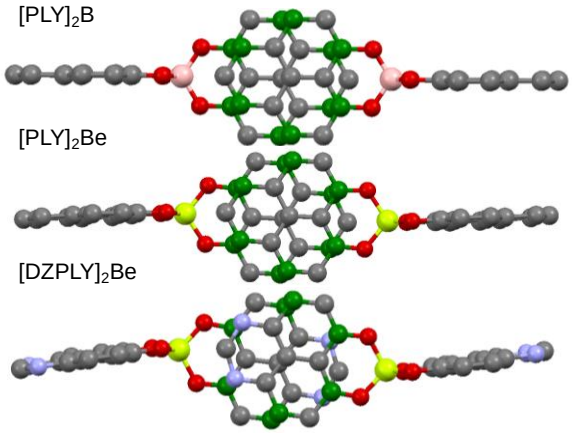

Figure 5.7: Interfacial overlap in radical $[PLY]_2B$ and dopants $[PLY]_2Be$ and $[DZPLY]_2Be$.

While $[DZPLY]_2Be$ shows significant differences in crystal structure than the radical $[PLY]_2B$, it still contains one good interfacial interaction and, as we had shown in Chapters 3 and 4, host radicals can incorporate at least a limited range of dopant concentrations in their structure before the changes become drastic.

5.6: Substitutional Doping with $[DZPLY]_2Be$

Growth of solid solutions containing $[DZPLY]_2Be$ proved to be extremely difficult. The insolubility of $[DZPLY]_2Be$ in most solvents proved a significant barrier. Figure 5.8 shows a few pictures of some of the (very) many crystals grown containing radical $[PLY]_2B$ doped with $[DZPLY]_2Be$. While previous pure and doped radicals display flat, smooth surfaces, those doped with $[DZPLY]_2Be$ become very jagged and rough. While some very large crystals were grown (>3 mm) their quality is very poor and appear to multi-crystalline (can be especially

seen in bottom left picture). Attempts at using other radicals proved unsuccessful.

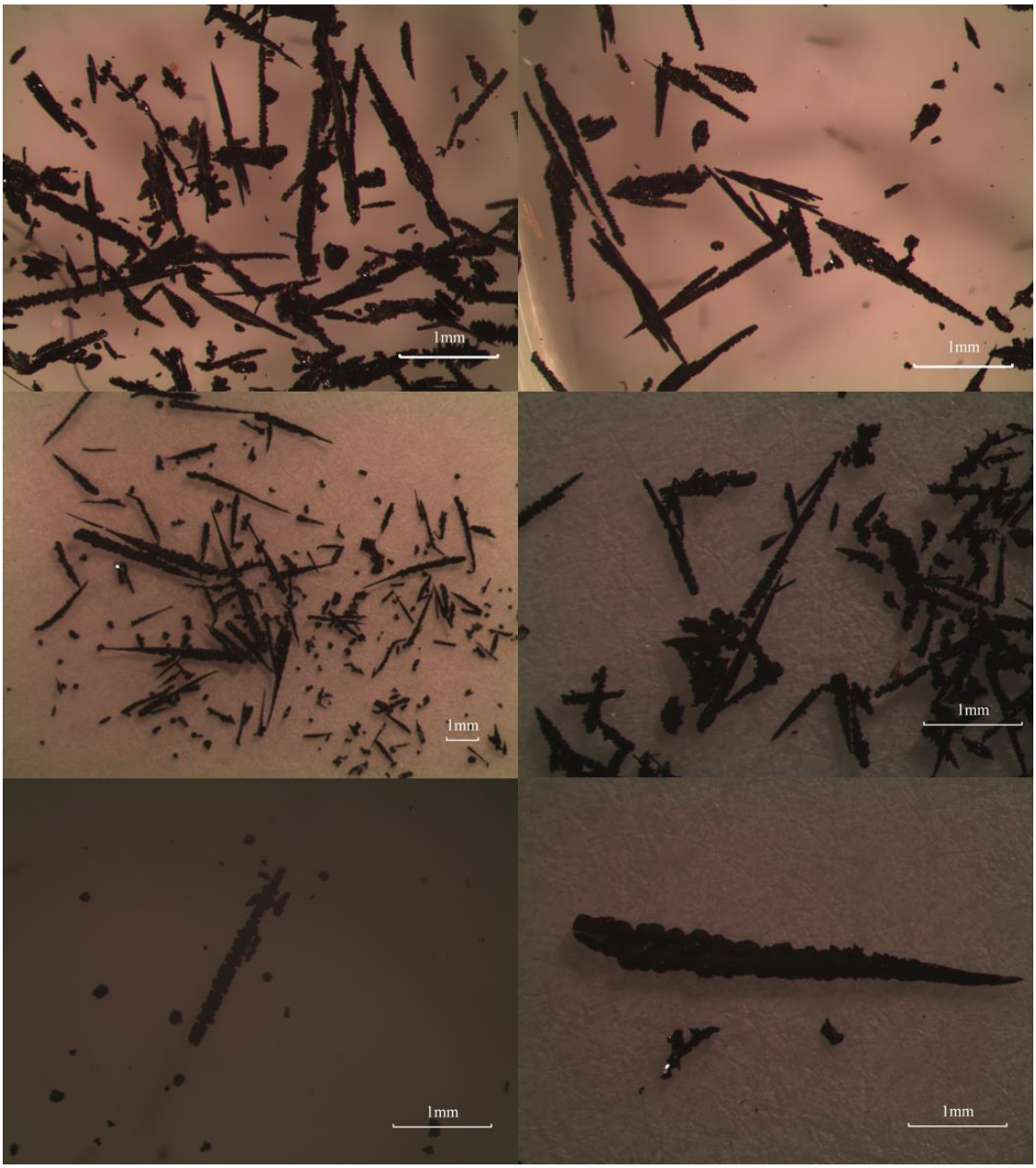

Figure 5.8: Pictures of $[PLY]_2B$ doped with $[DZPLY]_2Be$.

Figure 5.9 shows some four probe electrical conductivity measurements on doped systems along with a picture of a crystal wired for measurement (inset). As can be seen the doped compounds either display a lower conductivity or no change in conductivity from the original $[PLY]_2B$ radical. Whether this poor conductivity is due to the doping of the radical or the resultant poor crystal morphology is uncertain.

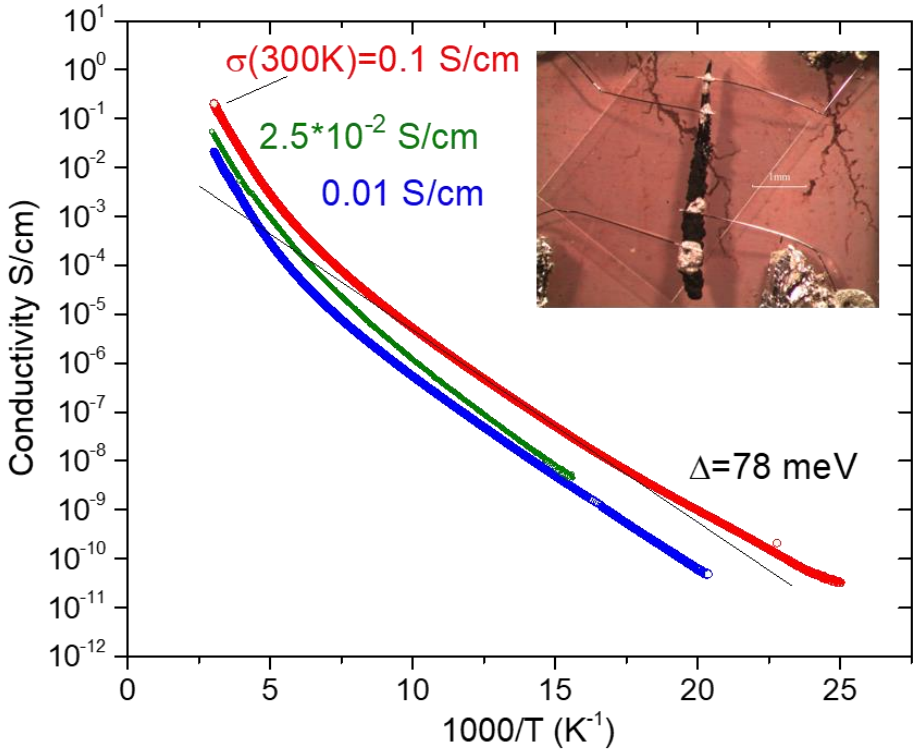

Figure 5.9: Conductivity measurements of doped crystals and (inset) a picture of a crystal wired for measurement.

5.7: Conclusion

In conclusion, an energy matched dopant, $[DZPLY]_2Be$ was synthesized and characterized. The dopant was shown to possess a different structure that contains a dimeric motif but still has an interfacial interaction. The dopant was also found to be a better match electrochemically due to the electronegative nitrogen atoms placed within the molecule. Unfortunately, solid solutions grown with this dopant were of poor crystal quality and show no improvement of electrical conductivity.

5.8: Experimental and Supplementary Information

5-amino-8-hydroxy-1,4-naphthoquinone (amino-naphthazarin):

5-amino-8-hydroxy-1,4-napthoquinone was synthesized by a modified literature procedure.[5] In a 500 mL round bottom equipped with a large stir bar, 1,5-dinitronaphthalene is added (20 grams, 92 mmol). Concentrated H_2SO_4 (75 mL) is slowly added. In a separate beaker, oleum (85 mL) is mixed with elemental sulfur (10g, 313 mmol). The oleum/sulfur mixture is slowly added to the round bottom over the course of ~1 hour while stirring. The reaction mixture is heated overnight at 65° C with stirring. The reaction mixture is poured into a large (2L beaker) containing ice and diluted using dH_2O to 1.5 L. The mixture is filtered through celite and extracted using dichloromethane using a liquid-liquid extractor. The solvent is removed through rotary evaporation to yield 5.5 g (28 %) of a solid purple powder. ^1H NMR (300 MHz, DMSO-d_6) δ 13.56 (1H, broad) 7.25 (1H, d) 7.15 (1H, d) 6.92 (2H, s) ppm.

4,6-N,N-9-Hydroxy-Phenalenone (DZPLY):

DZPLY was synthesized by a modified literature procedure.[7] To a 500 mL round bottom equipped with a large stir bar, acetic acid (250 mL) is stirred and heated to a heavy reflux. Amino-naphthazarin is added (1g, 10.5 mmol). Over the course of ~45 min excess formamide (~25 g, .56 mol) is added in ~5 mL portions. The reaction is monitored through thin layer chromatography as a slow-moving yellow (pdt) band forms. The reaction is removed from heat and diluted to ~ 0.5 L using dH_2O. The reaction is filtered and extracted using dichloromethane. Upon rotary evaporation a dark solid is given. A yellow solid is recovered after column chromatography on silica gel basified by triethylamine (1% triethylamine, 1% Methanol/Chloroform up to 5% Methanol/chloroform). Yield 0.40 g (38%); 1H NMR (300 MHz, $CDCl_3$) δ 14.40 (1H, broad) 9.56 (1H, s) 8.17 (2H, d) 7.47 (2H, d). ESI-MS m/z calcd for $C_{11}H_6N_2O_2$ [M+H] 199.050, found: 199.05.

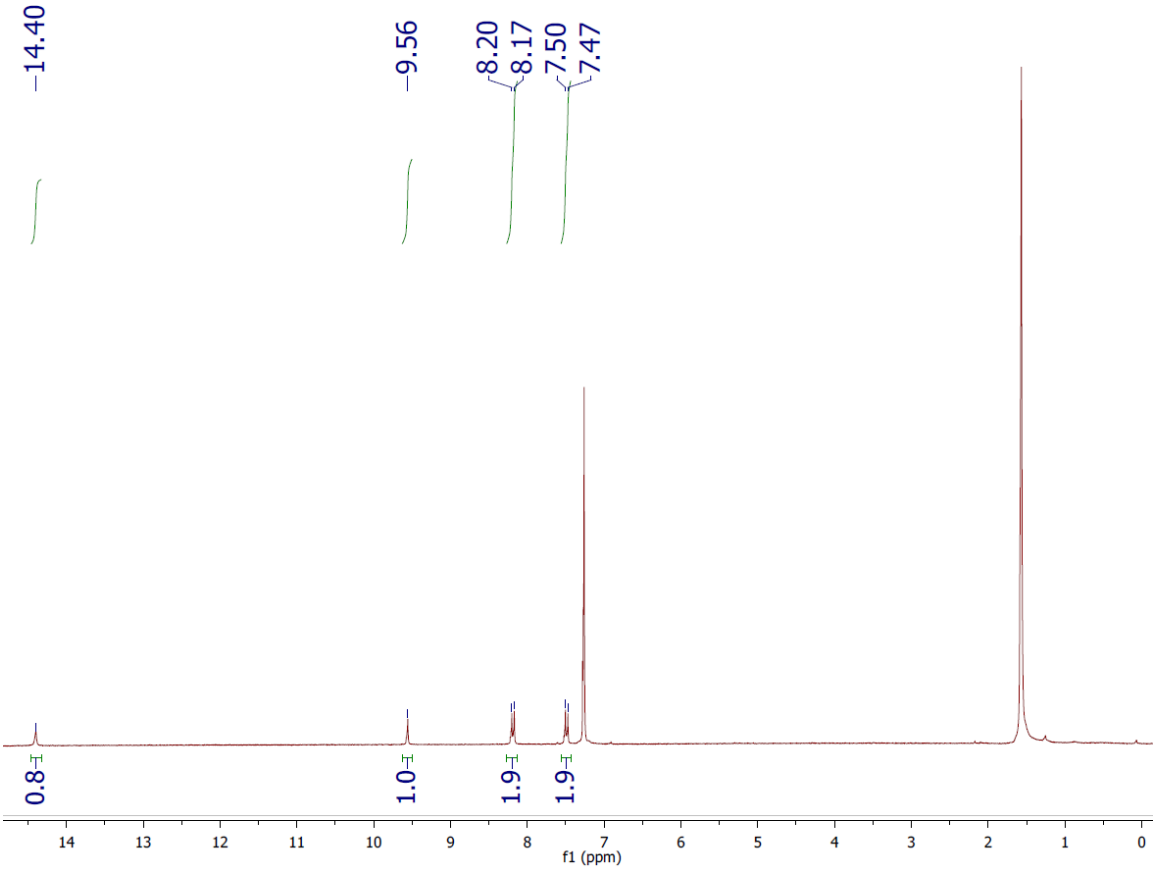

[DZPLY]$_2$Be:

In a 50 mL round bottom equipped with a small stir bar, 30 mL acetonitrile and DZPLY (200 mg, 1 mmol) are added and stirred. The reaction is heated to 80 °C and 2 eq. of Be(acac)$_2$ (414 mg, 2 mmol) are added and the reaction is left to stir overnight. The reaction is filtered, and the solid green precipitate is recrystallized from a DCM/MeOH mixture to give dark green crystals. Yield 120 mg (60 %); 1H NMR (300 MHz, $CDCl_3$) δ 9.61 (1H, S) 8.29 (2H, d) 7.53 (2H, d). ESI-MS m/z calcd for $C_{22}H_{120}N_4O_4Be$ [M+H] 404.3588, found: 404.36.

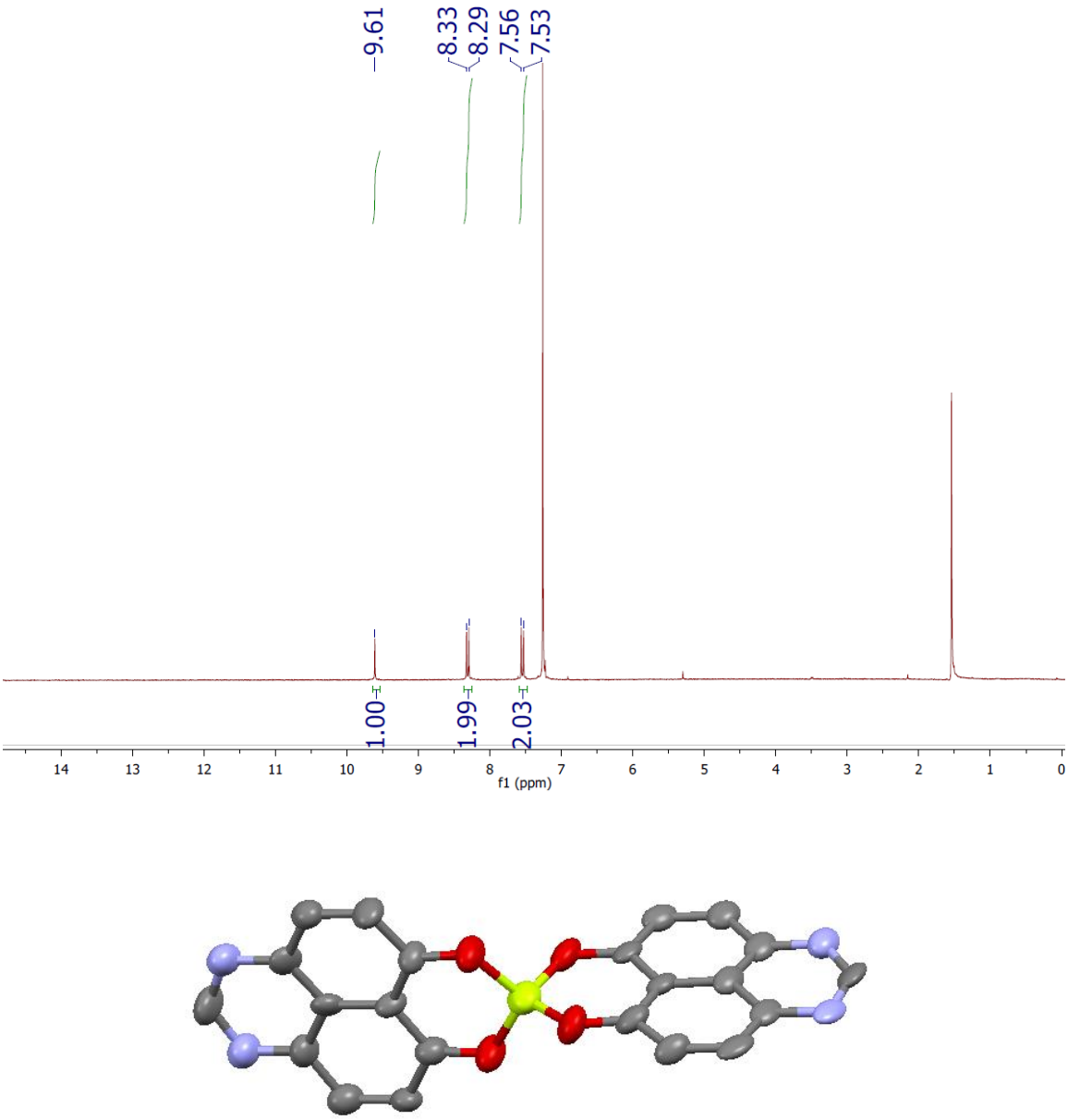

Figure 5.10: Thermal ellipsoids of $[DZPLY]_2Be$

Table 5.1: X-ray crystallographic data of $[DZPLY]_2Be$.

Compound	$[DZPLY]_2Be$
Empirical formula	C28 H19 O4 B
Formula weight (g/mol)	430.26
Temperature (K)	100
Crystal system	Monoclinic
Space group	$P\text{-}2_1/c$
Unit cell dimensions	
a (Å)	15.438
b (Å)	13.076
c (Å)	8.505
α (deg)	90
β (deg)	101.339
γ (deg)	90
V Å^3	1683.37
Z	4

Reaction of DZPLY and Butylamine:

In a 25 mL round bottom equipped with a magnetic stir bar, DZPLY (100 mg, 0.2 mmol) and n-butylamine (156mg, 0.6 mmol) are added and allowed to stir for ~6 hours. The solvent is removed via rotary evaporation and purified by column chromatography (alumina, dichloromethane eluent) to give 3 fractions (1st fraction mass 324 g/mol, 2nd fraction mas 254 g/mol, 3rd fraction mass 324).

5.9: References

1) Bag, P.; Itkis, M. E.; Stekovic, D.; Pal, S. K.; Tham, F. S.; Haddon, R. C. *J. Am. Chem. Soc.* **2015**, *137*, 10000

2) Pal, S. K.; Bag, P.; Itkis, M. E.; Tham, F. S.; Haddon, R. C. *J. Am. Chem. Soc.* **2014**, *136*, 14738.

3) Sarkar, A.; Pal, S. K.; Itkis, M. E.; Liao, P.; Tham, F. S.; Donnadieu, B.; Haddon, R. C. *Chem. Mater.* **2009**, *21*, 2226

4) Katritzky, A. R.; Yousaf, T. I. *Can. J. Chem.* **1986**, *64*, 2087.

5) Farina, F.; Martinez-Utrilla, R.; Paredas, M. C.; Stefani, V. *Synthesis* **1985**, 781.

6) Bloom, S. M.; Dudek, G. O. *Tetrahedron* **1970**, *26*, 1267.

7) Stefanska, B.; Dzieduszycka, M.; Martelli, S.; Tarasiuk, J.; Bontemps-Gracz, M.; Borowski, E. *J. Med. Chem.* **1993**, *36*, 38.

8) Chi, X.; Itkis, M. E.; Kirschbaum, K.; Pinkerton, A. A.; Oakley, R. T.; Cordes, A. W.; Haddon, R. C. *J. Am. Chem. Soc.* **2001**, *123*, 4041.

Chapter 6: Neutral Radicals as Novel Transmissive to Black Electrochromic Materials in the Visible and SWIR Range

6.1: Introduction

In Chapter 2 we discussed the electrochromic properties of carbon nanotubes and possible applications which required fast response times. Other applications of electrochromic materials have different requirements. One of the most commonly proposed uses of electrochromic materials is use in smart windows. Smart windows are able to switch from transmissive to opaque states thus modulating the amount of light and energy passing through it. With an estimated over 50% of total energy use in a building being attributed to cooling, heating, and lighting, a significant energy savings can be achieved through incorporation of electrochromic materials into smart windows.[1-4]

An ideal smart window would go from a transmissive to black state, thus absorbing all visible light. The most common approach to this has been a combination of polymers which display different colors but mixed together display black and transmissive states.[5-8] There are some single component materials which show good transmissive to black electrochromic properties in the visible range.[9] However, even modulating the entire spectrum of visible light would not be enough as approximately half of the energy emitted by the sun that reaches the earth is from infrared range from 700 to 2500 nm (~short-wave infrared (SWIR)).[1] Thus, for truly energy saving smart windows, a materials must be able to display transmissive and opaque states in both the visible and SWIR range.

6.2: Overview of Electrochromic Properties of Phenalenyl Based Neutral Radical Conductors

As discussed in Chapters 3 and 4, phenalenyl based neutral radical conductors are grown as shiny black crystals and the precursors are red-orange compounds. As could also have been seen in the cyclic voltammograms, this process is reversible.[10] This is summarized in Figure 6.1, where $[Bu]_2B$ can be in its red-orange cationic state and its black neutral radical state. As can be seen, this occurs in both the solid and solution phase. This unique optical transformation brings about questions about its potential use in electrochromic cells.

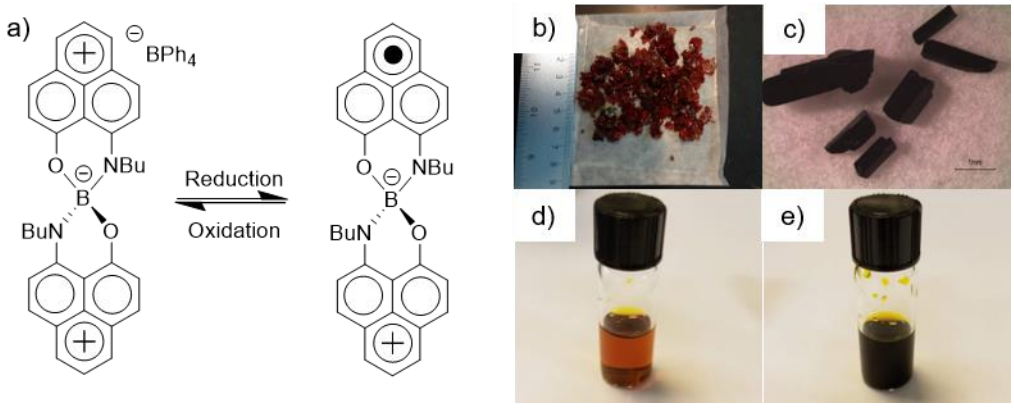

Figure 6.1: (a) Cationic and neutral radical structure of $[Bu]_2B$. Change of color between cationic and neutral radical states of $[Bu]_2B$ in (b,c) solid state and (d,e) in solution pictures.

6.3: Modulation of Visible Light in Electrochromic Cells Containing $[Bu]_2B$

While the electrochromic cells in Chapter 2 had an electrochromic component that was a thin film of SWNTs, here the electrochromic component would be a small molecule. While very similar to the cells in Chapter 2,

electrochromic cells containing electrochromic redox active materials still work in slightly different ways.

Figure 6.2 shows the proposed concept of the electrochemical mechanism of such cell operations. Here the electrochromic material would be dissolved into a solvent and combined with another material that undergoes the opposite redox process. In our case, the electrochromic material will be reduced from a cation to a neutral radical ($[Bu]_2B$), thus the other material should be able to be oxidized. Here hydroquinone will be selected due to its previously shown uses in the electrochromic field.[11] When a potential is applied (2V), the cation $[Bu]_2B^+$ is expected to be reduced to the radical $[Bu]_2B$, and thus the cell would experience a change in color. On the opposite electrode, hydroquinone needs to be oxidized to 1,4-benzoquinone. Then, when the device is turned off by decreasing the potential to 0 V, the molecules would diffuse and interact with one another recovering their original state with the cation $[Bu]_2B^+$ being reformed, and thus the cell is expected to return to its original color. This type of cell operation has been explored with viologens as the electrochromic small molecules changing from clear to single colored states, [12,13] but never with neutral radical molecules.

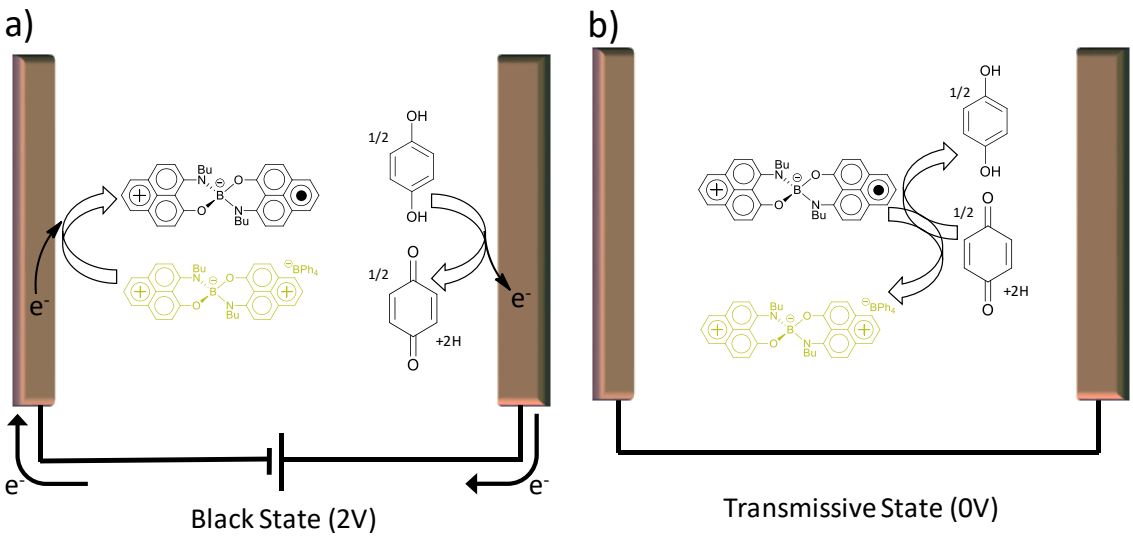

Figure 6.2: Electrochemistry of electrochromic device operations. (left) At an applied potential, $[PLY(O,NBu)]_2B^+$ is reduced to the neutral radical $[PLY(O,NBu)]_2B$ (1 electron reduction) while hydroquinone is oxidized to 1,4-benzoquinone (2 electron oxidation) resulting in a black state. (Right) When no potential is applied (0V) $[PLY(O,NBu)]_2B$ and 1,4-benzoquinone diffuse and $[PLY(O,NBu)]_2B$ is oxidized to $[PLY(O,NBu)]_2B^+$ while 1,4-benzoquinone is reduced to hydroquinone (transmissive state).

To test the proposed concept experimentally with a case of phenalenyl based molecules, a solution of $[Bu]_2B^+$ $^-BPh_4$ (tetraphenylborate) and hydroquinone in propylene carbonate is placed between two indium tin oxide (ITO) covered glass substrates to form an electrochromic cell. Upon application of a potential between opposing ITO electrodes, cationic $[PLY(O,NBu)]_2B^+$ is reduced to its neutral radical form and hydroquinone is oxidized to 1,4-benzoquinone (Figure 6.2). The reduction of $[PLY(O,NBu)]_2B^+$ to the neutral radical $[PLY(O,NBu)]_2B$ is visually observed through a change of the cell from a yellow transmissive to a black state (Figure 6.3a). Figure 6.3b shows the visible and partial near-IR range transmittance spectra of the device in its bleached and

colored state. The bleached state shows relatively high transparency of ~ 65% at wavelengths above 500 nm switching to transmittance of 10-30% in the black state.

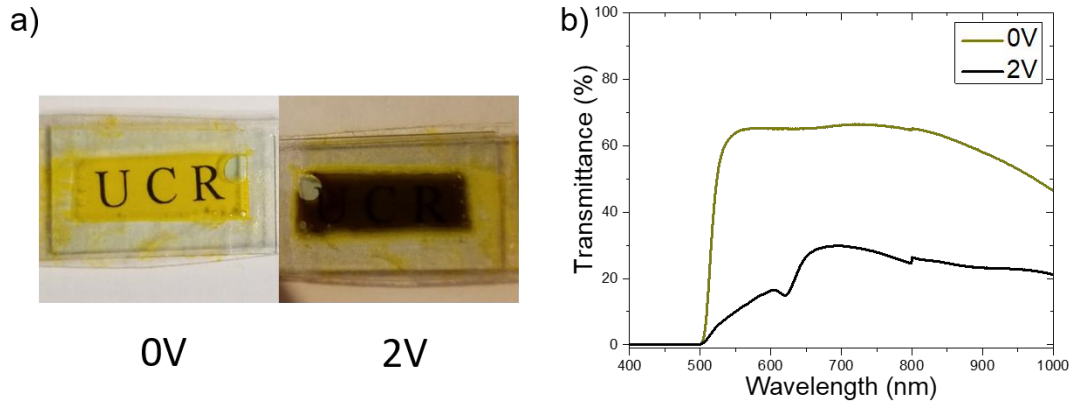

Figure 6.3: Electrochromic properties of $[NBu]_2B$ in an ITO-glass sandwich structure. (a) Pictures of the devices in clear and black state. (b) Accompanying transmittance spectra.

The cycling stability of the electrochromic cell was tested at 575 nm by switching applied potentials between +2.0 V (60 seconds) and 0 V (60 seconds). After several activation cycles at 575 nm the full amplitude of transmission (T) modulation between the transmissive state ($T \approx 65\%$) and black state ($T \approx 18\%$) has been achieved with the amplitude of modulation ($\Delta T \approx 47\%$) maintained at least for 6000 s (50 cycles) (Figure 6.4a). The response time (τ), defined as the time it takes for the device to reach 90% of its saturation signal, was evaluated at the level of 20-30 seconds as shown in Figure 6.4b at 575 nm. The response dynamics are controlled by the time required for the reduction of $[NBu]_2B$ (for darkening) and the time required for the reduced $[NBu]_2B$ and oxidized

hydroquinone (benzoquinone) to diffuse and meet each other in order to exchange charge (for bleaching) (Figure 6.2). The response time at the level of 20-30 s is acceptable for smart window applications and could possibly be improved through device optimization.[14]

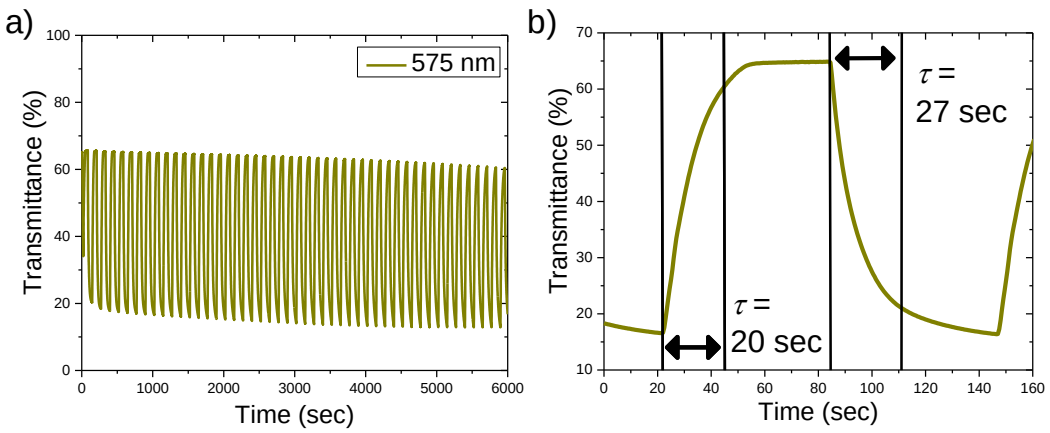

Figure 6.4: (a) Cycling response at 575 nm and (b) the expanded pulse shape showing corresponding response times.

Some loss of transmittance in the bleached state is partially due to the contribution of two ITO covered glass substrates (Figure 6.5a) and can be reduced by further device optimization. While modulating visible light is important, for energy saving smart windows infrared light from 700-2500 nm (~ SWIR) must also be considered as it is responsible for approximately half of the energy output from the sun that reaches the earth.[1] Thus, an ideal smart window would modulate both visible and short wave infrared (SWIR) light. Testing SWIR light modulation using the above device is prevented by the strong absorption of conducting ITO above wavelength of 1200 nm (Figure 6.5b).

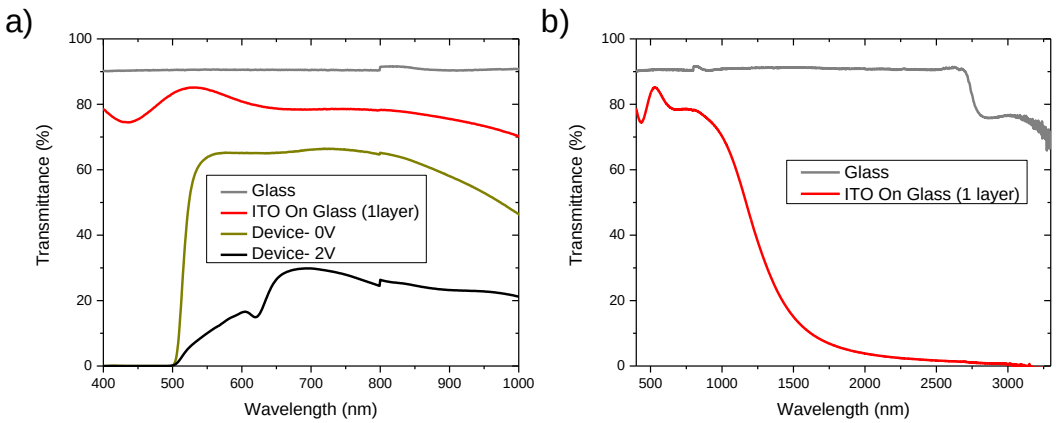

Figure 6.5: Transmittance spectra of device, ITO on glass in the range of interest (400-1000 nm). (b) Transmittance spectra of glass and ITO on glass showing high absorption of ITO above 1200 nm.

6.4: Modulation of Short-Wave Infrared Light in Electrochromic Cells Containing $[Bu]_2B$

In order to expand the spectral range of electrochromic devices to the SWIR range ITO must be replaced. Thus, in a new set of devices the ITO conducting layers on both opposing electrodes were substituted with films of metallic single-walled carbon nanotubes (MT-SWNTs).[15,16] The metallic type of SWNTs was selected because it has less interfering spectral features and lower absorption in the SWIR spectral ranges than semiconducting SWNTs, and MT-SWNT thin films provide very efficient transparent conductive layers at very low thicknesses as shown in Figure 6.6. As can be seen this is a significant improvement over ITO.

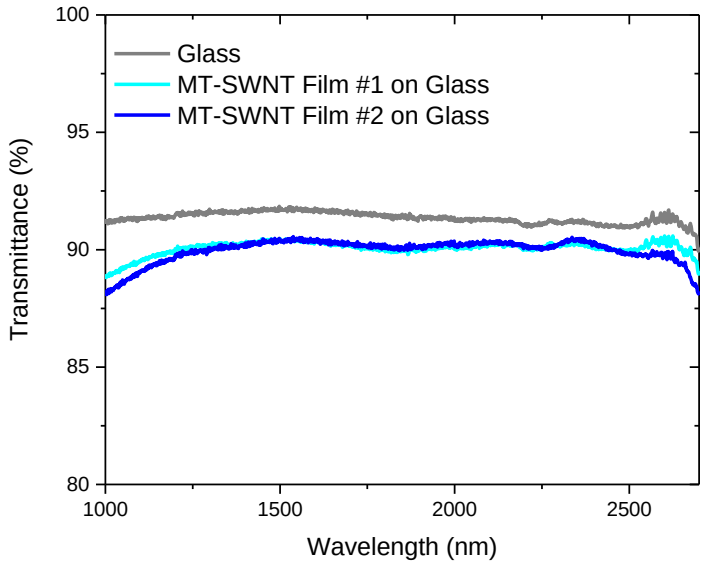

Figure 6.6: Transmittance spectra of MT-SWNT films on glass.

Figure 6.7a shows a picture of the device in its transmissive (0V) and colored (2V) state and Figure 6.7b shows the corresponding transmittance spectra. In the IR area of interest, 1000-2500 nm, the average transmittance in the bleached and colored state is 64.9% and 24.0 %, respectively, demonstrating a high degree of modulation ($\Delta T \approx 41\%$).

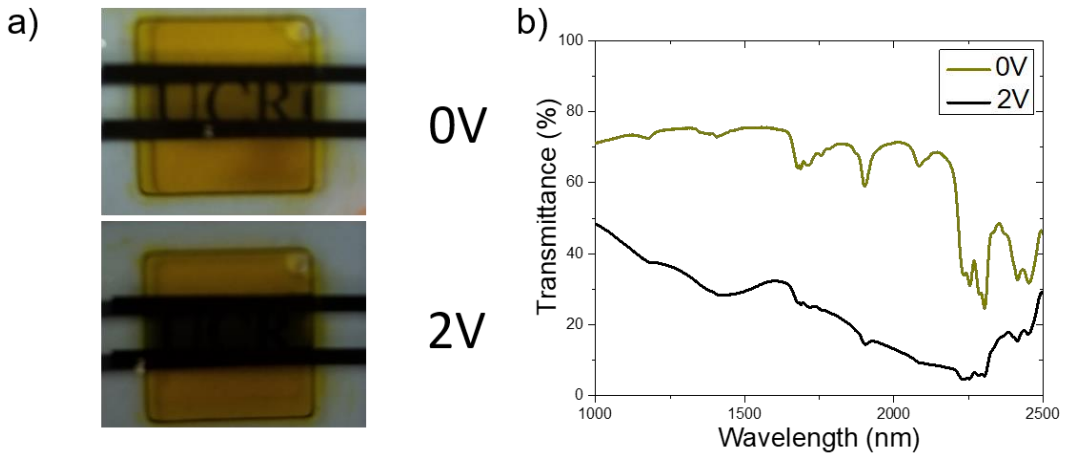

Figure 6.7: (a) Pictures of the $[Bu]_2B$ device utilizing MT-SWNT thin film electrodes and (b) the corresponding transmittance spectra in the transparent and opaque state.

A significant amount of absorption in both the bleached and colored states in the range from 1000-2500 nm is due to propylene carbonate, the solvent used in the cell (Figure 6.8a). Figure 6.8b presents the transmittance spectra of the device with the propylene carbonate subtracted out. It shows a significant increase of the transparency of the bleached state if the losses due to solvent are reduced along with an increased amplitude of the transmittance modulation (ΔT) up to 70% at 2200 nm. Thus, using thinner cells with less solvent in the optical path can improve the performance of the electrochromic cell as previously shown

in Chapter 2 with the LWIR devices. Even further improvement could be achieved through the elimination of solvent through the design of a solid-state device.

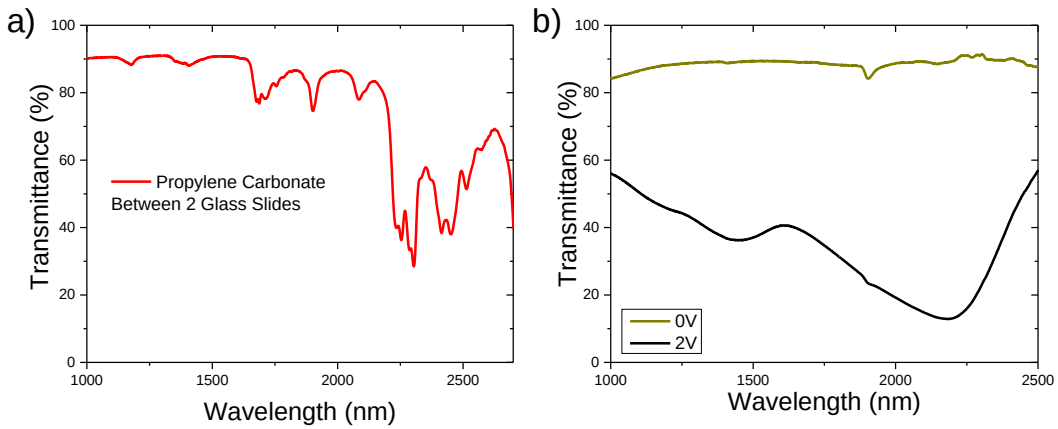

Figure 6.8: (a) Transmittance spectra of propylene carbonate between 2 glass slides and (b) the spectra of devices in Figure 6.6 with the contribution of propylene carbonate subtracted out.

Figure 6.9 shows the cycling of the device over 6000 seconds (60 seconds at 2V, 60 seconds at 0V) and not much degradation is observed showing that the electrochromic properties are reversible. The response time is on the order of 10 seconds (Figure 6.9b), which is shorter than in case of the ITO electrodes in agreement with our recent work on SWNT electrochromic cells.[14]

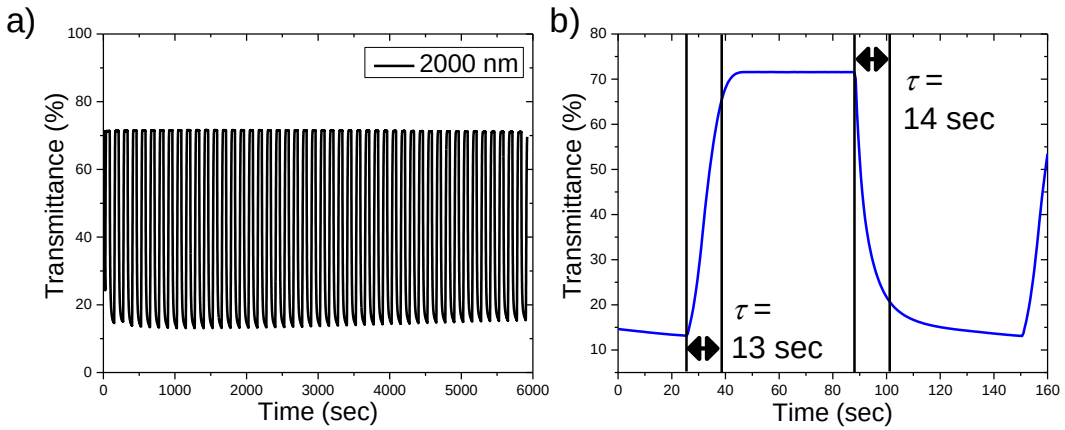

Figure 6.9: (a) Cycling response of device at 2000 nm and (b) corresponding response time.

6.5: Conclusion

We demonstrated that neutral radical small molecules, in particular $[Bu]_2B$, can be utilized as an electrochromic medium which can modulate both visible and SWIR light. This unique property could allow the material to serve as part of a smart window for energy conservation. While the devices showed good modulation, they could be further improved through the design optimization including the possibility of incorporation into a solid state device.

6.6: Experimental

Materials: Propylene Carbonate and hydroquinone were used as received (Sigma Aldrich).

Synthesis of [PLY(O,NBu)]$_2$B: [PLY(O,NBu)]$_2$B was synthesized as the cationic salt ([PLY(O,NBu)]$_2$B$^+$ $^-$BPh$_4$) according to the literature.

Preparation of Electrochromic solution: 8 mg of [PLY(O,NBu)]$_2$B$^+$ $^-$BPh$_4$ (9.0 x 10^{-6} mol) along with 2 mg hydroquinone (1.8 x 10^{-5} mol) was dissolved in 1 mL of propylene carbonate.

ITO Sandwich Device preparation: The electrochromic solution is sandwiched between two ITO coated glass slides (20 Ohm/sq, Thin Film Devices, Inc, Anaheim, CA) and sealed utilizing double sided tape with 3.5 mm x 13 mm rectangle cut aperture.

MT-SWNT Sandwich Device preparation: Similar to our previous report, the thin MT-SWNT films (30 nm thick) were made utilizing vacuum filtration of the dispersion of large diameter (1.2-1.7 nm) 99% separated (IsoNantube-M) metallic SWNTs purchased from Nanointegris Inc. The films were transferred onto glass substrates bridging a 2 mm gap between predeposited Ti(15nm/Pt(150 nm) electrodes. On one substrate, an adhesive seal frame (0.25 mm thick) (Frame-SealTM, Bio-Rad Laboratories) is placed. The cell is filled with electrochromic solution and another matching MT-SWNT on glass substrate is placed overtop.

Spectroscopy/Electrochromic Measurements: Transmittance spectra were recorded on a Cary 5000 UV-Vis Spectrophotometer (Agilent Technology). The

potential was applied using a model DS345 synthesized function generator (Stanford Research Systems).

6.7: References

1) Khandelwal, H.; Schenning, A. P. H. J.; Debije, M. G. *Adv. Energy Mater.* **2017**, *7*.

2) Hsu, C. Y.; Zhang, J.; Sato, T.; Moriyama, S.; Higuchi, M. *ACS App. Mater. Interfaces* **2015**, *7*, 18266.

3) Granqvist, C. G. *Thin Solid Films* **2014**, *564*, 1.

4) Baetens, R.; Jelle, B. P.; Gustavsen, A. *Sol. Energy Mater Sol. Cells* **2010**, *94*, 87.

5) Shin, H.; Kim, Y.; Bhuvana, T.; Lee, J.; Yang, X.; Park, C.; Kim, E. *ACS App. Mater. Interfaces* **2012**, *4*, 185.

6) Zhang, Q.; Tsai, C. Y.; Abidin, T.; Jiang, J. C.; Shie, W. R.; Li, L. J.; Liaw, D. J. *Polym. Chem.* **2018**, *9*, 619.

7) Liu, H. S.; Pan, B. C.; Huang, D. C.; Kung, Y. R.; Leu, C. M.; Liou, G. S. *NPG Asia Mater.* **2017**, *9*.

8) Beaujuge, P. M.; Ellinger, S.; Reynolds, J. R. *Nat. Mater.* **2008**, *7*, 795.

9) Abraham, S.; Mangalath, S.; Sasikumar, D.; Joseph, J. *Chem. Mater.* **2017**, *29*, 9877.

10) Bag, P.; Itkis, M. E.; Stekovic, D.; Pal, S. K.; Tham, F. S.; Haddon, R. C. *J. Am. Chem. Soc.* **2015**, *137*, 10000

11) Palenzuela, J.; Vinuales, A.; Odriozola, I.; Cabanero, G.; Grande, H. J.; Ruiz, V. *ACS App. Mater. Interfaces* **2014**, *6*, 14562.

12) Moon, H. C.; Kim, C. H.; Lodge, T. P.; Frisbie, C. D. *ACS App. Mater. Interfaces* **2016**, *8*, 6252.

13) Alesanco, Y.; Vinuales, A.; Cabanero, G.; Rodriguez, J.; Tena-Zaera, R. *ACS App. Mater. Interfaces* **2016**, *8*, 29619.

14) Stekovic, D.; Arkook, B.; Li, G.; Li, W.; Bekyarova, E.; Itkis, M. E. *Adv. Mater. Interfaces* **2018**, 1800861.

15) Wan, J. Y.; Xu, Y.; Ozdernir, B.; Xu, L.; Sushkov, A. B.; Yang, Z.; Yang, B.; Drew, D.; Barone, V.; Hu, L. B. *ACS Nano* **2017**, *11*, 788.

16) Vasilyeva, S. V.; Unur, E.; Walczak, R. M.; Donoghue, E. P.; Rinzler, A. G.; Reynolds, J. R. *ACS App. Mater. Interfaces* **2009**, *1*, 2288.